Politecnico di Torino

Politecnico di Torino

Master of science program in
Environmental and Land Engineering

Master Degree Thesis

Passive seismic and electrical resistivity tomography monitoring of high-altitude rock masses under climate change: the Sas da Lech case study (Dolomites, BZ)

Supervisor:
Prof.ssa Chiara Colombero

Co-supervisor:
Lorena Di Toro

Candidate:
Margherita Tamietto s332774

Academic Year 2024 – 2025

Abstract

Long-term continuous ambient seismic monitoring and electrical resistivity tomography (ERT) surveys can be valuable geophysical techniques for understanding the response of unstable rock volumes to external meteorological variations. Their increasing application in glacial and periglacial mountain areas is mainly aimed at monitoring of rock glaciers and permafrost, being among the most reliable indicators of climate change due to their sensitivity to temperature variations. Mountain regions such as the Alps are expected to be particularly affected by 21st-century global warming, and the related permafrost thawing has potential impacts on slope stability, potentially increasing the likelihood of related hazards. Therefore, the importance of monitoring the Sas da Lech rock columns, in the Dolomites (Italy, BZ). In the site, after the occurrence of several landslide events, extensometers, multiparametric columns, and geophones were installed between 2023 and 2024. In addition, two ERT surveys were performed to have a more complete understanding of the geological and geomorphological conditions.

In this thesis work are reported the analyses of the five months of data collected at the monitoring site, including a comparison with the nearest meteorological meteo station data. The latter was performed to identify the most controlling parameters on the thermo-mechanical behaviour of two rock columns resting on the Raibl Formation.

Daily and seasonal scale reversible fluctuations were observed on seismic parameters mainly controlled by external air temperature, while rock temperature strongly influences the microseismic events occurrence.

Given the observed sensitivity to temperature of the rock columns, a long-term temperature analysis was performed. It turned out that in the past thirty-four years the area experienced significant warming of 0.045 °C/year. Future projections, within RCP4.5 scenario, suggests a slightly decreasing temperature trend (2031-2100). While RCP2.6 shows a stable mean temperature with no significant increase, RCP8.5 exhibits an even steeper warming trend, reaching +0.062 °C/year.

Overall, the integrated analysis of the available data suggests a strong thermal control on the seismic response of the unstable rock columns. Indeed, temperature plays a key role in controlling both microseismicity and resonance-frequency variations. Given this observed thermal influence, and considering that the monitored columns rest on a lithology particularly sensitive to thawing and freezing cycles, their behaviour under external thermal forcing can be consistently explained through the geological characteristics of the site.

Contents

1 Introduction **1**

2 Applied geophysics theory **2**
2.1 Passive seismics . . . 2
2.1.1 H/V . . . 3
2.1.2 Microseismicity . . . 5
2.2 Electrical methods . . . 5
2.2.1 ERT . . . 5

3 Case study: Sas da Lech **8**
3.1 Geographical setting . . . 9
3.2 Geological setting . . . 11
3.3 Instrumentation setup . . . 13
3.4 Meteo stations . . . 17
3.5 Data analysis . . . 18
3.5.1 Temperature analysis . . . 18
3.5.2 Main fracture deformation . . . 21
3.5.3 Azimuth and frequency . . . 23
3.5.4 PSD and H/V . . . 27
3.5.5 Microseismicity . . . 38
3.5.6 ERT . . . 55

4 Climate change and future projections **60**
4.1 Permafrost . . . 60
4.2 Temperature Variability: Historical Data and Future Projections . . . 63
4.2.1 Climate Change in the Alps: Review of the Literature . . . 63
4.2.2 Historical Temperature Observations . . . 65
4.2.3 Projected Future Temperatures . . . 72

5 Method assessment and future work **76**
5.1 Advantages and limitations . . . 76
5.2 Future work . . . 78

6 Conclusions **79**

List of Figures

2.1 Schematic representation of the spectral analysis of ambient seismic noise recorded at an unstable site (A: stable reference station, B: station on unstable column). Station A does not show spectral amplifications. The resonance frequency (f_1) of the unstable compartment is extracted from the power spectral density (PSD) of the noise recorded at station B. Geometric and mechanical parameters are defined in the text. Modified from Colombero et al. (2021). 4

2.2 Possible ERT array configurations. A and B are current electrodes, while M and N are potential electrodes. 6

3.1 NNW face of the Sas da Lech, before (left) and after (right) the landslides occurring in 2018. (*Google, 2025*). 8

3.2 Overview of the monitoring site, with Piz Pisciadù on the left and the Sas da Lech in the center and Sass dai Ciamorces behind it. 10

3.3 Spatial allocation of the region of interest. The study site is shown as an orange marker, while the available meteo stations are displayed in blue (*QGIS Development Team, 2023*). 10

3.4 Geological profile across the summit of the Sas da Lech (*Mussner, 2009*). . 11

3.5 Faults and rock glaciers map of the Sella N-side. Most of the faults are small-offset strike-slip faults formed during the Neoalpine phase (*Mussner, 2009*, modified). Faults: General fault (solid red line) and Suspected fault (dashed red line). Reverse/thrust fault (red triangles). Is here highlighted also the Paleo-faults of Carnian age Normal fault (solid black line) and Presumed normal fault (dashed black line) crossing the Sas da Lech. 12

3.6 The normal fault in the Cassian Dolomite on the East face of the Sas da Lech (shown in red). 13

3.7 Schematic representation of the locations of the instruments within the monitoring site: geophones (GEA06, GEA07, GEA11, GEA12), extensometer (E21), multiparametric columns (DMS1, DMS2) and electrodes (e1-e48). 14

3.8 Schematic top view of the monitoring site. Geophones are shown in red, while extensometer 21 is shown in green (monitoring what is hereafter referred to as the main fracture, between blocks 3 and 4). Rock block 1 is stable, block 2 collapsed in 2018, block 3 is monitored by GEA06 (hereafter referred to as the northern rock column), and block 4 is monitored by GEA07 (hereafter referred to as the eastern rock column). 14

3.9 Location of the geophones at the monitoring site. Panels (a)–(c) show photographs from the photogrammetric survey, arranged from the easternmost to the northernmost viewpoints. The precise locations of the geophones are highlighted with red rectangles. (a) GEA12, installed on the Raibl Formation within the stable compartment, with a close-up view in (d). (b) GEA11, positioned on the Raibl Formation. (c) GEA07 and GEA06, both installed on the Dolomia Principale but located on two distinct rock columns. (e) Close-up view of GEA07. 15
3.10 Air temperature time series from extensometer 21 and the "Badia Cima Pisciadù" meteorological station, shown at 30-minute resolution. 18
3.11 Rock temperature time series at the two multiparametric columns (DMS1 and DMS2) compared to air temperature from extensometer 21, shown at 30-minute resolution. 20
3.12 Rock temperature time series at the multiparametric column DMS1 at different depths compared to air temperature from extensometer 21, shown at 30-minute resolution. Module 19 is the most superficial one, from the rock surface to 1 m depth; module 15 is the deepest one, going from 4 m depth to 5 m depth. The other 14 modules are not represented here to allow for a clearer visualization of the most superficial modules; however, they showed almost constant temperature throughout the year. 20
3.13 Air temperature and deformation time series from extensometer 21 at 30-minute resolution. A dashed horizontal line marks 0 °C. Deformation could be corrected only over a limited interval where rotation parameters were within the valid 0–360° range. 21
3.14 Daily-scale analysis of air temperature and deformation at extensometer 21: (a) residual temperature and deformation, (b) daily Pearson correlation coefficient, and (c) lag in hours from the cross-correlation. 22
3.15 Seasonal-scale analysis of air temperature and deformation at extensometer 21: (a) 30-day moving mean of temperature and deformation, and (b) 60-day moving correlation coefficient. 23
3.16 Frequency and azimuth analysis for geophone GEA06. Top panel: time series of the frequency associated to the maximum amplitude of the horizontal components. Bottom panel: corresponding azimuth of the extracted frequency. Blue indicates period 1 and orange indicates period 2. White regions represent data gaps whereas vertical black lines represents data gap within both monitoring periods. 24
3.17 Frequency and azimuth analysis for geophone GEA07. Top panel: time series of the frequency associated to the maximum amplitude of the horizontal components. Bottom panel: corresponding azimuth of the extracted frequency. Blue indicates period 1 and orange indicates period 2. White regions represent data gaps whereas vertical black lines represents data gap within both monitoring periods. 24

3.18 Frequency and azimuth analysis for geophone GEA11. Top panel: time series of the frequency associated to the maximum amplitude of the horizontal components. Bottom panel: corresponding azimuth of the extracted frequency. Blue indicates period 1 and orange indicates period 2. White regions represent data gaps whereas vertical black lines represents data gap within both monitoring periods. 25
3.19 Frequency and azimuth analysis for geophone GEA12. Top panel: time series of the frequency associated to the maximum amplitude of the horizontal components. Bottom panel: corresponding azimuth of the extracted frequency. Blue indicates period 1 and orange indicates period 2. White regions represent data gaps whereas vertical black lines represents data gap within both monitoring periods. 25
3.20 Spectral analysis of ambient seismic noise recorded at GEA06 (base of the northern rock column). (a)-(c) Probability density function of the hourly averaged power spectral density, with average (blue line) and 10th–90th percentiles (red dashed lines) of the data set: (a) east, (b) north and (c) vertical components. Black dashed lines: boundaries of the NHNM and NLNM of Peterson (*Peterson, 1993*). (d)–(f) Hourly averaged power spectral densities over the whole monitored period: (d) east, (e) north and (f) vertical components. 29
3.21 Spectral analysis of ambient seismic noise recorded at GEA07 (base of the eastern rock column). (a)-(c) Probability density function of the hourly averaged power spectral density, with average (blue line) and 10th–90th percentiles (red dashed lines) of the data set: (a) east, (b) north and (c) vertical components. Black dashed lines: boundaries of the NHNM and NLNM of Peterson (*Peterson, 1993*). (d)–(f) Hourly averaged power spectral densities over the whole monitored period: (d) east, (e) north and (f) vertical components. 29
3.22 Spectral analysis of ambient seismic noise recorded at GEA11 (over the Raibl Formation). (a)-(c) Probability density function of the hourly averaged power spectral density, with average (blue line) and 10th–90th percentiles (red dashed lines) of the data set: (a) east, (b) north and (c) vertical components. Black dashed lines: boundaries of the NHNM and NLNM of Peterson (*Peterson, 1993*). (d)–(f) Hourly averaged power spectral densities over the whole monitored period: (d) east, (e) north and (f) vertical components. 30
3.23 Spectral analysis of ambient seismic noise recorded at GEA12 (reference station, over the stable compartment). (a)-(c) Probability density function of the hourly averaged power spectral density, with average (blue line) and 10th–90th percentiles (red dashed lines) of the data set: (a) east, (b) north and (c) vertical components. Black dashed lines: boundaries of the NHNM and NLNM of Peterson (*Peterson, 1993*). (d)–(f) Hourly averaged power spectral densities over the whole monitored period: (d) east, (e) north and (f) vertical components. 30

3.24 Ambient seismic noise single station spectral ratios. (a)–(d) Probability density functions of the hourly averaged spectral ratios, with average (blue line) and 10th–90th percentiles (red dashed lines) of the data set. (e)–(h) Hourly averaged spectral ratios over the whole monitored period. Panels (a) and (e): H/V of GEA06; (b) and (f): H/V of GEA07; (c) and (g): H/V of GEA11; (d) and (h): H/V of GEA12. 32
3.25 Hourly-averaged spectral ratios of GEA07 over the entire monitored period. The temporal gap between the two monitoring periods has been intentionally reduced in the figure to improve the visibility of the data within each period. 33
3.26 GEA06 hourly averaged ambient seismic noise single-station spectral ratios compared with meteorological variables for period 1. (a) Temporal evolution of the spectral ratios; white bands across all frequencies indicate data gaps. (b) Wind speed and wind gust time series from the "Badia Cima Pisciadù" meteorological station. (c) Air temperature from the "Badia Cima Pisciadù" meteorological station and from extensometer 21 at the monitoring site. 34
3.27 GEA07 hourly averaged ambient seismic noise single-station spectral ratios compared with meteorological variables for period 1. (a) Temporal evolution of the spectral ratios; white bands across all frequencies indicate data gaps. (b) Wind speed and wind gust time series from the "Badia Cima Pisciadù" meteorological station. (c) Air temperature from the "Badia Cima Pisciadù" meteorological station and from extensometer 21 at the monitoring site. 35
3.28 GEA07 hourly averaged ambient seismic noise single-station spectral ratios compared with meteorological variables for period 2. (a) Temporal evolution of the spectral ratios; white bands across all frequencies indicate data gaps. (b) Wind speed and wind gust time series from the "Badia Cima Pisciadù" meteorological station. (c) Air temperature from the "Badia Cima Pisciadù" meteorological station and from extensometer 21 at the monitoring site. 35
3.29 Horizontal GEA07 PSDs comparison with wind speed measured at the meteorological station "Badia Cima Pisciadù" within period 1. Data shown are the hours in which the wind speed exceeds the threshold of 3.99 m/s, corresponding to the mean value over period 1. (a) East component PSD. (b) North component PSD. (c) Wind speed. 36
3.30 Horizontal GEA07 PSDs comparison with wind speed measured at the meteorological station "Badia Cima Pisciadù" within period 2. Data shown are the hours in which the wind speed exceeds the threshold of 2.96 m/s, corresponding to the mean value over period 2. (a) East component PSD. (b) North component PSD. (c) Wind speed. 37
3.31 Comparison of GEA07 PSDs with air temperature measured at Extensometer 21 during period 2, focusing on daytime hours. (a)-(c) East, North, and Vertical component PSDs shown only for daytime hours (07:00–19:00). (d) Air temperature at Extensometer 21. Daytime periods are highlighted with vertical shaded bands (07:00–19:00). 38

3.32 Comparison of GEA07 PSDs with air temperature measured at Extensometer 21 during period 2, focusing on nighttime hours. (a)-(c) East, North, and Vertical component PSDs shown only for nighttime hours (20:00–06:00). (d) Air temperature at Extensometer 21. Nighttime periods are highlighted with vertical shaded bands (20:00–06:00). 38
3.33 Illustration of the STA/LTA algorithm (*Ltd., 2019*). 39
3.34 Cumulative GEA06 events during period 1. Blue vertical bars highlight the main steep steps in the curve. 42
3.35 Distribution of microseismic events extracted from GEA06 ambient seismic noise using STA/LTA across different hours of the day. 42
3.36 Examples of microseismic events recorded at GEA07. In each plot, from the top to the bottom: seismogram, related Fourier spectrum and spectrogram. Events like these are likely micro-fracturing events. 43
3.37 Examples of the same microseismic event extracted at GEA06 (left) and at GEA07 (right). In each plot, from the top to the bottom: seismogram, related Fourier spectrum and spectrogram. Events like these are likely related to helicopter flights nearby the rock columns. 44
3.38 Examples of microseismic events extracted at GEA06 (a-c-e) and at GEA07 (b-d-f). In each plot, from the top to the bottom: seismogram, related Fourier spectrum and spectrogram. Events like these are likely related to local and regional earthquakes. (a-b) Same earthquake extracted by both station on 23/09/2024 12:53:33, registered in catalogue with code EqId:1710484. (c-d) earthquake event extracted just by GEA07. (e-f) Local earthquake not registered in catalogues but recorded and extracted by geophones on the site. 45
3.39 Examples of microseismic events extracted at GEA07 within period 2 that were not easy to be related to some ongoing process. 46
3.40 Peak frequencies of microseismic events extracted from GEA06 and GEA07. Blue markers correspond to events from period 1 (16/09/2024–18/12/2024), while orange markers correspond to events from period 2 (26/06/2025–04/09/2025). 47
3.41 Example of electromagnetic interference recorded in the ambient seismic noise of geophones, with frequency peaks observed at 50 and 100 Hz. (a) Seismogram recorded on channel N. (b) Corresponding Fourier spectrum. (c) Corresponding spectrogram. 47
3.42 Peak frequencies of extracted and filtered GEA07 microseismic events. Filtering removed events occurring during human presence on the site, events with kurtosis > 500, total duration < 13 s, maximum amplitude > 0.02 m/s, and events with peak frequencies outside the ranges 2-11 Hz and 65-85 Hz. Blue markers correspond to events from period 1, while orange markers correspond to events from period 2. 48
3.43 Comparison between peak frequency and maximum energy band of GEA07 in periods 1 and 2. (a) Histogram of peak frequencies of the extracted and filtered events, using 5 Hz bins. (b) 5 Hz bins associated with the maximum energy, computed as the frequency interval with the largest area under the amplitude spectrum. 49

3.44 Cumulative GEA07 events during period 1. Blue vertical bars highlight the main steep steps in the curve. 49
3.45 Cumulative GEA07 events during period 2. Blue vertical bars highlight the main steep steps in the curve. 50
3.46 Microseismic events at GEA07 during period 1 compared with meteorological parameters. Grey vertical bars indicate the main steep increases in the event rate. (a) Event rate at GEA07, expressed as the number of microseismic events per hour. (b) Air temperature measured at extensometer 21 and rock temperature at module 19 of DMS1 and DMS2. (c) Wind speed and wind gust speed recorded at the meteorological station "Badia Cima Pisciadù". (d) Precipitation, reported as the mean value measured at the two valley stations "Corvara" and "Selva di Val Gardena" on hours when rainfall was recorded at both stations. 52
3.47 Microseismic events at GEA07 during period 2 compared with meteorological parameters. Grey vertical bars indicate the main steep increases in the event rate. (a) Event rate at GEA07, expressed as the number of microseismic events per hour. (b) Air temperature measured at extensometer 21 and rock temperature at module 19 of DMS1 and DMS2. (c) Wind speed and wind gust speed recorded at the meteorological station "Badia Cima Pisciadù". (d) Precipitation, reported as the mean value measured at the two valley stations "Corvara" and "Selva di Val Gardena" on hours when rainfall was recorded at both stations. 52
3.48 Rock temperature influence on microseismic event occurrence. For each 1 °C temperature bin, the mean number of events per hour occurring within that bin is reported, along with the total number of recorded hours falling in the same temperature range. Data from period 1 and period 2 were combined for this analysis. 53
3.49 Wind speed influence on microseismic event occurrence. For each 1 m/s wind speed bin, the mean number of events per hour occurring within that bin is reported, along with the total number of recorded hours falling in the same wind speed range. Data from period 1 and period 2 were combined for this analysis. 54
3.50 Distribution of microseismic events, extracted from GEA07 ambient seismic noise and filtered, across different hours of the day. Data from period 1 and period 2 were combined for this analysis. 55
3.51 Distribution of microseismic events, extracted from GEA07 ambient seismic noise and filtered, across different hours of the day in different time periods. (a) First part of period 1, up to the 9th November 2024. (b) Second part of period 1. (c) Period 2. 55
3.52 Electrode settings at the site. 56
3.53 Resistivity model obtained from the inversion of the ERT performed on 26th June 2025. Both Dipole–Dipole and Wenner–Schlumberger data were used for the inversion. Dots along the surface indicate the electrode positions, from electrode 1 (E1) to electrode 48 (E48). The lines with dots represent the multiparametric columns, showing rock temperature in °C at each module depth (every 1 m). 58

3.54 Resistivity model obtained from the inversion of the ERT performed on 4th September 2025. Both Dipole–Dipole and Wenner–Schlumberger data were used for the inversion. Dots along the surface indicate the electrode positions, from electrode 1 (E1) to electrode 48 (E48). The lines with dots represent the multiparametric columns, showing rock temperature in °C at each module depth (every 1 m). 58
3.55 Rock temperature with depth at the multiparametric columns DMS1 and DMS2 measured during the ERT surveys. 59

4.1 Alpine Permafrost Index Map (APIM) shown for the European Alps (AT: Austria, CH: Switzerland, DE: Germany, FR: France, IT: Italy, SL: Slovenia). 61
4.2 Left map: surface type map zoomed over the study area. Right map: APIM zoomed over the study area. Realised using QGIS (*QGIS Development Team, 2023*). 62
4.3 Daily temperature time series from the Pian Fedaia meteorological station; vertical black bars indicate missing data. 66
4.4 Comparison between daily air temperatures measured Pian Fedaia meteorological station and at the monitoring site (Extensometer 21) 66
4.5 Difference in the daily mean temperature between extensometer21 and Pian Fedaia, with a 15-day moving average to better highlight the temporal trend throughout the all period (top plot). Difference in the daily thermal range between extensometer21 and Pian Fedaia, with 15-day moving average to visualize better the trend (bottom plot). 67
4.6 Pian Fedaia meteoreological station amplitude spectrum, with highlighted the main frequency corresponding to 1 years, 6 months and 4 months. . . . 68
4.7 Pian Fedaia periodic component (red line), daily average temperature (black line), and gap-filled complete-year dataset (blue dots). 69
4.8 Pian Fedaia trend evaluated from residuals obtained by removing the periodic component (top) and the daily average temperature (bottom). . . . 70
4.9 Monthly mean air temperature at Pian Fedaia meteorological station and of the historical scenario. 72
4.10 Comparison of monthly mean air temperature time series including raw Pian Fedaia data, historical data, RCP2.6 scenario data before and after bias correction. 73
4.11 Comparison of monthly mean air temperature time series including raw Pian Fedaia data, historical data, RCP4.5 scenario data before and after bias correction. 73
4.12 Comparison of monthly mean air temperature time series including raw Pian Fedaia data, historical data, RCP8.5 scenario data before and after bias correction. 74
4.13 Annual mean temperature time series for CORDEX RCP2.6, RCP4.5 and RCP8.5 scenarios. The curves are smoothed using a 5-year Gaussian filter to highlight long-term trends. Data shown are bias-corrected. 74

5.1 CORDEX grid over the study area. The study site is shown as an orange marker, while the available meteo stations are displayed in blue. Realised using QGIS (*QGIS Development Team, 2023*). 77

List of Tables

3.1 Seismic recording intervals within period 1 and period 2 of each geophone. 16
3.2 Data available at the monitoring site. 16
3.3 Details of the meteorological stations selected to download weather data. . 17
3.4 Filtering criteria used to remove events recorded while operators were on site, and corresponding number of events removed. 40
3.5 Number of ERT measurements after the filtering performed with the software Prosys-III (IrisInstruments) on Dipole-Dipole and Wenner-Schlumberger arrays. 56

4.1 Dataset Information. 71
4.2 Configuration of the CORDEX dataset downloaded from the Copernicus Climate Data Store for the climate analysis at Pian Fedaia meteorological station. 71

1. Introduction

The mountain regions are dynamic and complex environments, highly sensitive to climate variability. There, geomorphological processes are strongly influenced by climatic conditions. Indeed, mountain areas are particularly susceptible to changes in atmospheric temperature largely owing to the sensitivity of surface and sub-surface cryosphere components to melting conditions (*Bonometti, 2025*). In the Alps, ongoing temperature rise and the widespread degradation of permafrost are increasingly affecting the rock stability, contributing to a growing number of instability events observed over the last decades. Besides the rising of temperatures, the seasonal cycles of precipitation, global radiation, and relative humidity are also expected to change in the Alps, as well as temperature and precipitation extremes (*Gobiet et al., 2014*).

Understanding how high-altitude rock masses respond to thermal forcing and to other changing meteorological parameters is therefore of increasing interest, both for scientific investigation and for understanding the triggering mechanisms, as well as for the assessment of natural hazards (climate change adaptation perspective).

Geophysical methods have proven particularly valuable for studying these processes. Techniques such as ambient seismic noise monitoring and electrical resistivity tomography (ERT) allow for the indirect characterization of the internal structure, mechanical behaviour, and thermal state of rock masses, providing continuous or periodic information even in remote or hard-to-access environments.

Within the Dolomites, the Sas da Lech (Sella Group) represents an example of such a sensitive high-altitude setting. Following recent landslide events, the area was equipped in 2023–2024 with a multi-sensor monitoring system aimed at improving the understanding of the instability processes affecting two fractured rock columns made of Dolomia Principale resting on a Raibl Formation base. This study focuses on the analysis of the seismic and electrical measurements collected at the site, together with meteorological observations and long-term climatic data, to investigate how variations in external conditions influence the thermo-mechanical behaviour of the rock mass.

2. Applied geophysics theory

Applied Geophysics aims to characterize the subsurface structure and investigate Earth's processes in response to natural forces and human activities. It can be applied to a wide range of problems at local, regional, and global scales, also contributing to the monitoring of environmental processes and phenomena.

Geophysical methods were not originally designed specifically to study climate change, but they are increasingly applied in this context, since many climate-change-related processes occur near the surface, where geophysical techniques are most effective for detecting them. They are now used in climate change evaluation, monitoring, and in mitigation and adaptation tasks.

At regional and local scales, the main geophysical targets related to climate change are inland waters, mountain glaciers, and permafrost, as they are among the most reliable indicators of climate change due to their sensitivity to temperature variations.

Geophysical methods are generally non-invasive, but subsurface conditions are reconstructed indirectly, and the obtained results strongly depend on the contrast in the measured physical parameters. At the same time, these methods can cover wider investigation areas and depths while reducing time and costs.

Seismic, electrical, and electromagnetic methods are among the most applied and well-established geophysical techniques.

2.1 Passive seismics

Passive seismology is the branch of seismology that studies the Earth's interior using geophones, which record seismic waves generated by natural sources. Passive seismic equipment has the advantage of being compact and lightweight, and it does not require the artificial generation of elastic waves. A typical setup consists of a high-sensitivity triaxial low-frequency geophone coupled with a digitizer for data acquisition and storage, a battery, and a GPS antenna to ensure accurate timing between different stations. These geophones record wave velocities along three components (vertical, south-north, and west-east).

A key application of passive seismology is Ambient Vibration or Environmental Seismology, which focuses on the mechanical vibrations originating from external processes such as human activities or environmental forces. These vibrations, often referred to as Ambient Seismic Noise (ASN), are commonly considered an unwanted component in active seismic prospecting but provide valuable information in passive studies.

The standard method for quantifying seismic background noise is to calculate the noise Power Spectral Density (PSD) (*McNamara and Buland, 2004*). The most common method for estimating the PSD for stationary random seismic data is the "direct Fourier

transform" (or "Cooley-Tukey method"). The method computes the PSD via a finite-range Fourier transform of the original data. In general, a finite range FFT of a periodic time series $y(t)$ is computed as:

$$Y(f, T_r) = \int_0^{T_r} y(t) e^{-i2\pi ft}\, dt, \tag{2.1}$$

where T_r is the length of each time series segment and f is the frequency. Segmentation into segments of length T_r is a preprocessing step used to reduce the variance of the final PSD estimates.

For discrete frequency values f_k, the Fourier components are defined as:

$$Y_k = \frac{Y(f_k, T_r)}{\Delta t}, \tag{2.2}$$

for $f_k = \frac{k}{N\Delta t}$ when $k = 1, 2, ..., N-1$, where Δt is the sampling interval and N is the number of samples in each time series segment, $N = T_r/\Delta t$.

Finally, the PSD is computed as the square of the amplitude spectrum with a normalization factor of $\frac{2\Delta t}{N}$, following:

$$P_k = \frac{2\Delta t}{N} |Y_k|^2. \tag{2.3}$$

Processing techniques applied to ambient seismic data include spectral analyses such as the Horizontal-to-Vertical Spectral Ratio (HVSR), cross-correlation of ambient noise to derive temporal variations in seismic velocity (dV/V), and microseismicity analysis. These methods can be applied for monitoring purposes, and their main targets related to climate change include landslides, geological structures such as cliffs and rock columns (as in the present case study), mountain and rock glaciers, hydrogeological systems, geothermal reservoirs, and Carbon Capture and Storage (CCS) plants. Monitoring is achieved by analyzing seismic waves to detect changes in resonance frequencies and seismic velocities, as well as by examining microseismic events.

2.1.1 H/V

The Horizontal to Vertical Spectral Ratio (HVSR or H/V) is an experimental method used to estimate the fundamental resonance frequency of a site. It requires computing the ratio between the amplitude spectra of the horizontal (east and north) and vertical components of ambient seismic noise recorded at a single-station site or using a site–reference configuration involving multiple stations.

The method was first introduced by Nogoshi and Igarashi in 1971 and later widespread by Nakamura (*Nogoshi and Igarashi, 1971, Nakamura, 1989, Nakamura, 1996, Nakamura, 2000*). These authors pointed out the correlation between the H/V peak frequency and the fundamental resonance frequency of the site.

The application of this technique to glaciers is relatively recent. It is mainly used in geotechnical and civil engineering applications to detect contrasts in acoustic impedance (the product of density and P-wave velocity) between soft soil and the underlying bedrock or hard rock, where resonance is related to stratigraphy. In contrast, in landslide and rock column applications, resonance arises from the potentially unstable rock block itself.

The concept of resonance applied to gravitational instabilities develops from the analogy between unstable sites and a simple oscillator characterized by fundamental a resonance frequency f_1 that, following Equation 2.4, increases with stiffness K and decreases with the mass M of the system (*Colombero et al., 2021*).

$$f_1 = \frac{1}{2\pi}\sqrt{\frac{K}{M}} \tag{2.4}$$

Similar to Equation 2.4, in the case of a prone-to-fall compartment (Figure 2.1), resonance frequencies are functions of its mass (a function of volume and density ρ) and of mechanical properties such as the internal stiffness (K_b) of the unstable compartment, which can be described by the Young's modulus of the bulk material (E_b), and the stiffness at the contact between the stable rock mass and the unstable compartment (K_c). K_c is a function of fracture properties (e.g. depth z, width L, roughness, filling material, and presence of intact rock bridges) and is therefore usually difficult to describe and quantify.

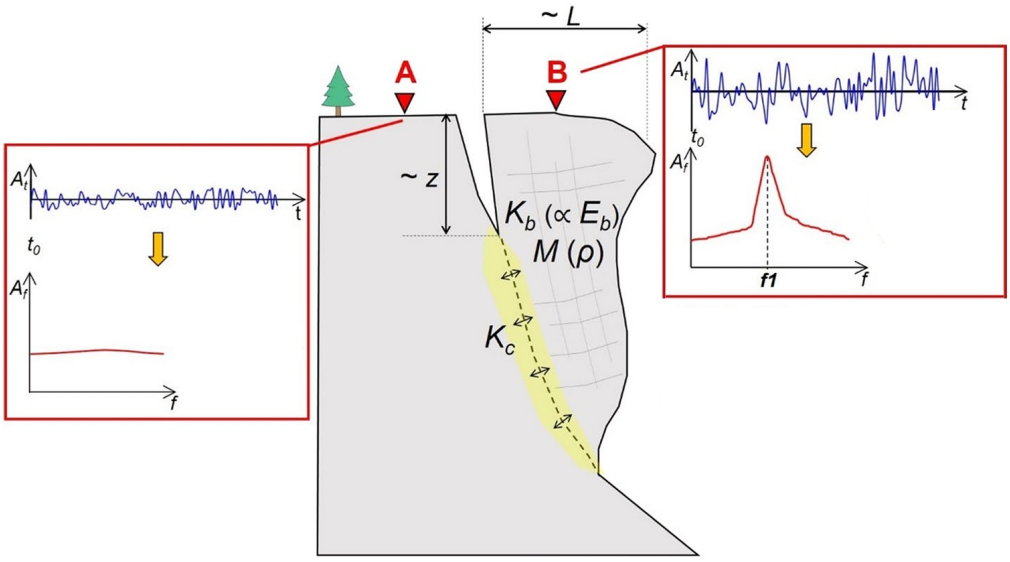

Figure 2.1: Schematic representation of the spectral analysis of ambient seismic noise recorded at an unstable site (A: stable reference station, B: station on unstable column). Station A does not show spectral amplifications. The resonance frequency (f_1) of the unstable compartment is extracted from the power spectral density (PSD) of the noise recorded at station B. Geometric and mechanical parameters are defined in the text. Modified from Colombero et al. (2021).

For example, Valentin et al. (2017) performed 2-D numerical modeling of a rock column isolated by a single vertical rear fracture to assess the pertinent and applicable parameters that could be extracted from ambient vibrations and used to gain information on a prone-to-fall column in stiff rock conditions. They found that the first bending resonance frequency f_1 depends on both the column geometry (thickness L and depth z, in m) and the rock Young's modulus E_b (in GPa), following:

$$f_1 = 44.696 L^{0.486} z^{-1.507} E_b^{0.49} \tag{2.5}$$

Following Equations 2.4-2.5, irreversible drops in f_1 values can be interpreted as a loss in internal or contact stiffness and therefore as potential precursors to failure. Hence, continuous monitoring can be used as an early-warning system. However, even if failure

does not occur, minor reversible fluctuations in resonance frequency are systematically reported in the literature. These fluctuations are interpreted as a consequence of changes in meteorological parameters (mainly air temperature T and precipitation P), which may modify the internal properties of the unstable compartments over different timescales. These reversible modifications in f_1 can vary in magnitude and delay on daily and seasonal scales, and their behavior in response to meteorological factors is not ubiquitous but site-dependent. In Colombero et al. (2021), it was found that the range of variation of f_1 in time due to reversible effects (1 to 12%) partially overlaps the range of irreversible changes observed prior to failure (7 to 50%). It is therefore essential to assess and understand the T- and P-driven reversible fluctuations of the seismic parameters at a given site.

Resonance frequency values can be derived from the peaks in the power spectral density (PSD) of continuous noise recordings. Spectral ratios (H/V) may be used complementarily to enhance the spectral peaks characterizing the site.

2.1.2 Microseismicity

Microseismicity refers to the occurrence of small-scale seismic events that can be generated by different phenomena such as local rock failure, glacier slip, or regional and local earthquakes. All of these processes release elastic waves that can be recorded by geophones. Unfortunately, not only natural phenomena are recorded; vibrations caused by human activity or electromagnetic transients can also be detected. Another type of detected event is rain droplets near the sensors, which, although of natural origin, are not of interest in a geophysical study.

In applied geophysics, microseismicity analyses are generally devoted to the detection, classification, and source location of short-duration events related to ongoing processes at a given site, and have increasing applications in the fields of landslide monitoring and natural hazard assessment. The processes of main interest are those of fracturing and slipping. Indeed, the detection of these events, together with the analysis of their temporal rate and source locations, can potentially provide useful information on the acceleration toward failure and the identification of prone-to-fall compartments and slip surfaces. These microseismic (MS) events are extracted from ambient seismic noise recordings by means of detection algorithms. After detection, event classification can be performed in different ways:

- visual classification based on event spectrograms (i.e. representation of the spectrum of frequencies of a signal as it varies with time);
- automatic classification based on:
  - clustering of time- and frequency-domain signal parameters;
  - supervised or unsupervised machine learning approaches.

2.2 Electrical methods

2.2.1 ERT

Electrical Resistivity Tomography (ERT) is an active electrical method used to determine the subsurface resistivity distribution. This method is commonly used in applied geo-

physics in water environments and permafrost research for the characterization of glacial and hydrological processes and features. Its application in these fields is related to the fact that a marked increase in electrical resistivity occurs at the freezing point, making ERT very effective in imaging the variation in electrical resistivity in the subsurface and in detecting, localizing, and characterizing structures containing frozen material.

The electrical resistivity of a material is a number describing how much that material resists the flow of electricity. It is measured in units of ohm·meters ($\Omega\,\mathrm{m}$) and represented by the Greek letter ρ. In ERT, this propriety is investigated by injecting direct electrical current (I) into the subsoil and the measurement of the consequent voltage distribution at the surface. The current is injected through a dipole of electrodes, called current electrodes (A and B), while the resulting voltage difference (ΔV) is measured at two potential electrodes (M and N).

The electrode spacing affects the depth at which the injected current penetrates and hence the depth of investigation, having consequences on data resolution and field logistics. The greater the electrode spacing, the greater the depth of investigation and the lower the data resolution near the surface (*Pace et al., 2024*). However, in mountain areas, the array length can be an issue due to the complex orography, which can lead to limited investigation depths.

To acquire apparent resistivity, different electrode configurations can be used; the most common ones are the Wenner–Schlumberger (with current electrodes A and B outside the potential electrodes M and N) and the Dipole–Dipole (with the the current electrode dipole A–B adjacent to the potential dipole M–N) (Figure 2.2). While the first is more sensitive to the vertical layering of the subsoil, Dipole–Dipole is sensitive to lateral resistivity contrasts.

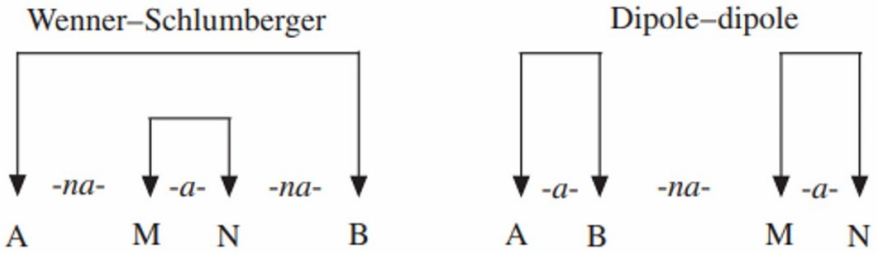

Figure 2.2: Possible ERT array configurations. A and B are current electrodes, while M and N are potential electrodes.

Since the measured voltage is influenced by the current flowing in the subsoil, which in turn depends on rock types, porosity, water saturation, salinity and temperature, weathering, metallic content, and clay content (*Pace et al., 2024*), the apparent resistivity ρ_a is computed from the known current and measured voltage difference as:

$$\rho_a = K \frac{\Delta V}{I} \tag{2.6}$$

where K is a geometric factor that depends on the arrangement of the four electrodes (array). This calculated resistivity is called "apparent resistivity" since it is not the true resistivity of the subsurface. ρ_a equals the true resistivity only for a homogeneous subsurface; for heterogeneous resistivity distributions in the ground (as in this case study),

the resistivity can be derived from the measured apparent resistivity values using inversion methods.

Different codes and software are available for the inversion of electrical data. The inversion process is iterative: the model results are compared with the experimental data, and the model parameters are adjusted at each iteration to minimize the differences (misfit) between measured and calculated values. Generally, a least-square solutions for the misfit minimization is adopted.

Starting from the known geometry of the electrodes, an initial resistivity model is computed, and a pseudosection of apparent resistivity is generated. Since the exact depth of measurement is unknown (the voltage is recorded at the midpoint of the quadrupole), the results are expressed in terms of a pseudo-depth. Once convergence is achieved, the final model provides the best-fitting resistivity distribution with respect to the observed data.

For monitoring purposes, time-lapse experiments can be carried out, where 2D resistivity surveys are repeated over the same line at different times. Using fixed-electrode arrays allows the repetition of identical measurements with the same geometry, enabling a consistent comparison of resistivity variations over time.

3. Case study: Sas da Lech

Due to several landslide events occurring in the past years, as the one occurred the 9th September 2018 (Figure 3.1), registered with code IFFI 69090100 (*Provincia Autonoma di Bolzano, 2018*), between summer 2023 and summer 2024, high-technology instrumentation has been installed at the base of the Sas da Lech north rock columns in order to understand and monitor the movement of the columns themselves.

Figure 3.1: NNW face of the Sas da Lech, before (left) and after (right) the landslides occurring in 2018. (*Google, 2025*).

The main aim of the project is to study thawing of permafrost, which affects high-altitude Alpine environment and it is a predisposing factor for landslide events. Permafrost thawing, which could be related to climate change, has indeed potential impacts on slope stability and can contribute to the occurrence of related hazards, hence the importance of monitoring.

The monitoring activities are supported by a group of geologists from the Office for Geology and Building Materials Testing of the Autonomous Province of Bolzano, and were financed by two main projects.

The installation of instruments, such extensometers and temperature probes, was possible thanks to the funding coming from the PNRR program, allocated by MUR (Ministero

dell'Università e della Ricerca) for the "Geoscience IR" project, coordinated by ISPRA. The aim of that project is the realization of an integrated system of research and innovation infrastructures to improve territorial monitoring (*Istituto Superiore per la Protezione e la Ricerca Ambientale (ISPRA), 2022*). While geophones were financed thanks to the project "THEROCKLAB", funded by the Italian National Research Program PRIN 2022 and involving Politecnico di Torino, Università di Milano-Bicocca, Sapienza Università di Roma, and Università di Bologna (*Politecnico di Torino, 2025*). This project focuses on the study of thermo- and hydro-mechanical processes affecting fractured rock masses, through multisensor monitoring and modeling approaches at five different sites in Italy. The Sas da Lech site was selected as a field lab in order to monitor rock wall processes associated with permafrost degradation. In particular, the installed instrumentation is aimed at studying the seasonal evolution of ice and permafrost, the associated rock-mass deformation, and the resulting instabilities.

3.1 Geographical setting

The Sas da Lech is a rock formation located on the northern side of the Sella Group in the Dolomites, Autonomous Province of Bolzano (south Tyrol, northern Italy).

The formation is located within a periglacial environment, characterized by the presence of a buried ice mass (the Murfrait rock glacier) and a proglacial lake (Lech dl Dragon). The latter has been under monitoring since 2004 due to ice melting and the subsequent large amounts of thawed debris, which caused debris flows affecting the road at Passo Gardena (*De Pascale, 2023*). To the west lies the Rifugio Franco Cavazza al Pisciadù (at an altitude of 2587 m), situated at the foot of the Pisciadù Peak and next to the crystal-clear lake having the same name. The hut is open only during the summer season due to adverse weather conditions and limited accessibility in winter, when the area is covered by snow. However, it represents an important destination for hikers in summer and serves as a logistical support point for the monitoring activities, thanks to the presence of a helipad that allows equipment to be transported and installed more easily at such an high altitude.

The monitoring site is located at the base of the north face of the Sas da Lech rock formation, at an elevation of 2720 m (see orange marker in Figure 3.3). An overview of the monitoring site is shown in Figure 3.2.

Figure 3.2: Overview of the monitoring site, with Piz Pisciadù on the left and the Sas da Lech in the center and Sass dai Ciamorces behind it.

Over Piz Pisciadù is actually present a mountain meteo station "Badia Cima Pisciadù meteo station" which has been used in the analyses of the data acquired at the monitoring site as well as other two meteo stations, located in the valley side, "Selva di Val Gardena" and "Corvara" meteo stations. The three of them are reported with a blue marker in Figure 3.3.

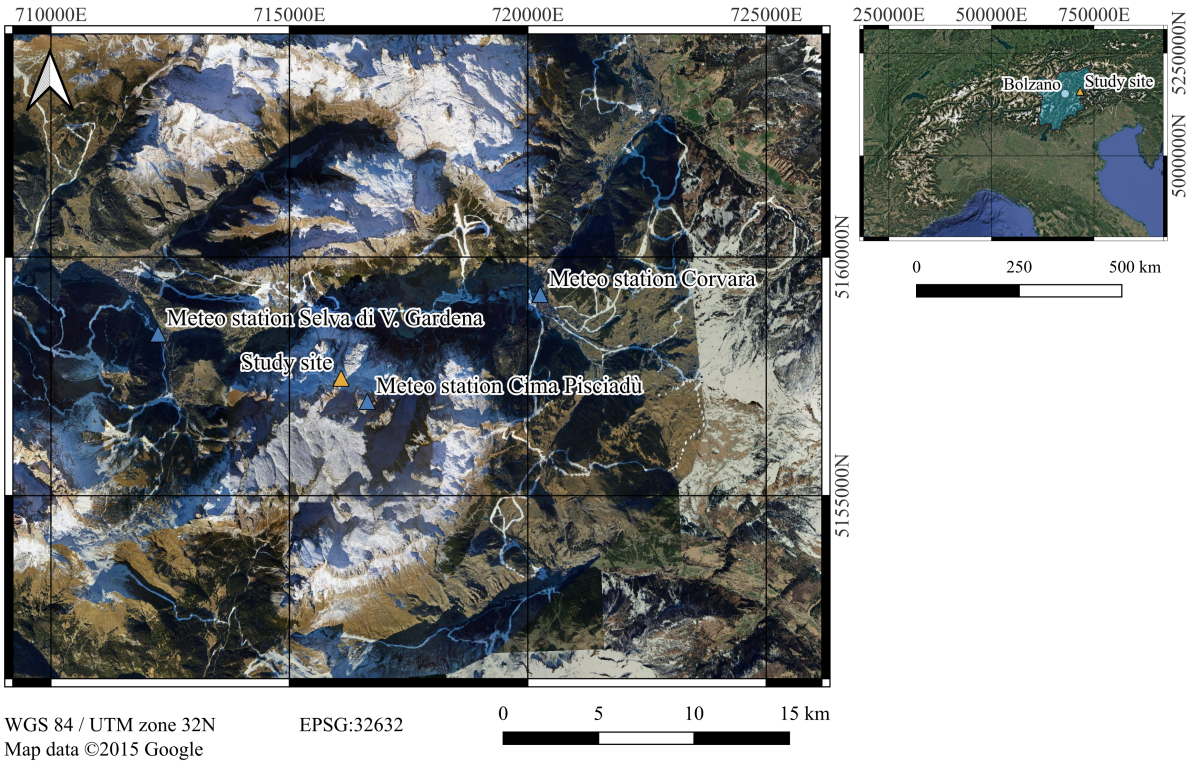

Figure 3.3: Spatial allocation of the region of interest. The study site is shown as an orange marker, while the available meteo stations are displayed in blue (*QGIS Development Team, 2023*).

3.2 Geological setting

The Dolomites form the central-northern portion of the Southern Alps, a non-metamorphic, south-vergent thrust belt belonging to the much larger Alpine Chain and resulting from the comparatively gentle deformation of a passive continental margin of the Mesozoic Tethys Ocean (*Stefani et al., 2004*). The Sas da Lech belongs to the Sella Massif of the Dolomites, a high-relief postvolcanic carbonate platform (with respect to the Middle Triassic magmatic events), with an atoll-like geometry, made up of two superimposed carbonate platforms (represented with blue and pink color in Figure 3.4).

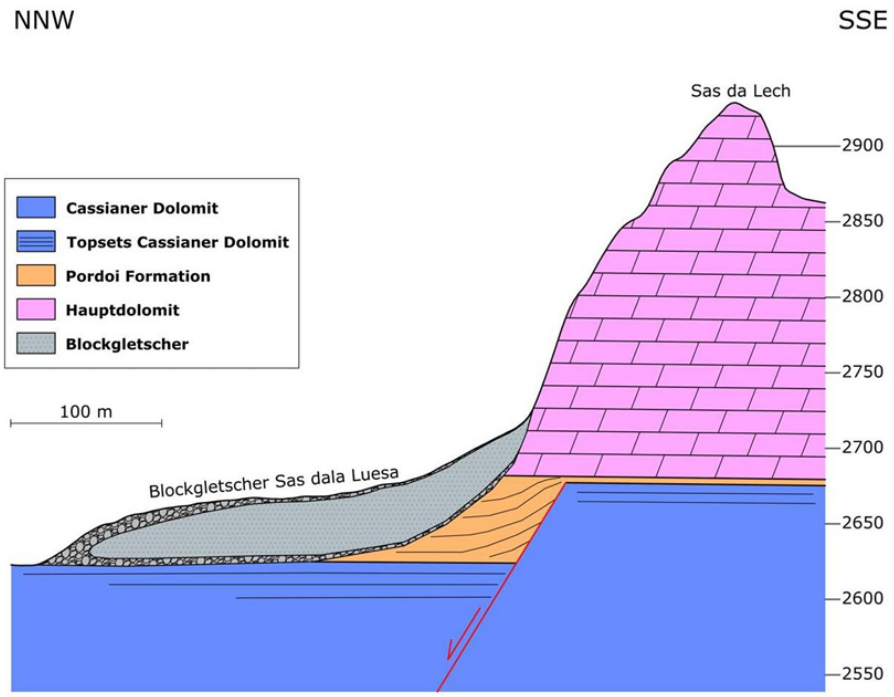

Figure 3.4: Geological profile across the summit of the Sas da Lech (*Mussner, 2009*).

The lower platform, Cassian Dolomite (Cassianer Dolomit), consists mainly of clinostratified slope deposits and is separated from the upper one by a ledge of Raibl Group, an alternation of Dolomites, marly Dolomites, lighter stromatolithic Dolomites, and greenish marls and/or clay shales (*Mussner, 2009*). The Raibl Group in the western Dolomites is composed of several formations such as the Travenanzes Formation, the Heiligkreuz Formation with its Lagazuoi, Falzarego, Fedares, and Dibona members, and the Pordoi Formation. The latter represent the Raibl in the area of the Sella Massif; one rare outcrops of the latter is actually present just below the base of Sas da Lech. Despite that, its conditions are not that good due to the presence of debris, talus and rock glaciers.

The upper platform, instead, is made up by the Dolomia Principale (Hauptdolomit or Main Dolomite). In the study area, it is, together with the Cassian Dolomite, the most most important rock-forming units and the highest parts and peaks of the Sella Massif are composed of Dolomia Principale. Thickness of the Main Dolomite reaches maximum values of about 250 m. The Dolomia Principale consists of flat lying region-wide peritidal deposits. Lithologically, it consists of a cyclic succession composed of meter-thick lime mudstone beds with bivalves (mainly megalodonts) and gastropods (Worthenia) and thin

stromatolitic beds; locally, thin breccias and marly layers are intercalated (*Krainer et al., 2012 - Mussner, 2009*).

The fracture network is likely of tectonic origin, as the structures display consistent orientations over wide areas and at multiple sites. However, the fractures may have subsequently been enlarged by karstification during periods of carbonate platform exposure, and some of them may even have developed later as new karst shafts. The filling of the fractures has been classified by *Keim and Brandner, 2001* as follows:

- mixed carbonate-volcaniclastic components in a greenish-marly matrix for mostly vertical fractures, up to several decimeters thickness and few tens of meters of depth
- brownish arenitic Dolomites, partially with greenish marls
- unsorted angular clasts (cm- to m-sized) embedded in a greenish-marly matrix for large fractures up to about a hundred meter wide

The faults setting of the area is visible in figure 3.5, where in black is highlithed the synsedimentary fault which across the Sas da Lech; indeed, in the east face of the Sas da Lech there is a normal fault within the Cassian Dolomite 3.6. Due to the presence of this fault, there is a marked thickness jump in the Pordoi Formation and it likely influences data collected at the monitoring site.

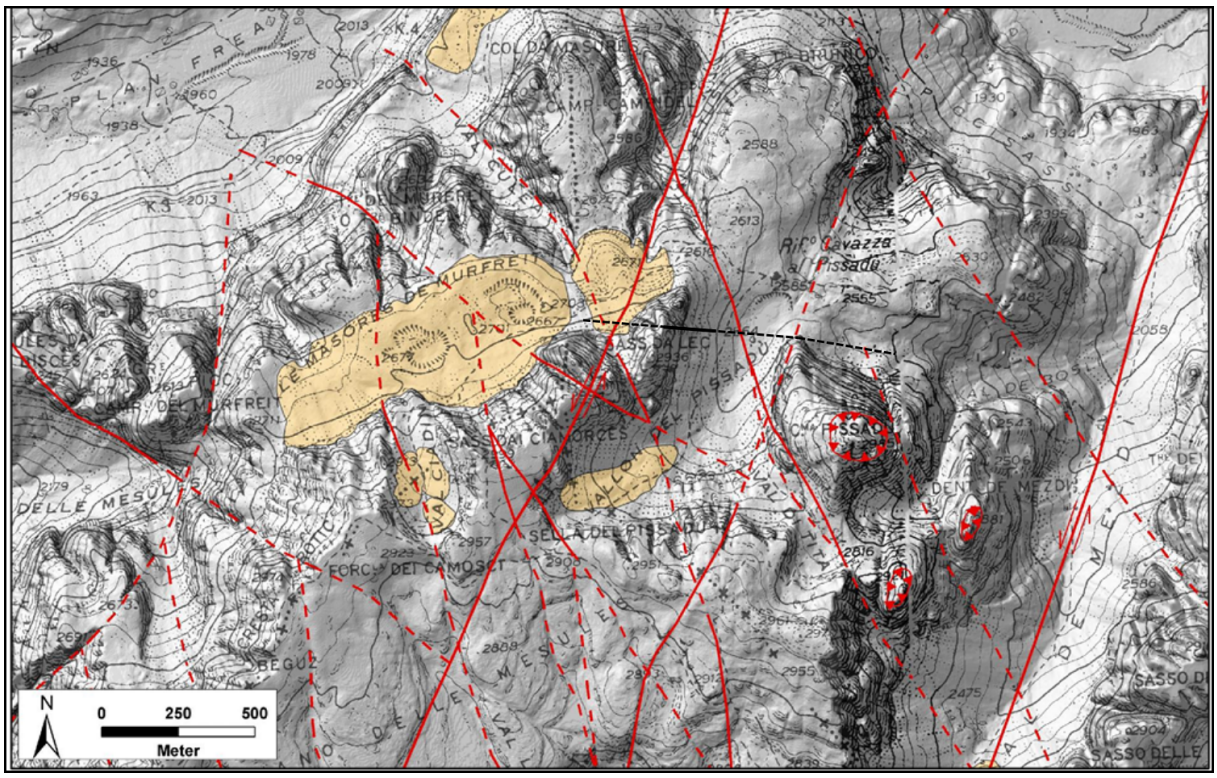

Figure 3.5: Faults and rock glaciers map of the Sella N-side. Most of the faults are small-offset strike-slip faults formed during the Neoalpine phase (*Mussner, 2009*, modified). Faults: General fault (solid red line) and Suspected fault (dashed red line). Reverse/thrust fault (red triangles). Is here highlighted also the Paleo-faults of Carnian age Normal fault (solid black line) and Presumed normal fault (dashed black line) crossing the Sas da Lech.

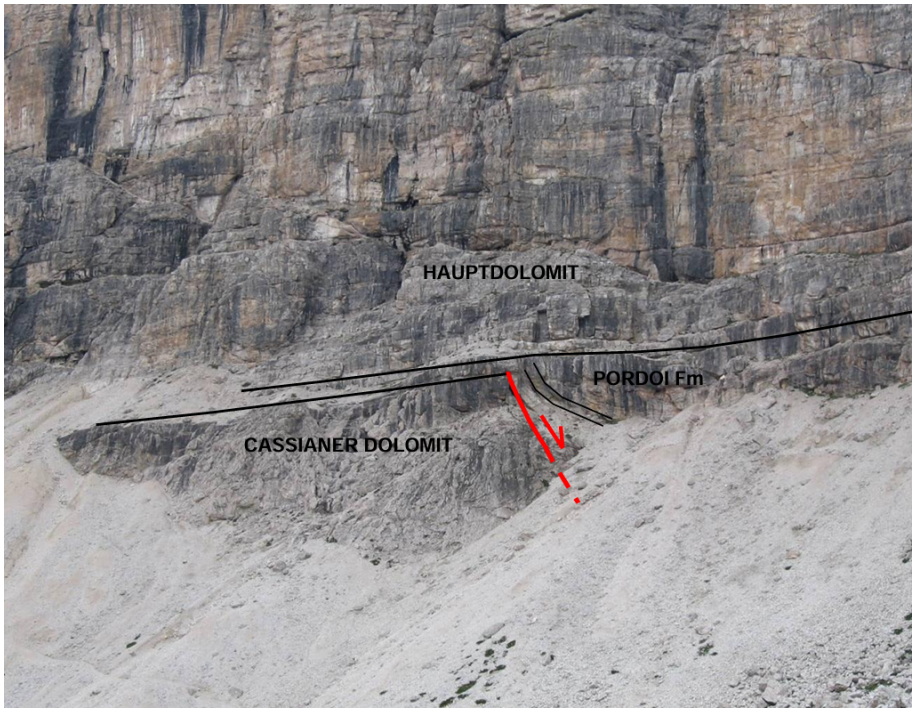

Figure 3.6: The normal fault in the Cassian Dolomite on the East face of the Sas da Lech (shown in red).

The presence of faults in the area causes structural weakening of the stratigraphic unit, making the rocks more easily eroded; hence the rock fragmentation observed in the study site enhances the efficiency of frost weathering, leading to abundant debris production *Antonellini and Mollema, 2000*. Furthermore, the steep Main Dolomite walls provide sufficient shading and along with debris production, under favorable climatic conditions, controls the formation of rock glaciers in the northern Sella, ultimately resulting in the development of the ice-cemented Murfreit rock glacier, located just northeast of Sas da Lech.

3.3 Instrumentation setup

Most of the instrumentation present at the Sas da Lech monitoring site was mounted during summer 2023. At the moment, on the site there are three different extensometers, two thermometric columns and four geophones.

Figures 3.7-3.8 illustrate the spatial distribution of the installed instrumentation.

Figure 3.7: Schematic representation of the locations of the instruments within the monitoring site: geophones (GEA06, GEA07, GEA11, GEA12), extensometer (E21), multiparametric columns (DMS1, DMS2) and electrodes (e1-e48).

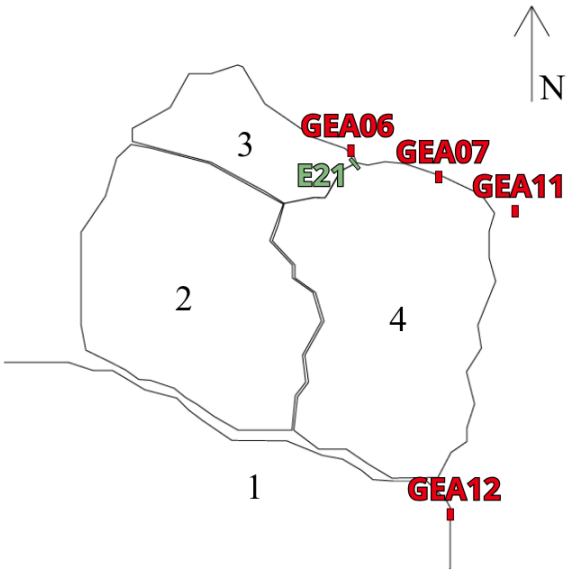

Figure 3.8: Schematic top view of the monitoring site. Geophones are shown in red, while extensometer 21 is shown in green (monitoring what is hereafter referred to as the main fracture, between blocks 3 and 4). Rock block 1 is stable, block 2 collapsed in 2018, block 3 is monitored by GEA06 (hereafter referred to as the northern rock column), and block 4 is monitored by GEA07 (hereafter referred to as the eastern rock column).

Extensometers are used to evaluate deformations in three different fractures; actually

just extensometer 21 was considered in this analysis being the only one in the main vertical fracture between two of the installed geophones. It was installed just in 2024, hence data of deformation and of air temperature are available just since 22th July 2024.

Thermometric columns are multiparametric columns DMS made of twenty modules, one at each meter, going from the 19th which is the nearest to rock face, to the 1st which is the deepest. Each module is equipped with temperature, inclinometric and accelerometric sensors. These columns were installed almost horizontally but due to the internal morphology the exact location inside the rock columns is not known. Thanks to them there are, since 3rd August 2023, data of rock temperature at different depth at the two locations where they are installed. Moreover, they provide deformation information for each module, that are actually under analysis of the Geologist group of the University of Milano Bicocca.

As far as regard geophones, instead, a network of four wireless passive monitoring stations was installed at the column base (GEA06, GEA07, GEA11 and GEA12). Specifically, GEA06 is installed on the Dolomia Principale at the base of the northern rock column, while GEA07 is also located on the Dolomia Principale but at the base of the eastern column. The deployment of GEA06 and GEA07 at the bottom of the two columns is not an optimal condition to monitor their resonance and behaviour. Indeed, higher noise amplifications are expected on the top of the columns. However, the installation in other positions was not possible due to the site conditions. GEA11 is positioned on the Raibl Formation, whereas GEA12 is placed on the Raibl Formation within the stable compartment of the Sas da Lech and is mostly buried. A schematic representation of their location is presented in Figure 3.9.

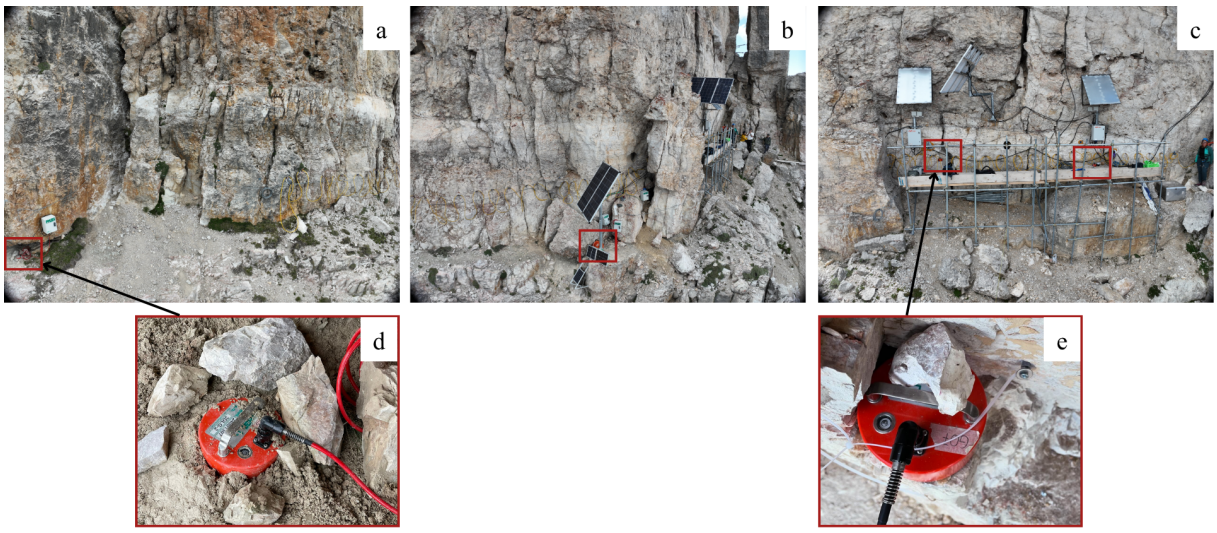

Figure 3.9: Location of the geophones at the monitoring site. Panels (a)–(c) show photographs from the photogrammetric survey, arranged from the easternmost to the northernmost viewpoints. The precise locations of the geophones are highlighted with red rectangles. (a) GEA12, installed on the Raibl Formation within the stable compartment, with a close-up view in (d). (b) GEA11, positioned on the Raibl Formation. (c) GEA07 and GEA06, both installed on the Dolomia Principale but located on two distinct rock columns. (e) Close-up view of GEA07.

Each station included a 2 Hz triaxial high-sensitivity geophone (200 V/(m/s)) and an on-purpose designed digitizer/recorder (GEA–GPS, developed by PASI s.r.l. and Iridium Italia s.a.s.) ensuring continuous seismic noise recording at 250 Hz sampling rate,

low-weight of the instrumentation to reach remote areas, low power consumption in the absence of an external power supply (approximately 30 days of autonomy) and daily remote information about the system state of health by a GSM–GPRS module. At the monitoring site, 70 W of solar panels were installed on the South-East face in order to avoid autonomy problems. Synchronization between the different stations is provided by GPS timing. Data are stored in 1 h files in an internal 32 GB memory card. Unfortunately, they were designed to not support a larger memory and as a consequence, according to the data collected, about every three months they are full. This fact requires the operators intervention every three months on the site, that is not always possible due to the inaccessibility of the site itself from late fall to late spring. For this reason, from their installation on September 2024, there is a gap in the seismic data from December 2024 and June 2025. From now on the analysis will refer to "period 1" and "period 2" covering September-December 2024 and June-September 2025, respectively. These instruments allow the characterization of the stability of the Sas da Lech rock columns and provide a continuous monitoring tool to the site.

Table 3.1 reports, for each geophone, the specific time intervals effectively recorded within period 1 and period 2, since the instruments stopped operating at different moments within the two seismic monitoring windows. Those differences are mainly due to temporary losses of GPS tracking or difficulties in acquiring the GPS signal at the beginning of the recording, as well as to occasional internal malfunctions of the geophones.

Table 3.1: Seismic recording intervals within period 1 and period 2 of each geophone.

Geophone	Time coverage [UTC] - Period 1	Time coverage [UTC] - Period 2
GEA06	16/09/24 h14 - 18/12/24 h00	26/06/25 h09 - 27/06/25 h08
GEA07	16/09/24 h11 - 15/12/24 h02	26/06/25 h08 - 04/09/25 h07
GEA11	16/09/24 h15 - 28/09/24 h23	26/06/25 h08 - 04/09/25 h07
GEA12	17/09/24 h09 - 29/10/24 h13	26/06/25 h08 - 05/09/25 h07

Table 3.2 summarizes the available datasets.

Table 3.2: Data available at the monitoring site.

Variable	Time coverage [UTC]	Time resolution	Instrumentation used
Air temperature [°C]	22/07/2024–25/09/2025	30 min	Extensometer 21
Main fracture def [mm]	22/07/2024–25/09/2025	30 min	Extensometer 21
Rock temperature [°C]	03/08/2023–25/09/2025	30 min	Multiparametric columns DMS
Seismic data	16/09/2024–18/12/2024 26/06/2025–04/09/2025	1 h	Geophones

3.4 Meteo stations

Because only air temperature is recorded at the monitoring site, and snow on the panels causes data gaps, meteorological data from nearby stations were used for the seismic analysis (see their location from Figure 3.3).

The nearest meteorological station is "Badia Cima Pisciadù" (*Provincia autonoma di Bolzano — Meteo Alto Adige, 2025*), located at an elevation of 2985 m on the summit of the homonymous mountain, southeast of Sas da Lech. The available data include air temperature (°C), wind speed (m/s), wind direction (degrees with respect to north), and wind gust speed (m/s), all recorded at a 10 minute resolution. The station was installed in June 2023, thus covering both periods of seismic data acquisition.

Unfortunately, precipitation data are not collected at the "Badia Cima Pisciadù" station. Therefore, the two nearest meteorological stations, "Corvara" and "Selva di Val Gardena", were selected instead. Both are located in the valley below the rock formation, at significantly lower elevations (1530 m and 1594 m, respectively). In both cases, precipitation data (in mm) were available starting from 2023, thereby covering the acquisition period, with a time resolution of 5 minutes.

All data downloaded from these stations were provided in Central European Time (CET) format and were first temporally aligned to the UTC time format used in the seismic dataset.

Table 3.3 provides a summary of the meteorological stations and the datasets used in this analysis.

Table 3.3: Details of the meteorological stations selected to download weather data.

	Badia Cima Pisciadù	**Corvara**	**Selva di V. Gardena**
Altitude [m]	2985	1530	1594
Station code	61720WS	61300MS	73500MS
Station type	Mountain	Valley	Valley
Cartographic coordinates (UTM WGS84)	716635 m / 5156974 m	720262 m / 5159216 m	712245 m / 5158389 m
Geographic coordinates	46.5314°N / 11.8250°E	46.5504°N / 11.8733°E	46.5456°N / 11.7684°E
Data time resolution	10 min	5 min	5 min
Downloaded meteorological parameters	Air temperature [°C] Wind speed [m/s] Wind direction [°] Wind gust [m/s]	Precipitation [mm]	Precipitation [mm]

3.5 Data analysis

In this section are reported methods and results of the analysis perfomed on the data available at the monitoring site.

The long-term ambient seismic noise data set acquired at the Sas da Lech was analysed using both spectral analysis and microseismicity techniques while electrical data were inverted to get a resistivity model within the rock medium. To fully understand the detected seismic and electric response, ambient seismic noise spectral analyses results and microseismicity trends were compared with meteorological data measured at the nearest meteo stations (see Section 3.4).

Moreover temperature data were compared with deformation data acquired at extensometer 21 to understand the behaviour of the main fracture dividing the rock columns.

3.5.1 Temperature analysis

Air temperature data at the monitoring site are available at 30-minute resolution and are measured by extensometer 21. First, a data-gap investigation was performed on the temperature dataset measured at the site. It was found that 72 gaps are present, mostly due to snow covering the solar panels, occurring between November 2024 and mid-February 2025.

Then, the on-site temperature was compared with air temperature data measured at the meteorological station “Badia Cima Pisciadù” to assess the representativeness of the station and to better understand the temperature behaviour during the cold months. Both datasets were plotted at 30-minute resolution for the entire period of availability of extensometer 21 data (Figure 3.10).

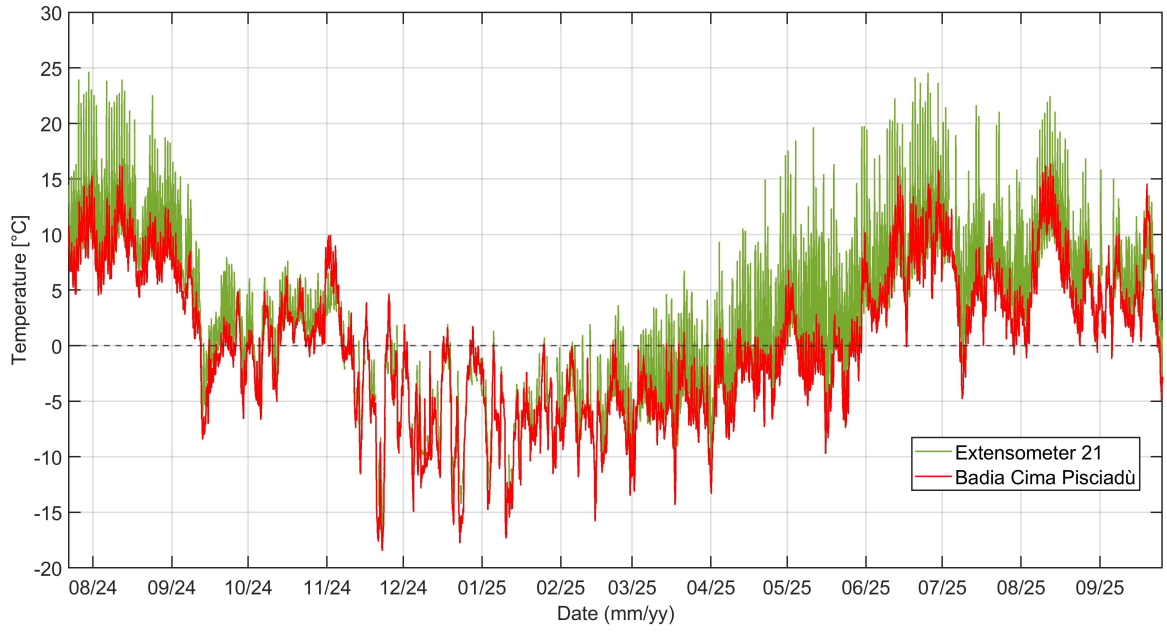

Figure 3.10: Air temperature time series from extensometer 21 and the ”Badia Cima Pisciadù” meteorological station, shown at 30-minute resolution.

It was found that, within the year of available data, the two time series are highly correlated, with an overall correlation coefficient (Pearson) $r = 0.91$. On average, extensometer 21 temperature values show higher mean temperatures and a larger daily temperature range. Indeed, over the period, the mean air temperature measured at the site was 3.27 ± 6.79 °C, while at the meteorological station it was 0.30 ± 6.61 °C, i.e., about 3 °C higher. This result is likely related to the lower altitude (about 265 m) of the Sas da Lech monitoring site but at the same time a longer dataset would make this estimation more robust. Indeed, it is an higher difference than the reported average lapse rate of -0.54 to -0.58 °C/100 m for Italian and French Alpine regions, by Kirchner et al. (2013). The mean daily temperature range was 8.19 ± 4.47 °C at the site and 4.57 ± 1.98 °C at the meteorological station on Piz Pisciadù.

The thermal range appears to be more similar during the cold months; however, these months also include most of the data gaps, and therefore a more complete dataset would be needed to confirm this behaviour. For the same reason, the correlation is slightly lower during this period, as the numerous gaps affect the calculation of the correlation coefficient.

Overall, the air temperature at the "Badia Cima Pisciadù" meteorological station is lower and shows a smaller daily thermal range, but it exhibits a similar temporal trend to the temperature measured at the monitoring site by extensometer 21.

Furthermore, air temperature at the monitoring site was also compared with rock temperature measured at the two multiparametric columns (DMS1 and DMS2). For the comparison, only the most external modules (number 19) were selected (Figure 3.11) since it was observed that rock temperature is mainly affected by external temperature only in the first meter of depth (Figure 3.12); at larger depths, the daily air temperature fluctuations do not seem to lead to changes in rock temperature, as rocks may respond on longer thermal time scales. However, due to the limited time series of air temperature, this behaviour cannot be further investigated. This depth of response is consistent with the 1.5 m depth observed at Senales, where permafrost is monitored by the Geological Office of Bolzano (PermaNET project). There air temperature variations are still perceivable and measurable down to approximately 1.5 m within the rock.

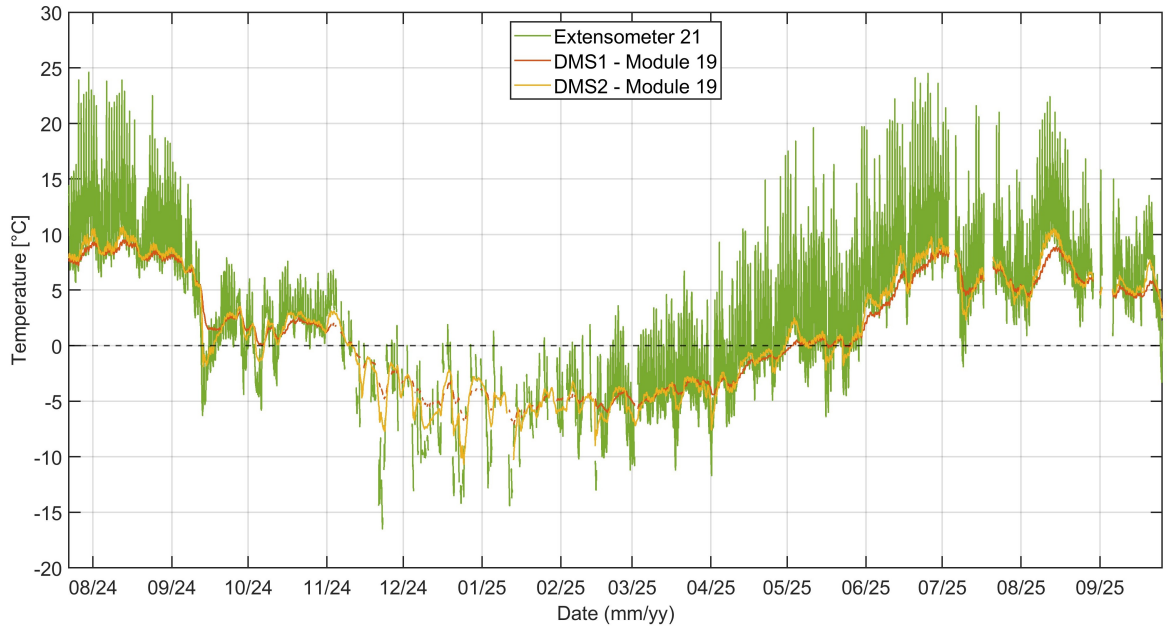

Figure 3.11: Rock temperature time series at the two multiparametric columns (DMS1 and DMS2) compared to air temperature from extensometer 21, shown at 30-minute resolution.

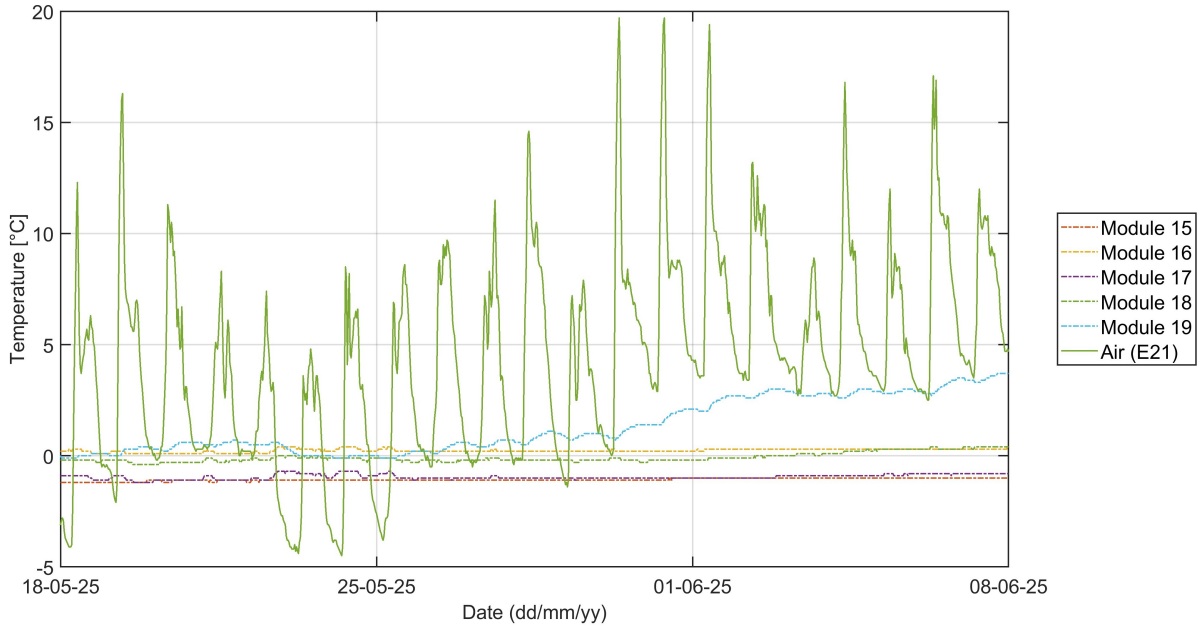

Figure 3.12: Rock temperature time series at the multiparametric column DMS1 at different depths compared to air temperature from extensometer 21, shown at 30-minute resolution. Module 19 is the most superficial one, from the rock surface to 1 m depth; module 15 is the deepest one, going from 4 m depth to 5 m depth. The other 14 modules are not represented here to allow for a clearer visualization of the most superficial modules; however, they showed almost constant temperature throughout the year.

Over the entire period, at the location of DMS1 an average rock temperature of 1.641

± 4.413 °C was measured, while a slightly lower mean value was observed at DMS2 (0.778 ± 5.151 °C). Actually, it can be observed that this difference in the mean value is not constant throughout the year, and it seems that DMS2 rock temperature has a larger range. This is likely due to the fact that it is within the rock column more exposed to solar radiation, being the one facing east. At the daily scale, a delay of 7 hours was found between the external air temperature and the rock temperature response. The analysis at larger scales was not performed due to the limited availability of the datasets.

3.5.2 Main fracture deformation

Since the behaviour of the two rock columns was of interest, their relative movement was analysed using the deformation data measured at extensometer 21. As can be seen in the instrument setup figure (Figure 3.7), the extensometer is located between the two rock columns, and it was installed perpendicularly to the fracture. The same gaps of air temperature were observed since both variables were measured by the same instrument.

Deformation measurements are reported in millimetres, with a 30-minute time resolution. Along with the deformation, also roll, pitch, and yaw angles were measured and available. These three angles were used in order to correct deformation data, via a rotation matrix, so that the corrected deformation value was the one along the original configuration of the instrument, hence perpendicular to the fracture. Unfortunately, the correction was possible only in a small time range due to anomalous values of the yaw angle. Despite that, in the corrected range it was observed that the corrected data were almost exactly equal to the raw ones. Hence, the entire deformation dataset was assumed to represent the true deformation between the rock columns.

Negative values mean that the rock columns are moving closer to each other.

Deformation values were compared to air temperature data measured by the same extensometer (the same one analysed previously) and are reported in Figure 3.13.

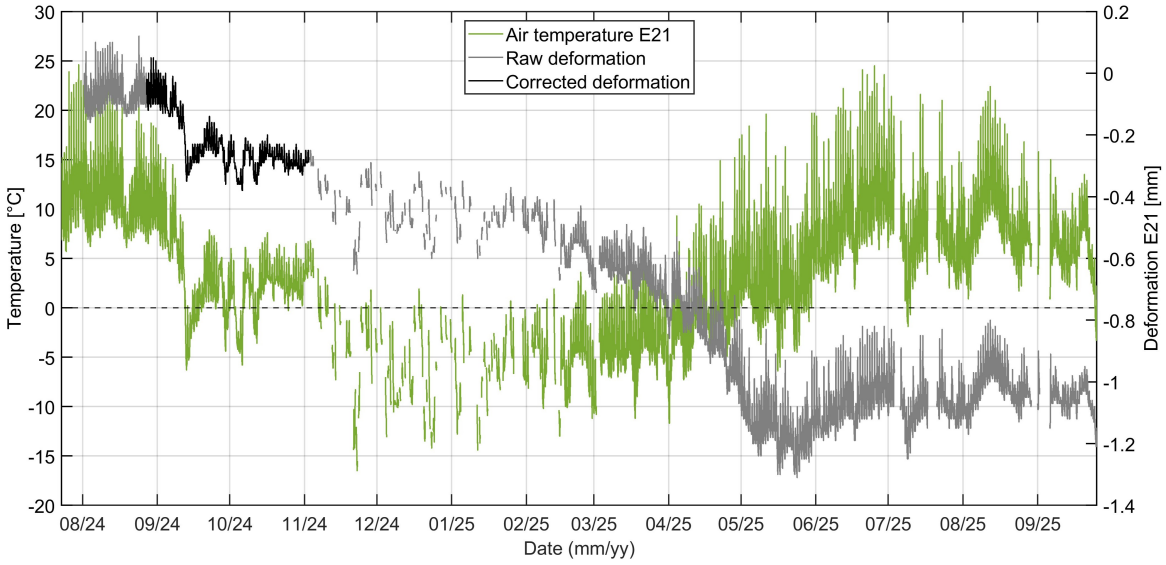

Figure 3.13: Air temperature and deformation time series from extensometer 21 at 30-minute resolution. A dashed horizontal line marks 0 °C. Deformation could be corrected only over a limited interval where rotation parameters were within the valid 0–360° range.

These two datasets were further analysed in order to understand the relation between them at both daily and seasonal scales (Figures 3.14-3.15, respectively).

For the daily scale analysis, temperature residuals were obtained by subtracting a 24-hour moving average (48 samples at 30-minute resolution) from the raw temperature time series. Deformation residuals were computed in the same way by removing their corresponding 24-hour moving average.

For each day of the time series (48 samples per day), the Pearson correlation coefficient between temperature residuals and deformation residuals was calculated, using only non-missing data. For the same daily segments, the time lag (in hours) was determined from the cross-correlation function.

Over the analysed period, air temperature and deformation of the main fracture are highly correlated at the daily scale, and there is almost no time lag in the response of deformation to the external thermal conditions. A slightly lower correlation is observed in cold months, where many data gaps may have affected this result.

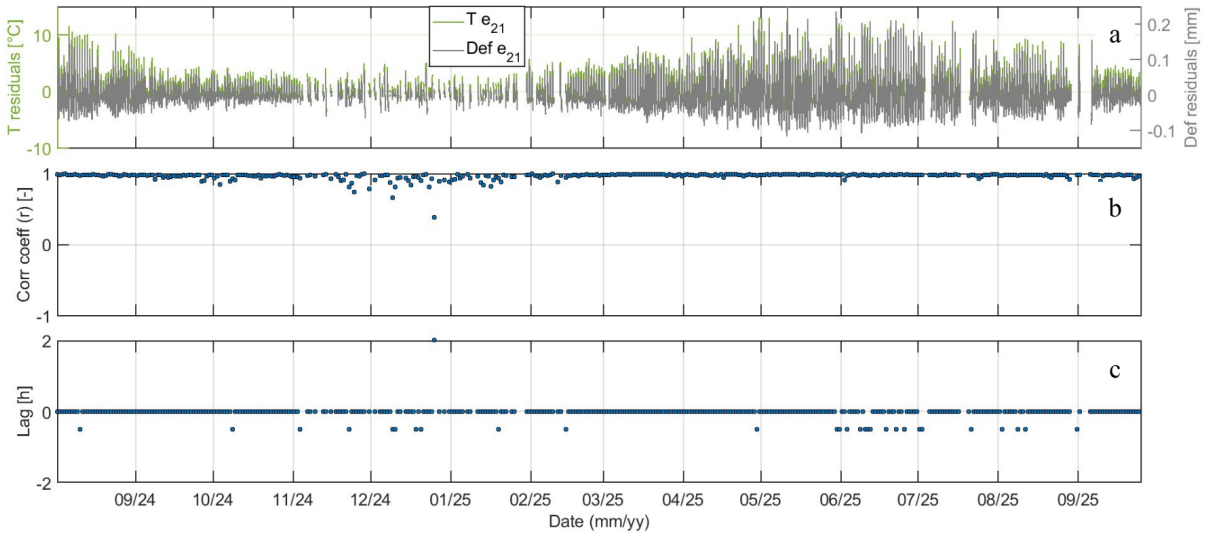

Figure 3.14: Daily-scale analysis of air temperature and deformation at extensometer 21: (a) residual temperature and deformation, (b) daily Pearson correlation coefficient, and (c) lag in hours from the cross-correlation.

At the seasonal scale, to remove daily thermal oscillations, a 30-day moving average was applied to both temperature and deformation time series. To investigate how the correlation evolves on longer time scales, a moving Pearson correlation coefficient was computed using a sliding window of 60 days. Within each window, the correlation was evaluated only when at least 50% of the samples were valid (non-missing).

From Figure 3.15.a it is clearly visible that deformation follows the decrease in air temperature until mid-December. At that point, temperature is below 0°C but starts to increase again, while deformation continues to decrease, indicating a narrowing of the main fracture. Therefore, in cold months a negative correlation is observed, which becomes positive again in late spring whenair temperatures rise above 0°C.

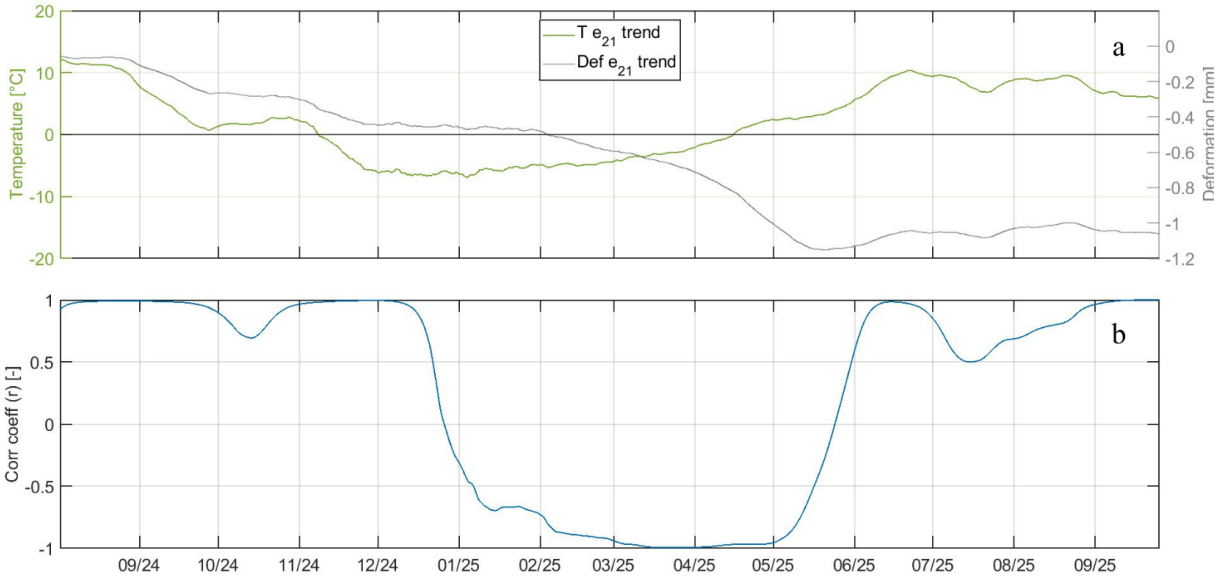

Figure 3.15: Seasonal-scale analysis of air temperature and deformation at extensometer 21: (a) 30-day moving mean of temperature and deformation, and (b) 60-day moving correlation coefficient.

A possible interpretation of deformation data, at seasonal scale and related to the thermal cycles of thawing and freezing, is the following. The Raibl Formation, on which the two rock columns of Sas da Lech are located, consists of an alternation of limestone layers with clayey layers that become imbibed with water. When water freezes inside the imbibed layers, these layers expand. Given the geometry of the site, the expansion occurs mainly in the outer portions, and this causes a rotation of the main overlying dolomite blocks due to a lever effect. A few centimeters of expansion of the layers of the Raibl Formation, concentrated in the first outer decimeters of the layers, are likely sufficient to generate the observed seasonal trend. If this hypothesis of rotation is correct, then a reduction of the fracture occurs when temperatures drop below zero, leading to the decrease in deformation measured by the extensometer. Given the thermal inertia of the rock, a time lag between air temperature and deformation response is observed, visible in the shift between the absolute minimum of temperature and deformation, with a delay of about 5 months.

A similar behavior between deformation and air temperature has been observed by the geological group of the Province of Bolzano at the monitoring site of the dolomitic rock face at Salorno (BZ).

With the seismic analysis, it appears that this movement of the Raibl Formation is more evident below the eastern rock column (detected by GEA07) than below the northern one (see the following sections for further explanation).

3.5.3 Azimuth and frequency

Starting from the continuous noise recording at 250 Hz for each geophone component, the value of frequency associated to the maximum of the horizontal components in the frequency domain was extracted. This operation was performed for each hour of recording in order to identify the dominant vibration mode of the rock columns. Moreover, the corresponding azimuth was extracted (as angle with respect to the north).

Those information were plotted for all the four stations and for both seismic monitoring periods (Figures 3.16-3.19)

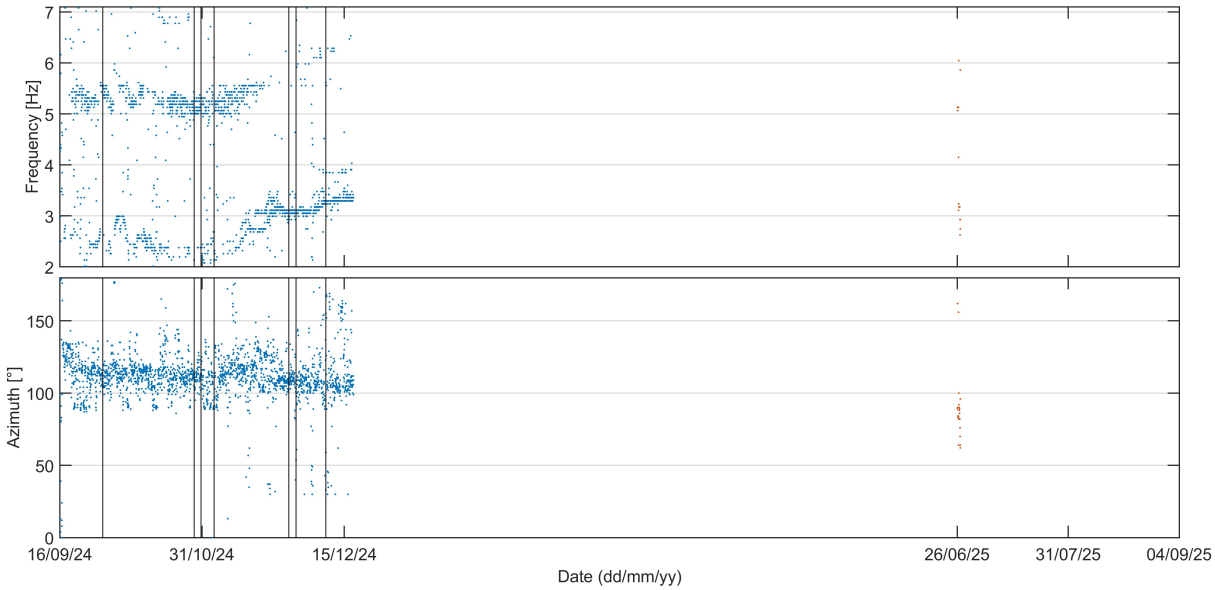

Figure 3.16: Frequency and azimuth analysis for geophone GEA06. Top panel: time series of the frequency associated to the maximum amplitude of the horizontal components. Bottom panel: corresponding azimuth of the extracted frequency. Blue indicates period 1 and orange indicates period 2. White regions represent data gaps whereas vertical black lines represents data gap within both monitoring periods.

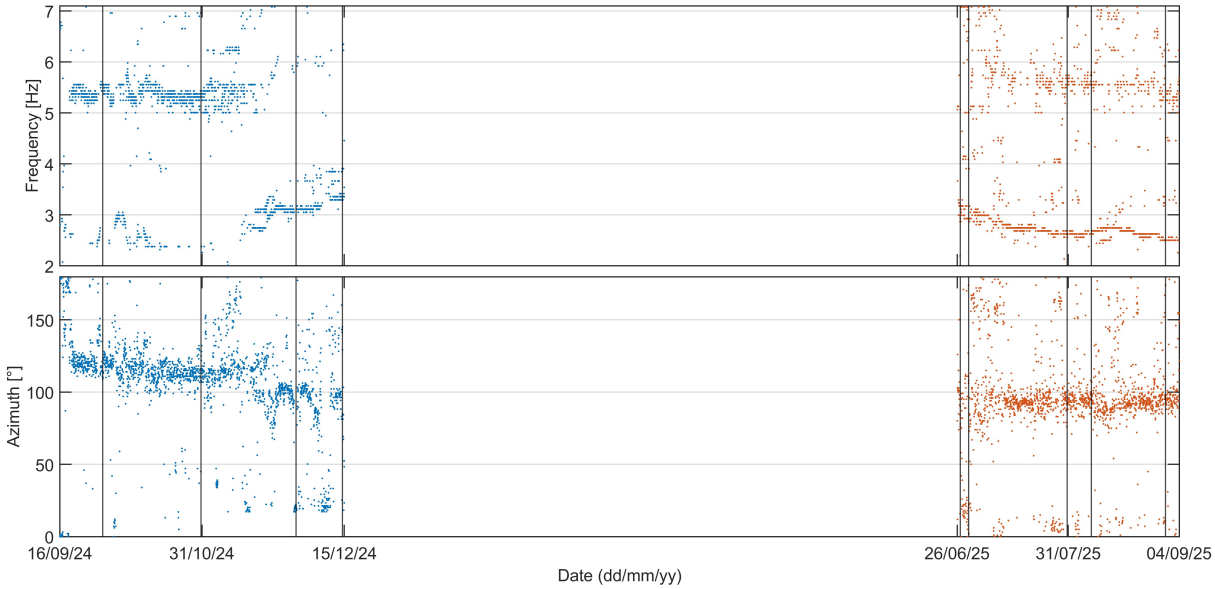

Figure 3.17: Frequency and azimuth analysis for geophone GEA07. Top panel: time series of the frequency associated to the maximum amplitude of the horizontal components. Bottom panel: corresponding azimuth of the extracted frequency. Blue indicates period 1 and orange indicates period 2. White regions represent data gaps whereas vertical black lines represents data gap within both monitoring periods.

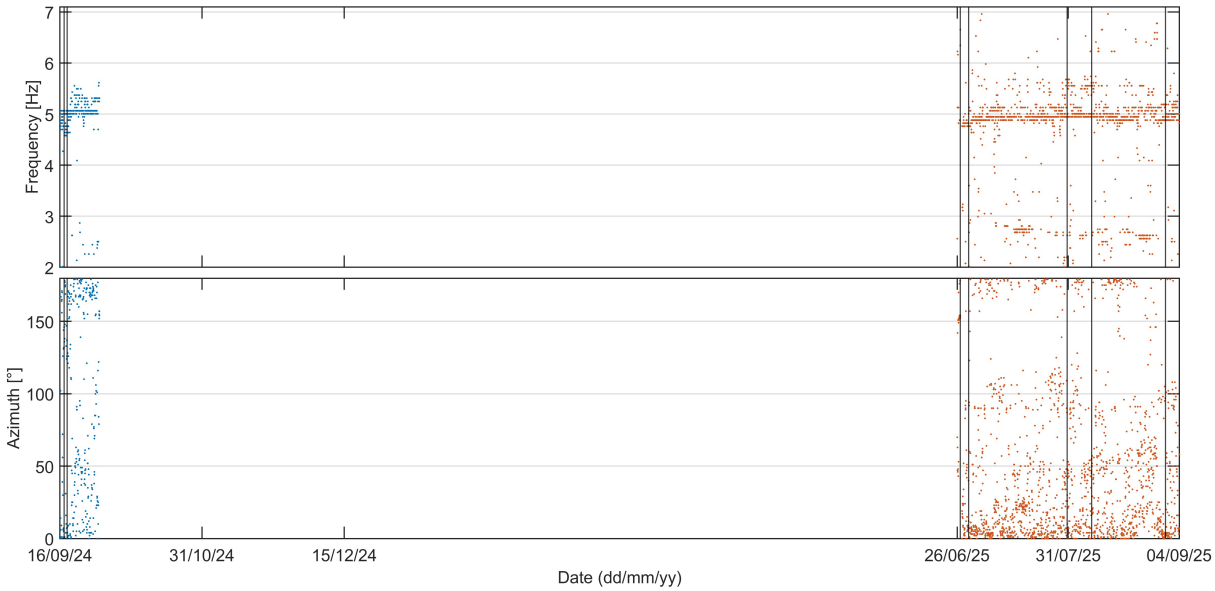

Figure 3.18: Frequency and azimuth analysis for geophone GEA11. Top panel: time series of the frequency associated to the maximum amplitude of the horizontal components. Bottom panel: corresponding azimuth of the extracted frequency. Blue indicates period 1 and orange indicates period 2. White regions represent data gaps whereas vertical black lines represents data gap within both monitoring periods.

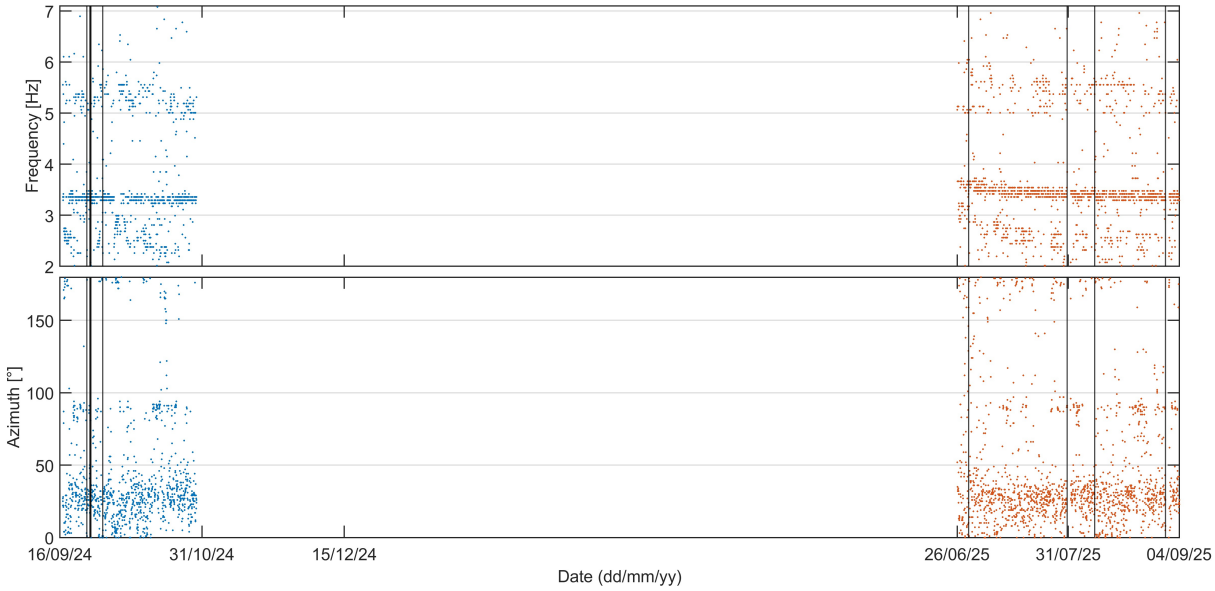

Figure 3.19: Frequency and azimuth analysis for geophone GEA12. Top panel: time series of the frequency associated to the maximum amplitude of the horizontal components. Bottom panel: corresponding azimuth of the extracted frequency. Blue indicates period 1 and orange indicates period 2. White regions represent data gaps whereas vertical black lines represents data gap within both monitoring periods.

Both GEA06 and GEA07 were recording when, on the 8$^{\text{th}}$ November 2024, a human intervention took place at the monitoring site and both of them were levelled again. This operation led to a shift in the azimuth, and for this reason both datasets were corrected.

For GEA06, since the recorded azimuth was almost constant throughout period 1, the correction was performed by shifting upward the data after the 8th November by the difference between the mean azimuth before and after that day, resulting in a 30° adjustment.

Conversely, GEA07 showed a more complex azimuth pattern within period 1, making it impossible to apply the same correction strategy used for GEA06. In this case, the shift was performed through a trial-and-error procedure until the data immediately before and after the intervention fell within the same azimuth values range.

In Figures 3.16-3.17, azimuth values are shown already corrected.

Looking at Figure 3.16, it can be observed that the azimuth of the dominant modes of vibration is almost constant, in the range 100-125 Hz, but the dominant modes of vibration seem to be two: a superior one in the range 5-5.5 Hz that weakens once the cold months approach, and a lower one that is weaker during warm months and in the range of 2-3 Hz but increases up to 3.5 Hz and becomes stronger during cold months. Unfortunately, the recorded period is too short to confirm this behaviour; indeed, the station does not work properly at all in period 2.

Similarly, GEA07 also recorded two dominant modes of vibration. The upper one (5-5.7 Hz) seems more stable, while the lower one (2.5-3.5 Hz) varies more, as for GEA06. Indeed, the lower one seems to increase from mid-November and then decrease again in June. Unfortunately, the long winter gap does not allow for a more comprehensive understanding of the behaviour of the dominant frequencies of GEA07.

Overall, as far as the first period is concerned, GEA06 and GEA07 recorded a similar pattern of dominant vibration mode frequencies. However, looking at the azimuth, GEA07 shows different behaviour compared to GEA06. Indeed, while GEA06 azimuth stays almost constant within period 1, when approaching the cold temperatures (mid-November, aligned with the change in frequency), GEA07 azimuth starts to decrease, passing from an average of 120° to 100°, and in period 2 the azimuth is almost constant at about 100°.

An azimuth of 120° means that the eastern rock column (block 4 in Figure 3.8) vibrates almost perpendicularly to the main fracture (monitored by extensometer 21), while at 100° it vibrates more parallel to the back fracture (between the rock columns and the stable compartment). This changing behaviour might be related to the observed closure of the main fracture in cold months.

Looking at periods 1 and 2 together, it seems that when the higher frequency is dominant the azimuth is about 120°, while the lower frequency that is strong in the cold months but also in the warm months of period 2 seems to be linked to an azimuth of 100°.

A comprehensive understanding would require not only data in the gap between the two recorded periods, but also multi-year recordings in order to better understand the possible link between the dominant frequencies and relative azimuth with temperature and other ongoing processes at the site. Indeed, looking only at the first period of GEA07, it seemed that the pattern of the dominant mode of vibration was related to temperature, but then having also the second period, the expected azimuth (following the theory of decreasing azimuth with decreasing temperature derived from looking at the first period) would have been higher in the second period.

From GEA11 (Figure 3.18), the recorded period was very short, but a single dominant vibration mode at 5 Hz emerges, with weak vibration in the range 0-10°. Since it is on the Raibl formation, no different behaviour was expected.

Finally, GEA12 (Figure 3.19) showed a single dominant mode of vibration at around

3.5 Hz with weak vibration mainly at 25°. Also for this geophone, no changes in these two analysed parameters were expected, being on the stable compartment.

3.5.4 PSD and H/V

Method

Spectral analysis of the ambient seismic noise recordings was undertaken to evaluate the performance of the monitoring network, recognize the presence of resonance frequencies in the noise spectral content and study their temporal evolution. Spectral analysis involved the computation of the Power Spectral densities (PSDs) for each component of each station, the single-station spectral ratios (H/V) and the relative Probability Density Functions (PDFs).

Before computing the PSDs, the continuous time series for each station component was subjected to preprocessing (according to McNamara and Buland, 2004). Data clipping was used to reduce the influence of episodic energetic events, using an adaptive threshold fixed at four times the standard deviation of the whole detrended and demeaned signal. To further reduce the variance of the final PSD estimates, each 1-hr time series record was divided into non-overlapping 100-s segments. Furthermore, to suppress side-lobe leakage in the resulting FFT, a 10% cosine taper was applied to the ends of each truncated and detrended time-series segment. Thanks to this operation, the FFT appeared smoothed and the effect of discontinuity between the beginning and end of the time series was minimized. After this preprocessing, PSDs were computed on each 100-s window for each component of each geophone (for the computational method, see Section 2.1.1) and averaged over each 1-hr recording, after correcting for the loss of amplitude due to tapering (*Bendat and Piersol, 1971*).

Moreover, spectral ratio computations were performed to enhance the presence of frequency peaks in the spectral content of the recorded ambient seismic noise. Each 1-hr noise recording was preprocessed following the same steps applied for the PSDs, involving data clipping, segmentation into 100-s windows, and tapering. Then, for each 100-s segment, the Fast Fourier Transform (FFT) was computed and subsequently smoothed with a bandwidth coefficient $b = 90$, following Konno and Ohmachi (1998). This smoothing operation, was applied to suppress spurious closely spaced peaks present in the PSDs, allowing the identification of single physically meaningful resonance frequencies. In this way, spectra along the East, North, and Vertical components were obtained for each 100-s segment. These were finally averaged over 1-hr periods. To compute the ratio between the horizontal and vertical components, the horizontal spectrum was calculated as a squared average (SA):

$$S_H = \sqrt{\frac{S_N^2 + S_E^2}{2}} \tag{3.1}$$

and then divided by the vertical spectrum S_V, yielding the single-station spectral ratios S_H/S_V.

Probability density functions (PDFs) were computed for both PSD and spectral ratio to evaluate the full range of noise at the different seismic stations.

Each 1-hr PSD estimate $PSD(f)$, for each recording channel (E,N,V), was first converted to decibels by applying

$$10 \log_{10}\big(S(f)\big). \tag{3.2}$$

PSD values were then binned into a two-dimensional histogram on a regular frequency–power grid. In particular, the frequency bins used had a width of 0.1 Hz, from 0.2 Hz to the Nyquist frequency (125 Hz), while the power bins had a width of 1 dB, from -300 to 0. For each 1-hr PSD, the count corresponding to the pair of frequency and power bins was incremented when the PSD fell within that bin pair. The PDF at each frequency bin is then obtained by normalizing the histogram column-wise by the total number of occurrences of that frequency. The resulting matrix is displayed as the colored squares in the PDF panels of figures 3.20-3.23. From the same hourly PSDs also the mean value (plotted as a continuous blue line), the 10^{th} and 90^{th} percentiles were computed (shown as dashed red lines). Probability of occurrence of a given power was also compared to the New Low Noise Model (NLNM) and New High Noise Model (NHNM) proposed by Peterson in 1993 (*Peterson, 1993*). These models represent global reference curves for the natural seismic noise levels observed on Earth and are usually used to evaluate the quality of the seismic data.

Analogously to the PSDs, probability density functions (PDFs) were also computed for the H/V spectral ratios in order to describe the full variability of the resonance behaviour at each station. For every 1-hour recording, the H/V spectrum was obtained as described above and subsequently stored to build a two-dimensional histogram in the frequency–H/V amplitude domain. Logarithmically spaced bins were adopted in both dimensions. For each H/V spectrum, the corresponding frequency–amplitude bin was incremented, and the histogram was finally normalized column-wise by the total number of occurrences at each frequency. This representation highlights the most persistent resonance values as regions of high probability in the log–log PDF panels. From the same hourly H/V spectra, the mean curve as well as the 10^{th} and 90^{th} percentiles were computed.

Results

Noise hourly averaged PSDs of the E, N and V channels of all geophones are shown in Figures 3.20-3.23, respectively (PDFs of the whole data set in panels a, b, c and related periodograms in d, e, f).

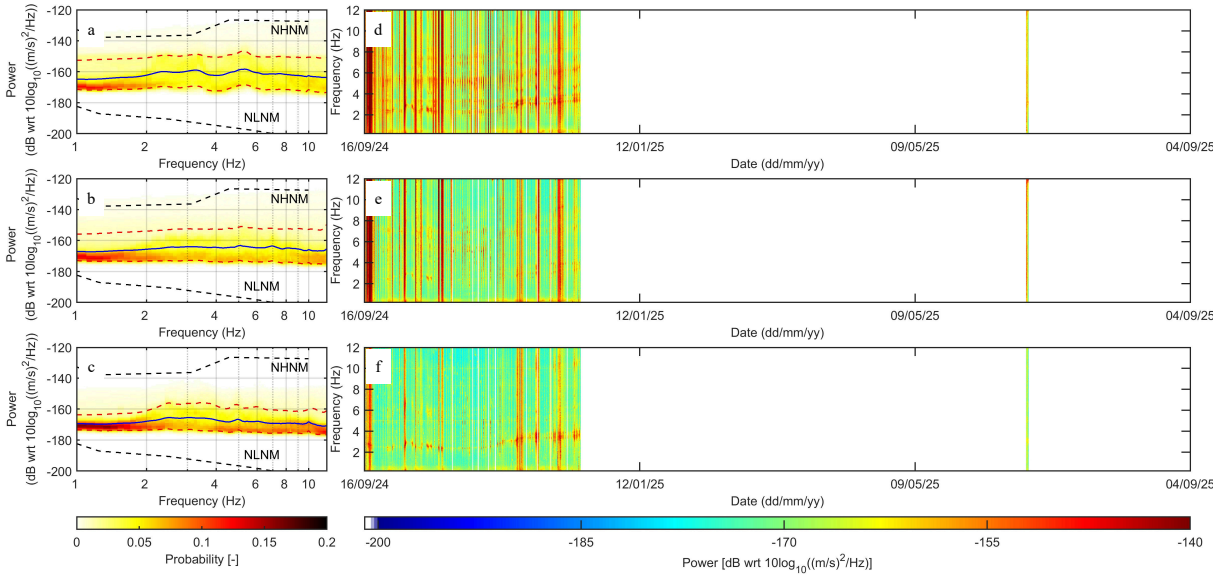

Figure 3.20: Spectral analysis of ambient seismic noise recorded at GEA06 (base of the northern rock column). (a)-(c) Probability density function of the hourly averaged power spectral density, with average (blue line) and 10th–90th percentiles (red dashed lines) of the data set: (a) east, (b) north and (c) vertical components. Black dashed lines: boundaries of the NHNM and NLNM of Peterson (*Peterson, 1993*). (d)–(f) Hourly averaged power spectral densities over the whole monitored period: (d) east, (e) north and (f) vertical components.

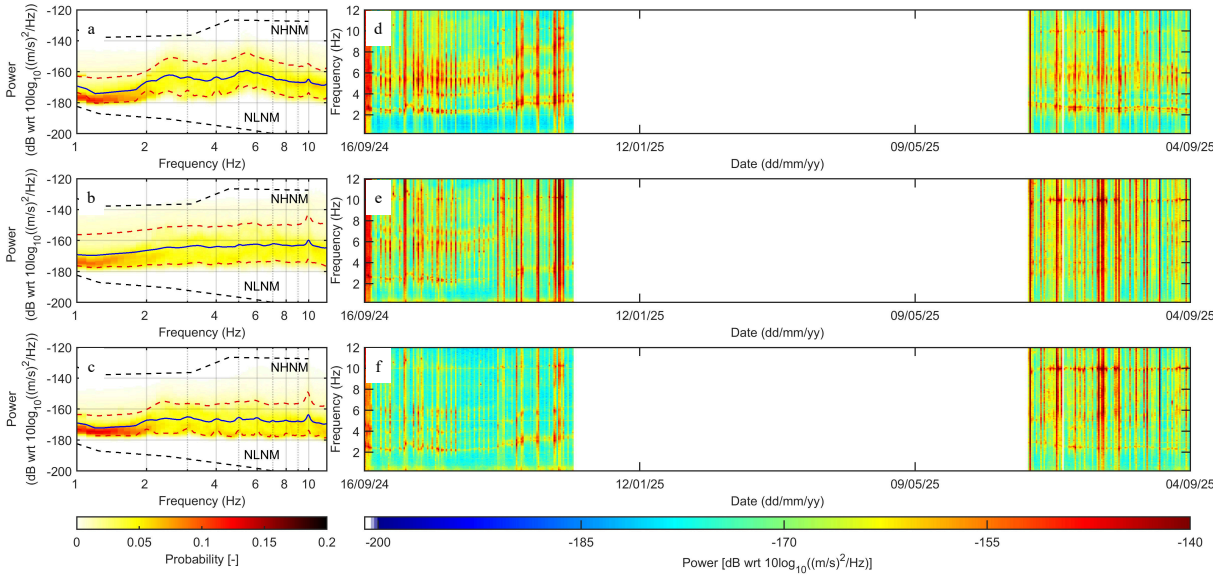

Figure 3.21: Spectral analysis of ambient seismic noise recorded at GEA07 (base of the eastern rock column). (a)-(c) Probability density function of the hourly averaged power spectral density, with average (blue line) and 10th–90th percentiles (red dashed lines) of the data set: (a) east, (b) north and (c) vertical components. Black dashed lines: boundaries of the NHNM and NLNM of Peterson (*Peterson, 1993*). (d)–(f) Hourly averaged power spectral densities over the whole monitored period: (d) east, (e) north and (f) vertical components.

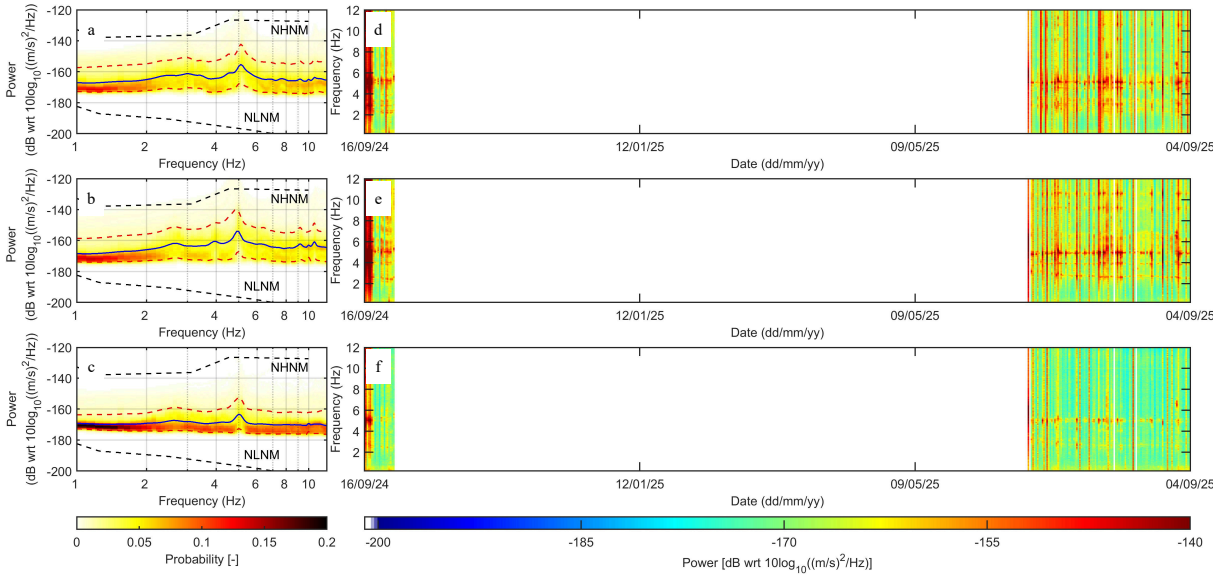

Figure 3.22: Spectral analysis of ambient seismic noise recorded at GEA11 (over the Raibl Formation). (a)-(c) Probability density function of the hourly averaged power spectral density, with average (blue line) and 10th–90th percentiles (red dashed lines) of the data set: (a) east, (b) north and (c) vertical components. Black dashed lines: boundaries of the NHNM and NLNM of Peterson (*Peterson, 1993*). (d)–(f) Hourly averaged power spectral densities over the whole monitored period: (d) east, (e) north and (f) vertical components.

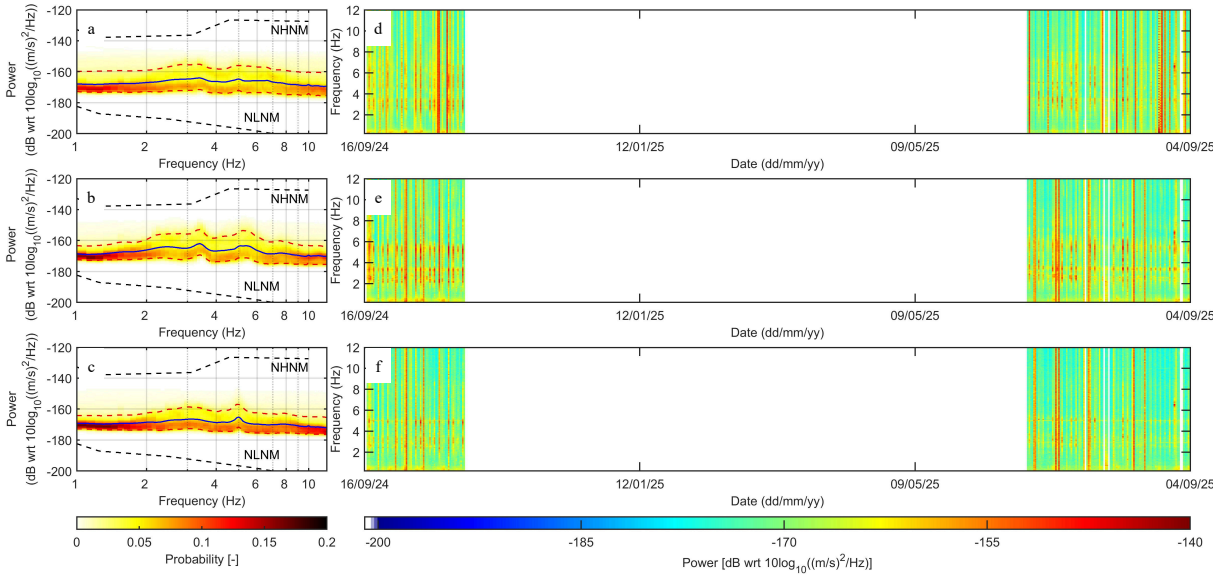

Figure 3.23: Spectral analysis of ambient seismic noise recorded at GEA12 (reference station, over the stable compartment). (a)-(c) Probability density function of the hourly averaged power spectral density, with average (blue line) and 10th–90th percentiles (red dashed lines) of the data set: (a) east, (b) north and (c) vertical components. Black dashed lines: boundaries of the NHNM and NLNM of Peterson (*Peterson, 1993*). (d)–(f) Hourly averaged power spectral densities over the whole monitored period: (d) east, (e) north and (f) vertical components.

From PDFs, it is highlighted that the adopted geophones are almost insensitive below 2 Hz (reddish area). Above this threshold, comparing the recorded data with the new high

and low noise models (NHNM and NLNM), it can be observed a good spectral response and variability on all the components of all four geophones.

GEA06 shows no well-defined spectral peaks and they appear mainly in the east component while they are almost absent along the vertical one. The stronger spectral peaks observed in the east component relative to the north component are consistent with the vibration azimuth of 100–120° obtained in the previous analysis (see Section 3.5.3). Main spectral peaks seem to be at frequencies centered at about 3.3 Hz and 5.2 Hz, but the available data covers just three months, hence not a 1-year complete behaviour can be observed and tracked within spectrograms.

GEA07 shows a main peak at around 5.2 Hz (as GEA06), especially in the east component. Looking at spectrograms of GEA07 (Panels (d)–(f) in Figure 3.21) it seems that the eastern rock column vibrates more than the northern one; indeed, resonance frequencies are clearer and continuous over the monitoring periods.

A possible interpretation of these findings and those reported for the azimuth is that below the rock column monitored by GEA06, conditions remain more stable throughout the year, while below the GEA07 column they seem to change with cold and warm periods. This could be related to the fact that the eastern column is more exposed to direct solar radiation; hence, below the column a thawing and freezing cycle could occur. It could be that below GEA06 this process of thawing is less present or not present at all due to the almost null direct irradiation. However, this theory is just a possible explanation of the observed ambient seismic noise.

Both GEA06 and GEA07 main spectral peaks (2.5–3 Hz and 5–5.5 Hz) show oscillations within the monitoring periods, increasing in frequency around November. Meanwhile, the minor peak present in GEA07 PSD, especially in the vertical component, at around 10 Hz does not exhibit amplitude or frequency variation over time, likely not being related to natural ongoing processes.

For seismic stations GEA11 and GEA12 we expected almost no peaks. However, the proximity to the rock columns leads them to be affected by resonance. Especially for GEA12, which lies on the stable compartment and is almost buried, some noise is shown in the spectrogram (hours at high power at each frequency) that is sometimes related to thunderstorm interference, vibration of the scaffolding, and some other disturbances without an apparent explanation. Overall, PSD results of GEA12 weakly remark the same spectral peaks of GEA06 and GEA07, at around 3 and 5 Hz, with considerably lower spectral amplitudes. Therefore, it can be considered as a reference stable station, even if some influences due to its proximity to the unstable compartments are still present in the data.

Single station spectral ratios for all seismic stations are reported in Figure 3.24.

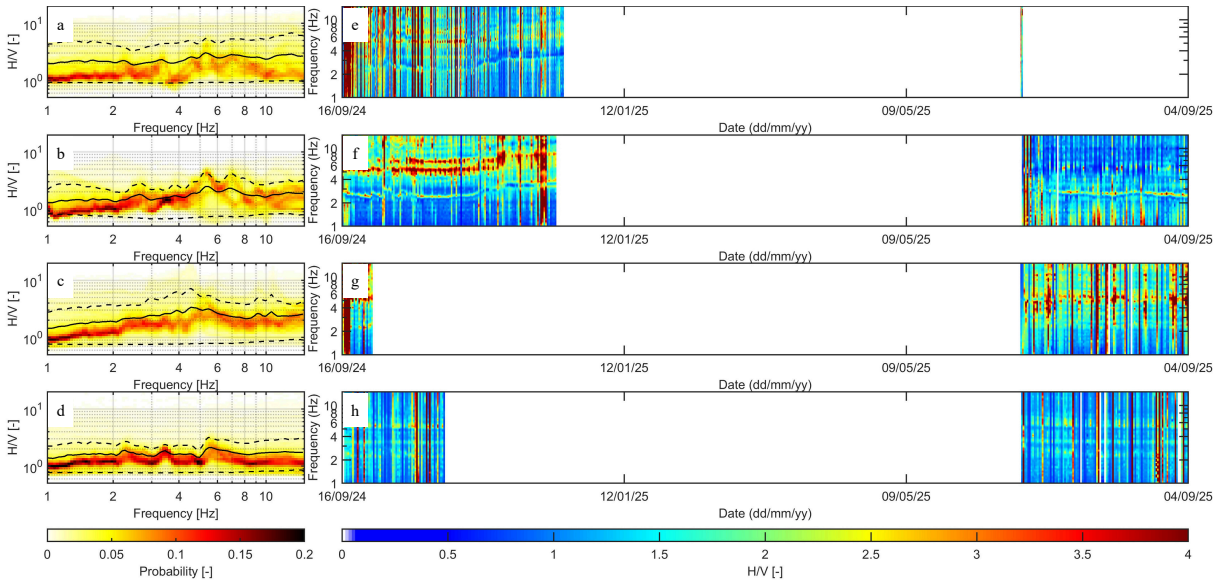

Figure 3.24: Ambient seismic noise single station spectral ratios. (a)–(d) Probability density functions of the hourly averaged spectral ratios, with average (blue line) and 10th–90th percentiles (red dashed lines) of the data set. (e)–(h) Hourly averaged spectral ratios over the whole monitored period. Panels (a) and (e): H/V of GEA06; (b) and (f): H/V of GEA07; (c) and (g): H/V of GEA11; (d) and (h): H/V of GEA12.

Single-station spectral ratios confirm and emphasize the previous spectral observations.

The main focus of the analysis was on the seismic response of GEA07, as it is the geophone with the longest monitoring time frame and is located over an unstable compartment. A zoom just over the temporal evolution of its spectral ratio is reported in Figure 3.25. By looking at its spectral ratios, over period 1, two main spectral frequencies at around 5.5 Hz and 7 Hz can be observed. They seem to increase slightly in frequency at around 20$^{\text{th}}$ November 2024, and simultaneously the lower one weakens. This is temporally aligned with the change in azimuth observed at the same geophone. Moreover, in GEA07 H/V plots not only the frequencies at around 5.5 Hz and 7 Hz are clearly visible, but also the one at around 2.5–3 Hz is visible. Of these three, only the two lower ones are coherent with frequencies extracted within the azimuth data analysis. The azimuth plot has been truncated at 7.1 Hz; however, even plotting up to 10 Hz, the higher frequency was not extracted. This discrepancy could be related to the fact that the frequencies extracted in the azimuth part were the ones associated with the maximum of the horizontal components, while here the frequency is related to all the horizontal and vertical components. Still looking at GEA07, it can be observed that in period 2 some low-frequency disturbances around 1 Hz appear, leading to contamination of the PDF. Furthermore, still in period 2, the frequency pattern is different compared to period 1. Indeed, the highest frequencies (5.5 and 7 Hz) are very strong in period 1 and barely visible in period 2. Moreover, the 5.5 Hz peak seems to have disappeared in period 2. In this case study this behaviour could be related to a question of constraints of the rock column. Based on the constraints of the pillar, the vibration mode seems to change (as also visible from the azimuth), but for now there are too few data to confirm this theory. The observed disappearance of a frequency was also observed in another case study, still unpublished, over Cervino, where during cold months only one frequency appears, but during melting

three frequencies appear. In that case, by modelling it resulted that this behaviour is related to the presence of ice in the main fracture during winter, while the presence of air in the same fracture leads to the presence of more than one frequency in the computed spectral ratios. In the present case of the Sas da Lech, it does not seem to be a matter of ice presence in the main fracture, but of structural constraints of the rock column. To confirm this hypothesis, modelling should be pursued.

GEA11 and GEA12, which are over the Raibl Formation and on the stable compartment respectively, were expected to have a constant value of 1 in the PDF plots (Panels (a)–(d) of Figure 3.24). However, as already observed with PSDs, they are affected by the vicinity of the unstable rock columns. GEA12, compared to GEA11, is located on stable rock but is also buried. This makes it less sensitive to wind-induced vibrations, and hence its H/V plot appears less noisy.

By looking at the zoomed view of the GEA07 spectral ratio (Figure 3.25), it can be highlighted that around mid-November the resonance frequencies increase. This increase is temporally aligned with the decrease in temperature and indicates that the observed system appears to become more rigid, which could be related to the formation of ice within or below the eastern rock column. During warm periods (see the H/V at the beginning of period 2), when the system is likely less rigid, the resonance frequencies decrease and become weaker.

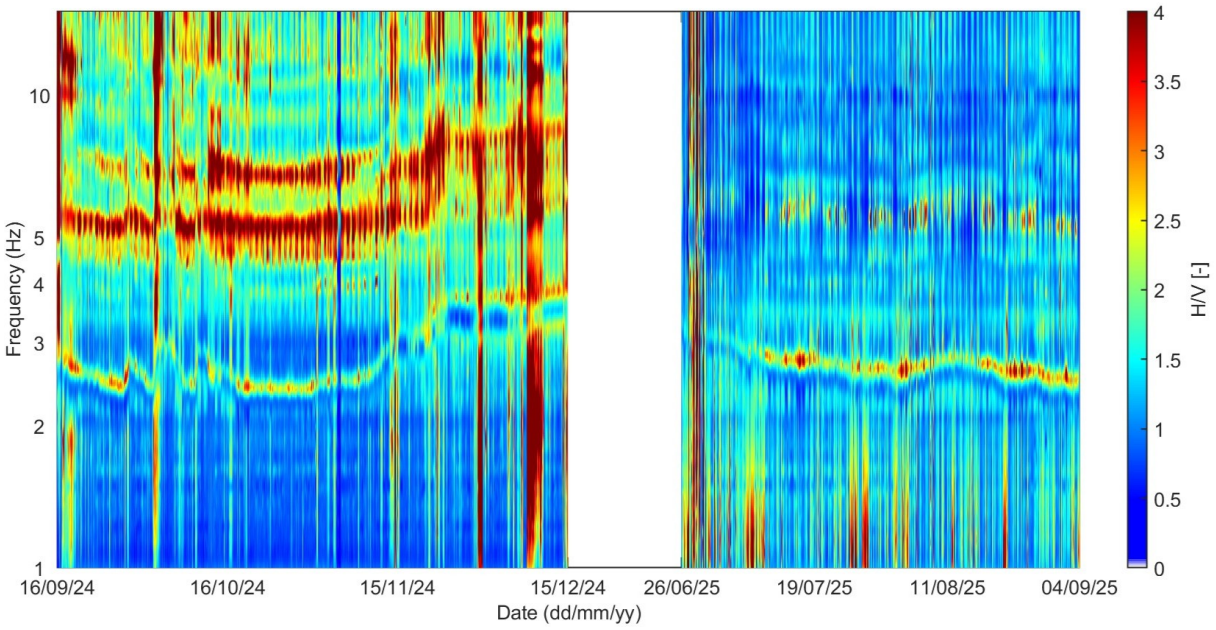

Figure 3.25: Hourly-averaged spectral ratios of GEA07 over the entire monitored period. The temporal gap between the two monitoring periods has been intentionally reduced in the figure to improve the visibility of the data within each period.

Since the obtained Power Spectral Densities and spectral ratios turned out to be very noisy, and also to further investigate the possible causes of the oscillation observed in the resonance frequencies, they were both compared to meteorological variables collected at the meteorological station "Badia Cima Pisciadù" and to the air temperature data available on the site. A focus on GEA06 and GEA07 is presented in the following, being the stations monitoring unstable compartments.

Comparing period 1 of both stations (Figures 3.26-3.27), it is clearly visible how the spectral ratios of GEA06 are much more noisy, making it more difficult to pick the resonance frequencies. However, resonance frequencies of both geophones seem to have the same pattern: dominant frequencies of 5.5 Hz and 7 Hz, and a weaker one at 3 Hz. The two highest ones also seem to somehow unify at the end of the period, or one of the two disappears, it is not that clear. In any case, they weaken. Unfortunately, period 2 for GEA06 was not available to perform a comparison between the two stations, and the data gap between the two monitoring periods does not allow a more comprehensive understanding of the behaviour of the spectral ratios.

Looking at period 1 of the GEA06 spectral ratio (Figure 3.26), it can be observed that the weakening in the most clear resonance frequency (5.5 Hz) is likely related to the decrease in temperature below 0°C in mid-November.

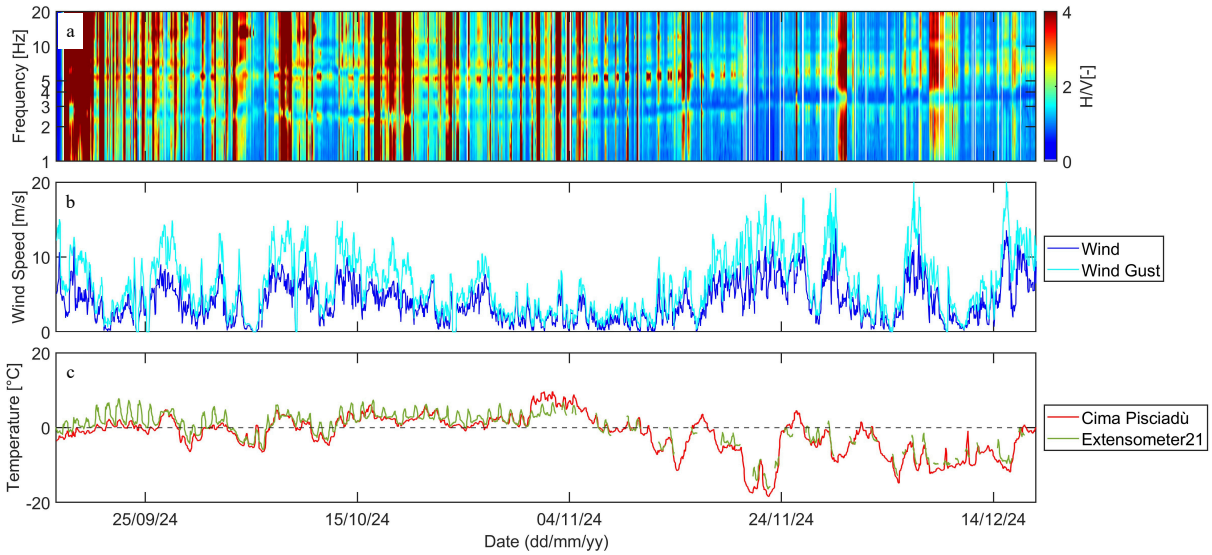

Figure 3.26: GEA06 hourly averaged ambient seismic noise single-station spectral ratios compared with meteorological variables for period 1. (a) Temporal evolution of the spectral ratios; white bands across all frequencies indicate data gaps. (b) Wind speed and wind gust time series from the "Badia Cima Pisciadù" meteorological station. (c) Air temperature from the "Badia Cima Pisciadù" meteorological station and from extensometer 21 at the monitoring site.

Now, a focus on GEA07 is proposed. Even if the spectral ratios of Figure 3.27 and Figure 3.28 refer to the same geophone and were extracted in the same way from the raw ambient seismic noise, they are very different. In period 2, in the range 5–7 Hz, just one resonance frequency appears and is much weaker than in period 1, while the 3 Hz frequency is stronger and seems to decrease a bit within that monitoring period.

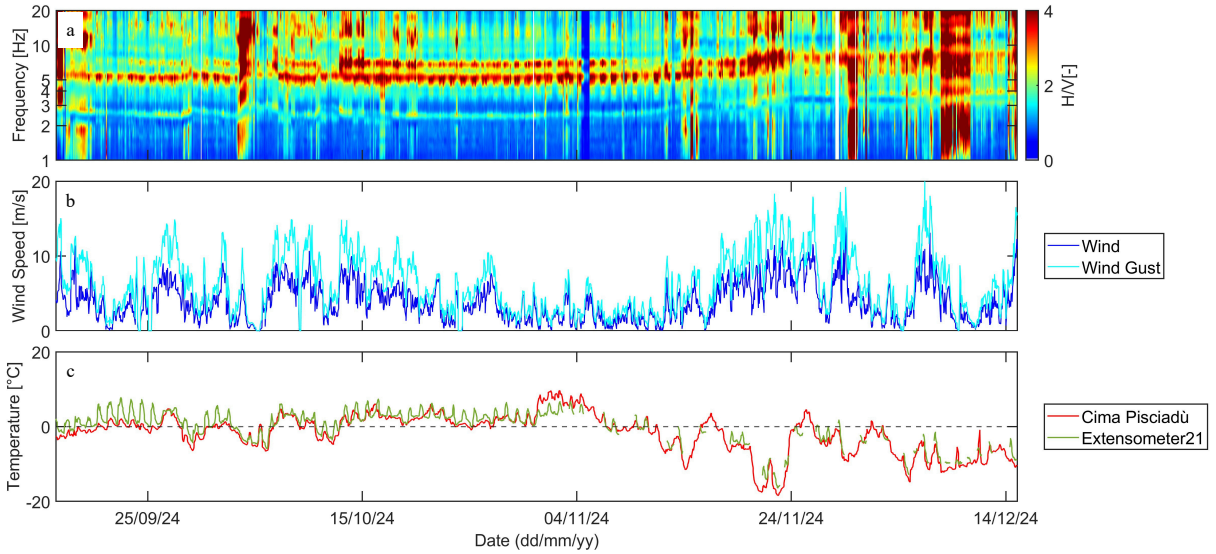

Figure 3.27: GEA07 hourly averaged ambient seismic noise single-station spectral ratios compared with meteorological variables for period 1. (a) Temporal evolution of the spectral ratios; white bands across all frequencies indicate data gaps. (b) Wind speed and wind gust time series from the "Badia Cima Pisciadù" meteorological station. (c) Air temperature from the "Badia Cima Pisciadù" meteorological station and from extensometer 21 at the monitoring site.

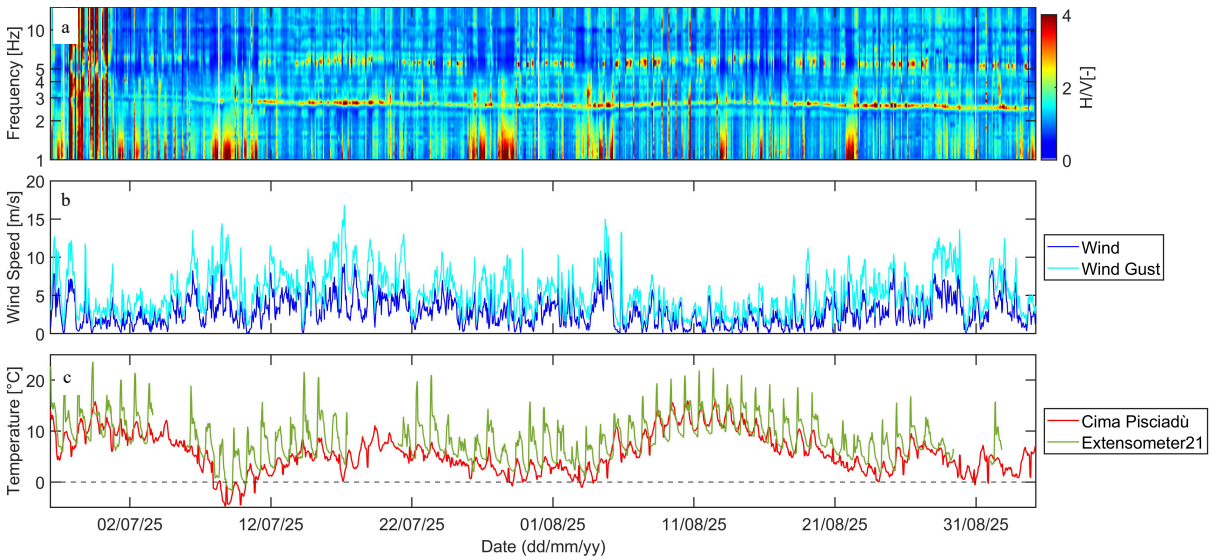

Figure 3.28: GEA07 hourly averaged ambient seismic noise single-station spectral ratios compared with meteorological variables for period 2. (a) Temporal evolution of the spectral ratios; white bands across all frequencies indicate data gaps. (b) Wind speed and wind gust time series from the "Badia Cima Pisciadù" meteorological station. (c) Air temperature from the "Badia Cima Pisciadù" meteorological station and from extensometer 21 at the monitoring site.

In the just presented plots (Figures 3.26-3.28) wind was plotted in order to understand if the vibration of the rock columns and the relative vibrations registered at the geophones were related to the wind blowing. Indeed, the PSDs of GEA12 (Figure 3.23) were much less noisy than those of the other stations, and it was hypothesized that this could be due to the sensor being buried, and thus not exposed to the air. From the spectral ratios, it

also emerged that not all of the observed noise can be explained by the presence of wind. However, we are sure that it is a variable that has some influence on the H/V, since at the beginning of period 1, two days of surveys were performed on the site and, while leaving the site, it was very windy. At the beginning of both Figure 3.26 and Figure 3.27, a set of hours with very high spectral ratios at each frequency can be noticed.

Hence, a further comparison was performed between wind and the GEA07 PSDs to understand the wind role in the recorded noise. In particular, the East and North components were filtered to highligth just the hours of recording when wind was above its mean value (3.99 m/s and 2.96 m/s for period 1 and period 2, respectively).

In both periods, the PSD of the north component appeared noisier (as already observable in Figure 3.21). Indeed, noisy hours are more reddish along the north component than along the east one. From the filtering (Figures 3.29–3.30), it was found that the wind appears to play a role in generating this noise. Many noisy hours were extracted in both period 1 and period 2. In particular, at the beginning of both periods, we are certain that the site conditions were highly windy due to the human presence during the surveys.

However, wind conditions exceeding the mean are not the only cause of noise in the spectrograms, nor are they always a triggering factor. Indeed, the filtering also extracted hours that were not noisy. This outcome may be related to several factors, such as the orography, which does not always allow the wind to reach the geophones on Piz Pisciadù with the same intensity and direction, the threshold used for the filtering, or other processes generating noise that are not yet understood.

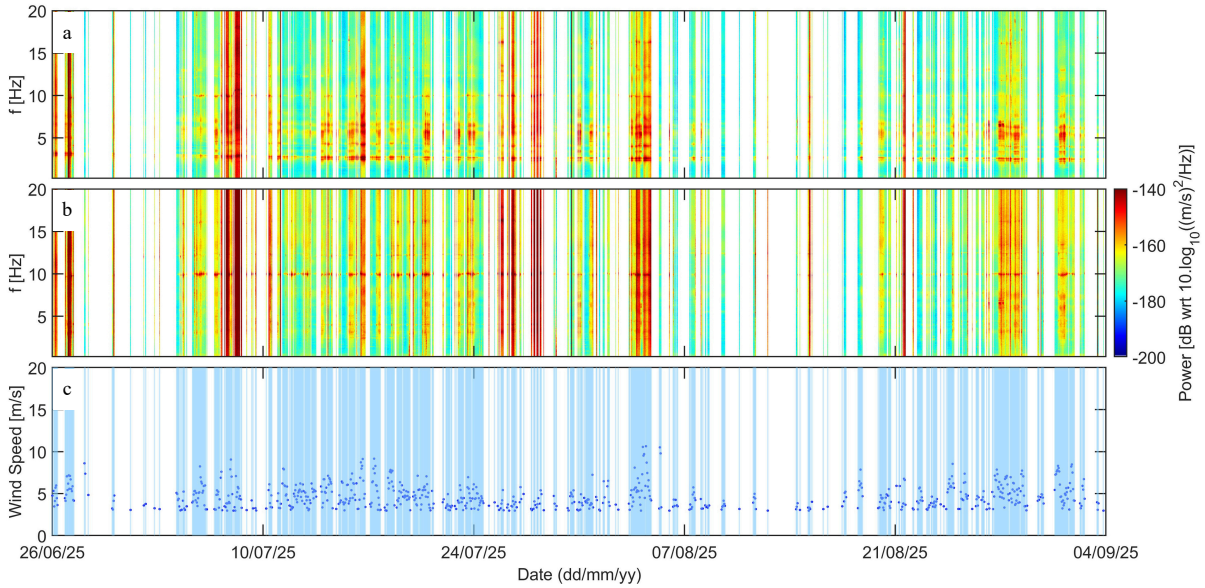

Figure 3.29: Horizontal GEA07 PSDs comparison with wind speed measured at the meteorological station "Badia Cima Pisciadù" within period 1. Data shown are the hours in which the wind speed exceeds the threshold of 3.99 m/s, corresponding to the mean value over period 1. (a) East component PSD. (b) North component PSD. (c) Wind speed.

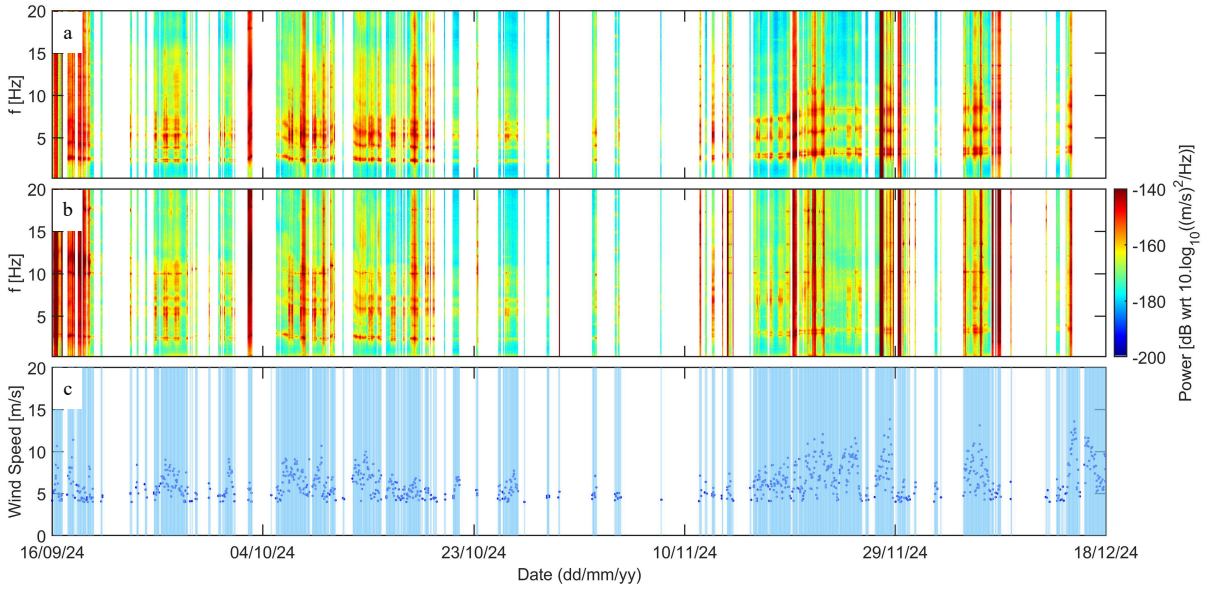

Figure 3.30: Horizontal GEA07 PSDs comparison with wind speed measured at the meteorological station "Badia Cima Pisciadù" within period 2. Data shown are the hours in which the wind speed exceeds the threshold of 2.96 m/s, corresponding to the mean value over period 2. (a) East component PSD. (b) North component PSD. (c) Wind speed.

Finally, a more detailed comparison was performed to assess the influence of temperature. Indeed, in both spectral ratios and PSDs of all stations, a clear cyclicity can be observed, following the daily thermal cycle. Here, only the case of GEA07 during period 2 is presented (Figures 3.31-3.32), but similar patterns were observed for all stations in both periods.

In Figures 3.31–3.32, PSDs were filtered to show only daytime and nighttime periods, respectively. The threshold used to define day and night hours was determined by examining the temperature time series (Panel d in both figures). From these series, a rapid increase in air temperature starting around 07:00 can be observed, reaching the daily maximum within a few hours, followed by a subsequent decrease. Very noisy hours are observed both during the day and at night, across all components and hence are not likely related to temperature. The main temperature control is reflected in the background noise, which is generally lower at night, resulting in more greenish colors in the PSD plots. Additionally, resonance frequencies tend to weaken during nighttime.

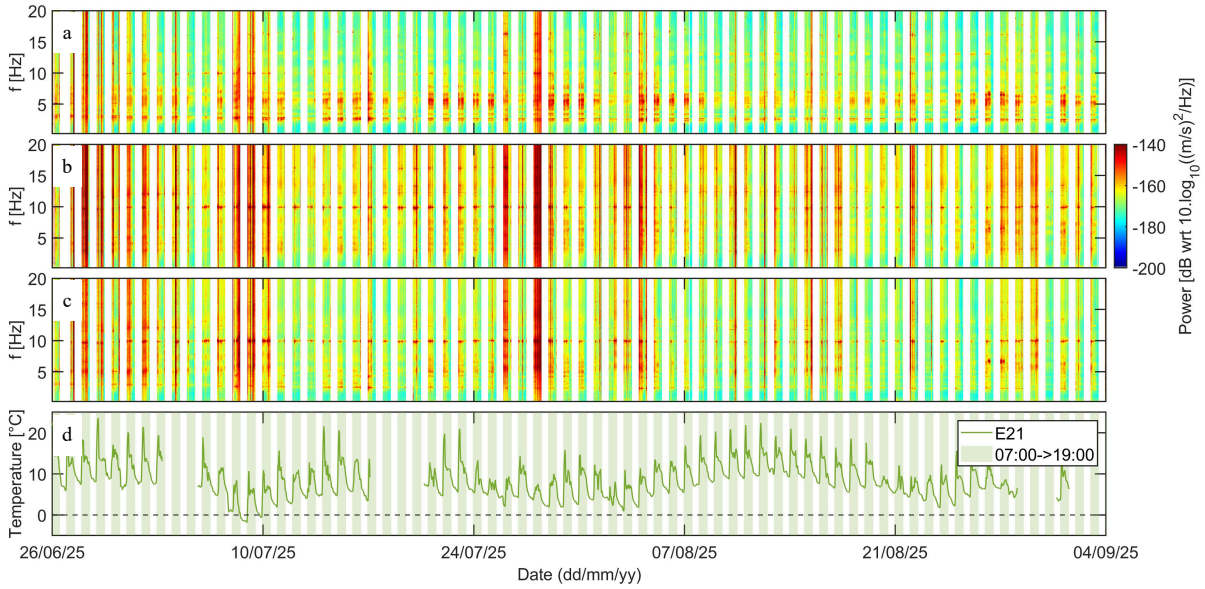

Figure 3.31: Comparison of GEA07 PSDs with air temperature measured at Extensometer 21 during period 2, focusing on daytime hours. (a)-(c) East, North, and Vertical component PSDs shown only for daytime hours (07:00–19:00). (d) Air temperature at Extensometer 21. Daytime periods are highlighted with vertical shaded bands (07:00–19:00).

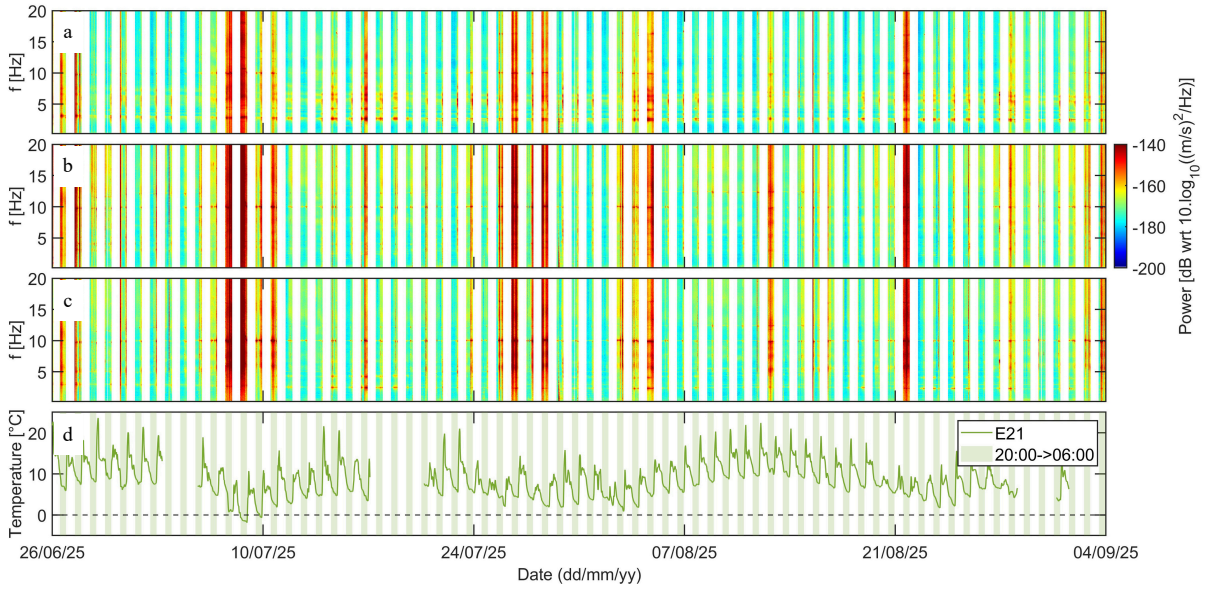

Figure 3.32: Comparison of GEA07 PSDs with air temperature measured at Extensometer 21 during period 2, focusing on nighttime hours. (a)-(c) East, North, and Vertical component PSDs shown only for nighttime hours (20:00–06:00). (d) Air temperature at Extensometer 21. Nighttime periods are highlighted with vertical shaded bands (20:00–06:00).

3.5.5 Microseismicity

Method

Microseismic events detection was performed using a Short Time Average over Long Time Average (STA/LTA) algorithm. This method is based on the ratio between the average

amplitude of the recorded ambient seismic noise over a short-time window (STA) and a long-time window (LTA). The parameters used are:

- 0.5 s short-time window
- 10 s long-time window
- STA/LTA = 6 trigger-on threshold
- STA/LTA = 3 trigger-off threshold
- 0.5 s minimum event duration.

A 3 s pre-event window was automatically added to avoid missing first arrivals on some channels, and a 10 s post-event window ensured that the full waveform was captured. A representation of the algorithm's operation is shown in Figure 3.33.

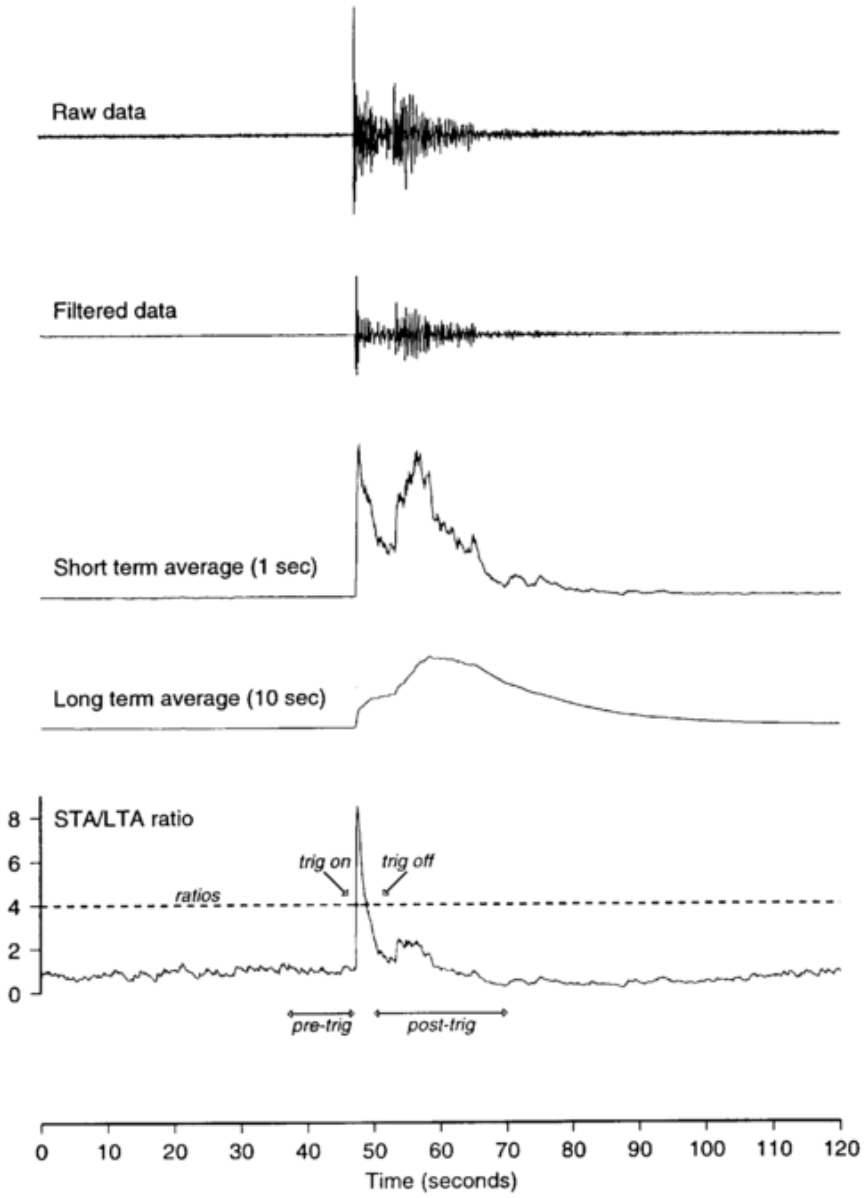

Figure 3.33: Illustration of the STA/LTA algorithm (*Ltd., 2019*).

The detection was performed just over GEA06 and GEA07 continuous ambient seismic noise recording.

Within period 1 a total of 9329 events were extracted for GEA06 and 9529 events for GEA07, while a total of 10654 events were extracted for GEA07 in period 2.

A first filtering was performed to remove the hours of known presence of operators on the site (Table 3.4).

Table 3.4: Filtering criteria used to remove events recorded while operators were on site, and corresponding number of events removed.

	Removed date	**Number of removed events**	
		GEA06	**GEA07**
Period 1 (16/09/2024–18/12/2024)	16/09/2024 11:00→14:00 UTC 17/09/2024 08:00→12:00 UTC 08/11/2024 06:00→11:00 UTC	101	289
Period 2 (26/06/2025–04/09/2025)	26/06/2025 09:00→17:00 UTC 27/06/2025 06:00→12:00 UTC	–	187

A further filtering was performed according to salient time- and frequency-domain parameters of the events. In particular, for each event were calculated:

- Kurtosis, the fourth moment in statistics. It is a measure of the shape of a data distribution, providing information about the heaviness of the tails and the peakedness of the distribution relative to a normal distribution. High kurtosis indicates heavy tails, while low kurtosis indicates light tails.
- Total extracted signal duration.
- Maximum energy band. It saves the index of the **5** Hz-wide frequency band (indexed sequentially: $1 = 1 - 5$ Hz, $2 = 5 - 10$ Hz, etc.) where the maximum energy is concentrated (i.e., the largest area under the amplitude spectrum). This measure is preferred over peak frequency to identify true energy content, avoiding noise peaks (e.g., 50 Hz due to electromagnetic interferences).
- Peak frequency (f_{peak}): the frequency corresponding to the maximum amplitude in the signal's amplitude spectrum.
- Maximum amplitude (A_{max}) of the signal, expressed in m/s.

All events with kurtosis greater than 500, total duration shorter than 13 s (extracted at the end of the 1-hour stored signal and therefore not comparable with the other events), and maximum amplitude greater than 0.04 m/s for GEA06 and 0.02 m/s for GEA07 were filtered out, as they were likely not natural events and considered outliers.

Considering the unusual behavior of the GEA06 event frequency peak, and the fact that only three months of events were extracted, the analysis of microseismicity was primarily focused on GEA07 events.

For each event, the extracted signal along the north component was plotted in the time domain, in the frequency domain, and the corresponding spectrogram was computed,

obtaining figures useful for visual classification of the events. An example is shown in Figure 3.41.

The frequency-domain plot was obtained by using the Fast Fourier Transform (FFT) algorithm. Let L be the length of the signal and $FS = 250$ Hz be the sampling frequency. The full-range amplitude spectrum, $Y(f)$, was calculated by taking the magnitude of the FFT and normalizing by the signal length, L:

$$Y(f) = \frac{|\mathrm{FFT}(s(t))|}{L}.$$

To obtain the single-sided amplitude spectrum (or true amplitude spectrum), $Y_{\mathrm{true}}(f)$, the result was doubled and truncated to positive frequencies. The doubling of the amplitude is done to account for the energy discarded from the negative frequency components (since the signal $s(t)$ is real-valued). The frequency axis, f, was created by selecting the positive frequency components from 0 Hz up to $f_{Nyquist} = FS/2 = 125$ Hz.

The spectrogram was obtained by dividing the signal into overlapping segments of length $N_F = L/20$. Consecutive segments overlapped by $N_F/1.01$ samples. For each segment, the Fast Fourier Transform (FFT) was computed, and the magnitude was normalized by the segment length and doubled to obtain the single-sided amplitude:

$$Y_{\mathrm{segment}}(f,t) = \frac{2\,|\mathrm{FFT}(s_{\mathrm{segment}}(t))|}{N_F}.$$

Finally, the spectrogram in decibels was calculated as

$$Y_{\mathrm{dB}}(f,t) = 20\log_{10}\left(Y_{\mathrm{segment}}(f,t)\right),$$

where f is the frequency vector from 0 up to the Nyquist frequency $f_{\mathrm{Nyquist}} = FS/2 = 125$ Hz, and t is the time corresponding to the center of each segment. The resulting spectrogram provides a time-frequency representation of the signal, allowing visual inspection of how spectral content evolves over time.

After all those filtering operation, the temporal trend of the remaining events was computed and analyzed in comparison with the meteorological parameters.

Results

Extracted events were first plotted in cumulative form to provide an immediate visualization of their temporal trend. Figure 3.34 shows the cumulative GEA06 events, already filtered according to human presence on the site and the previously described parameters. From the total number of extracted events, 283 were filtered out, of which 101 occurred during hours when operators were present.

Within period 1, 11 steep steps were identified. The detection procedure was performed by interpolating the discrete event data onto a fine, uniform 5-minute time grid. The instantaneous rate of events (the slope of the cumulative count) was then calculated, followed by a 2-hour moving average smoothing to mitigate noise and highlight long-term rate changes. The steepest event periods were identified by applying a percentile threshold of 95%, isolating only the steepest 5% of event periods. Finally, a temporal filter was applied, retaining only those identified steep intervals that persisted for a minimum of 3 hours. This ensures that the detected "steps" represent sustained increases in the event rate rather than short-lived bursts. It can be observed that most of the steps occurred

in November and December. Indeed, the GEA06 trend of the cumulative events changed before and after mid-November, increasing from an average of 2.7 events per hour to 6 events per hour. This mean is strongly influenced by the occurrence of the steep steps.

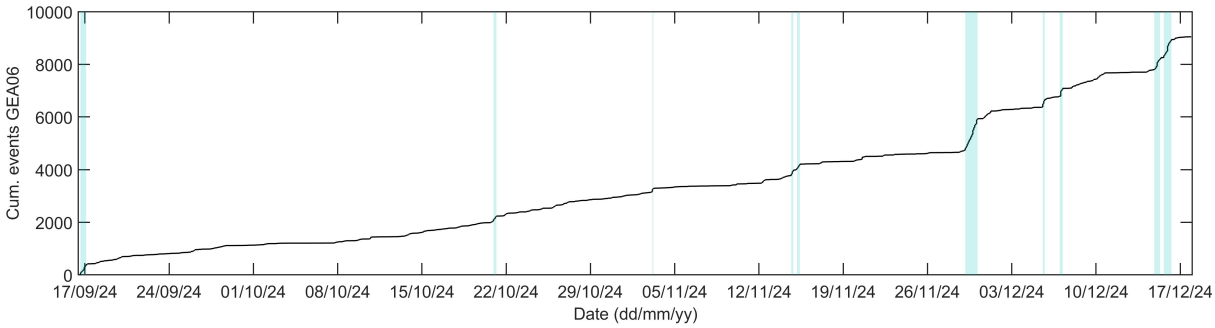

Figure 3.34: Cumulative GEA06 events during period 1. Blue vertical bars highlight the main steep steps in the curve.

The occurrence of events during different hours of the day was also investigated, as shown in Figure 3.35. A strong variability in the timing of events within a day is evident for period 1, with most events occurring during night hours.

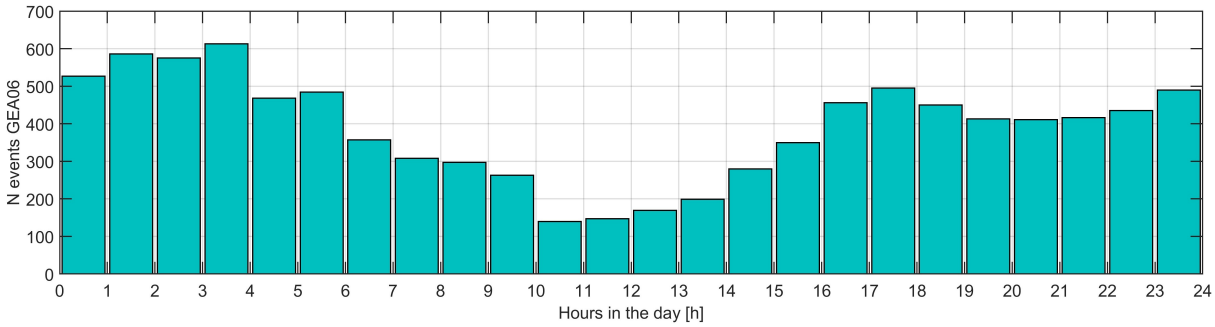

Figure 3.35: Distribution of microseismic events extracted from GEA06 ambient seismic noise using STA/LTA across different hours of the day.

It is important to note that the analyzed period covers only about three months. Therefore, the observed variability in the daily occurrence of microseismic events cannot be assumed to represent the entire year.

The events of most interest in the present case study are those of micro-cracking and microfracturing happening within the rock mass. These events produce impulsive and short duration signals, with a sharp energy increase in the spectrogram followed by an exponential decay of the high frequency content with time. The duration of a single event is generally short (< 1.5 s), but they can occur in sequences of repeating and overlapping events, making the total event duration an ineffective parameter for classification. All those characteristics are coherent with micro-fracturing signatures reported in the literature (*Colombero et al., 2018*;*Colombero et al., 2021*). An example of spectrogram is reported in Figure 3.36. Those events, despite being of great interest, are not easy to be filtered from the all extracted events; indeed, they exhibit variable maximum amplitude and they can occur once or in series with different time spacing. Also the frequency peak is not the same for all of them. All of these considerations make microseismicity analysis challenging.

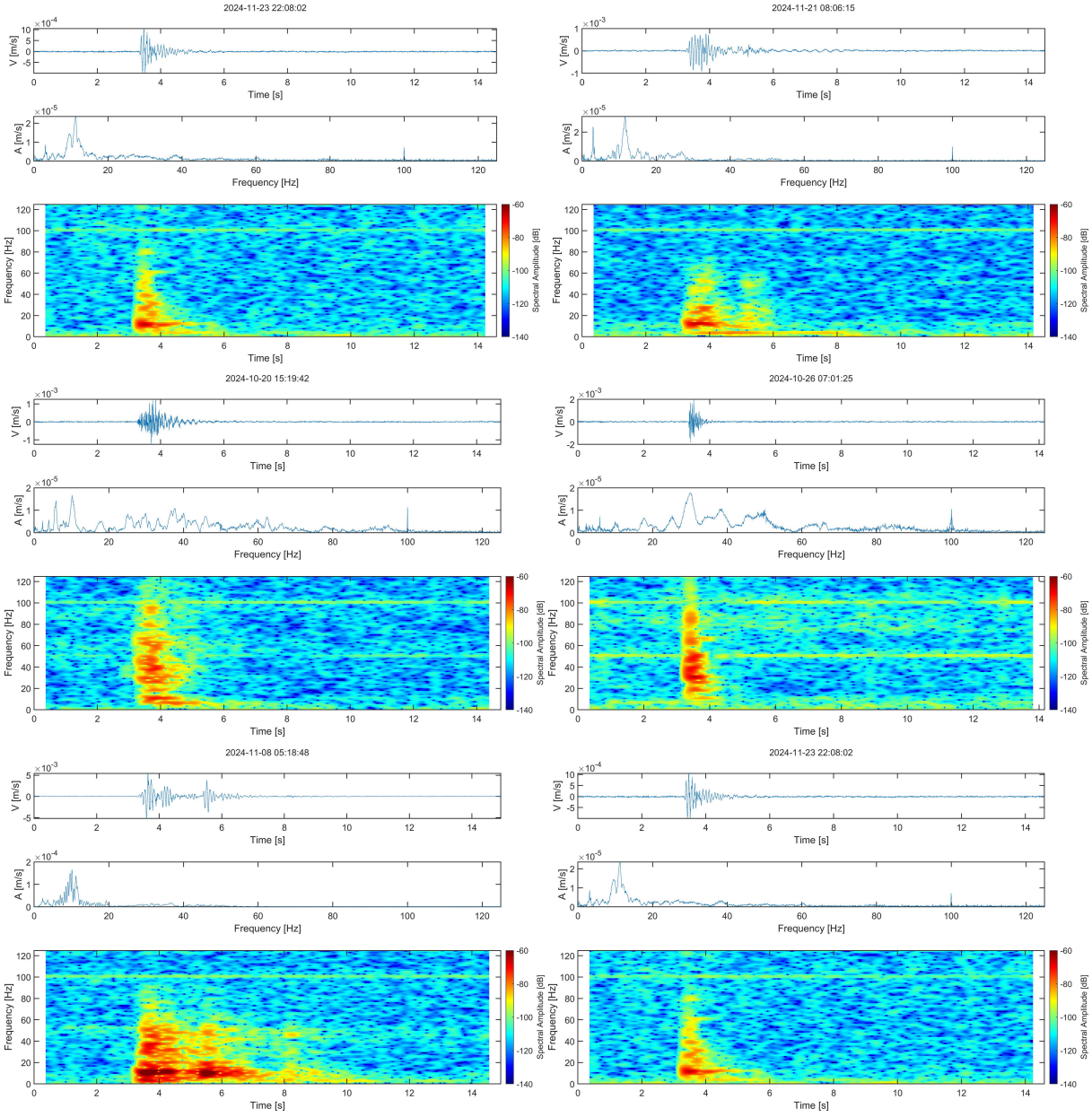

Figure 3.36: Examples of microseismic events recorded at GEA07. In each plot, from the top to the bottom: seismogram, related Fourier spectrum and spectrogram. Events like these are likely micro-fracturing events.

However, from the visual analysis it appeared that most of these events (likely related to fracturing processes) have peak frequency lower than 20 Hz.

From the visual analysis of the spectrograms, other kinds of events were recognized, such as helicopter flights near the rock columns. Their spectrograms appear with particular features like those in Figure 3.37. Out of the total number of extracted events, helicopter flights were 3 for GEA06, 9 for GEA07 in period 1 (of which 7 on the 8$^{\text{th}}$ of November 2024, when operators went to the site to re-level the geophones) and 5 for GEA07 in period 2. Hence, they represent only a very small number of events, with variable amplitude and peak frequency, but they are well recognizable from the spectrograms.

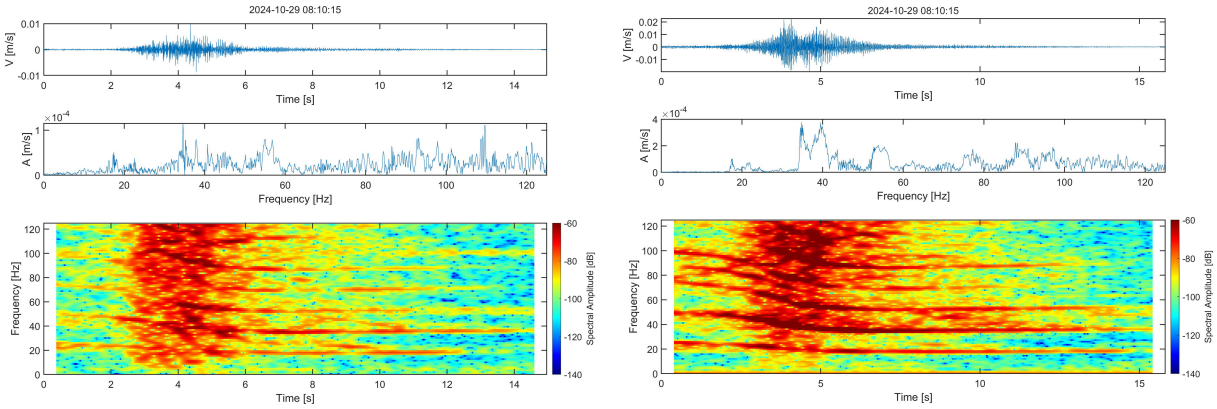

Figure 3.37: Examples of the same microseismic event extracted at GEA06 (left) and at GEA07 (right). In each plot, from the top to the bottom: seismogram, related Fourier spectrum and spectrogram. Events like these are likely related to helicopter flights nearby the rock columns.

Another kind of events extracted are regional and local earthquakes. Those events are characterized by long duration and low-frequency content (usually < 20 Hz), with a sharp onset in the energy content in the spectrogram (Figure 3.38). Within period 1, from GEA06 ambient seismic noise, 15 events were extracted and 18 from GEA07. The dates of occurrence of those events were compared with regional earthquakes registered in the European-Mediterranean Seismological Centre catalogue (*EMSC-CSEM, n.d.*) and were confirmed. While just 5 were extracted in period 2. In both periods a few other events were extracted showing a very similar spectrogram with respect to the ones of the events confirmed by catalogues. They could be related to more local earthquakes, and possibly linked to the synsedimentary fault which crosses the Sas da Lech (see Section 3.2).

It is worth highlighting the fact that most of these earthquake events were extracted by both stations, while others by just one of the two. Moreover, the analysis of these events highlights a limitation of the STA/LTA algorithm. Indeed, as shown in Figure 3.38 in panels c–d, the same event was extracted only by GEA07. Actually, GEA06 was working, but the background noise was too high for the STA/LTA to detect the earthquake. Indeed, STA/LTA was used to extract events by surpassing the background noise. It is important to keep in mind that when the noise is strong, some events may still be recorded but not extracted. However, earthquakes are an insignificant number of events compared to the total number of events extracted and more importantly are spread all over the periods and not concentrate, thus not contributing to rapid increases in the number of events occurring on the site.

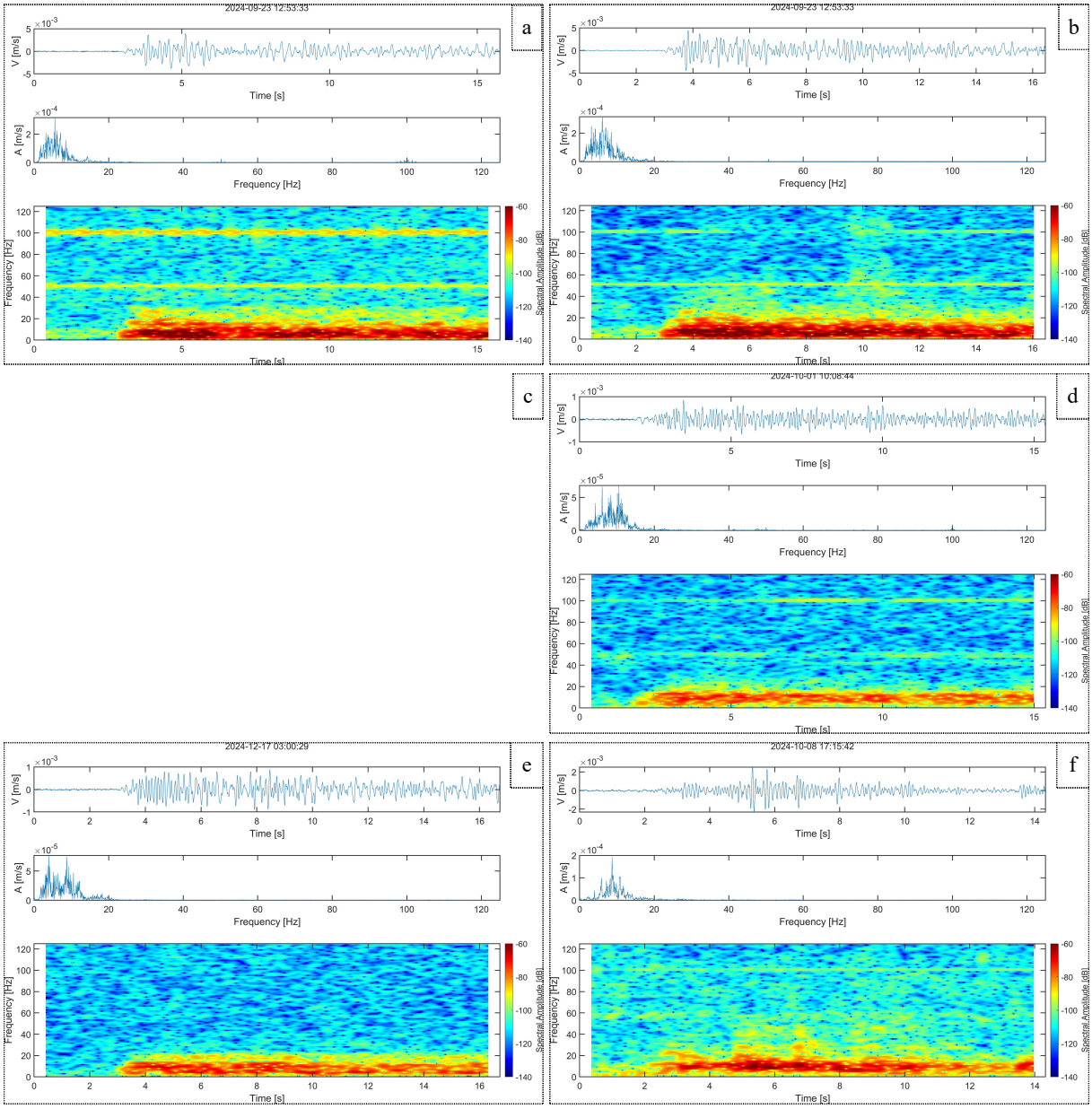

Figure 3.38: Examples of microseismic events extracted at GEA06 (a-c-e) and at GEA07 (b-d-f). In each plot, from the top to the bottom: seismogram, related Fourier spectrum and spectrogram. Events like these are likely related to local and regional earthquakes. (a-b) Same earthquake extracted by both station on 23/09/2024 12:53:33, registered in catalogue with code EqId:1710484. (c-d) earthquake event extracted just by GEA07. (e-f) Local earthquake not registered in catalogues but recorded and extracted by geophones on the site.

Despite some of the presented events being easy to recognize (even if not always easy to filter out from the total extracted events), there were also other events with an unexplained spectrogram. An example is shown in Figure 3.39. These latter events all occurred during period 2 and were interpreted as very high-frequency events, of which only the lower coda appears in the spectrogram, but it was difficult to associate them with a known ongoing process.

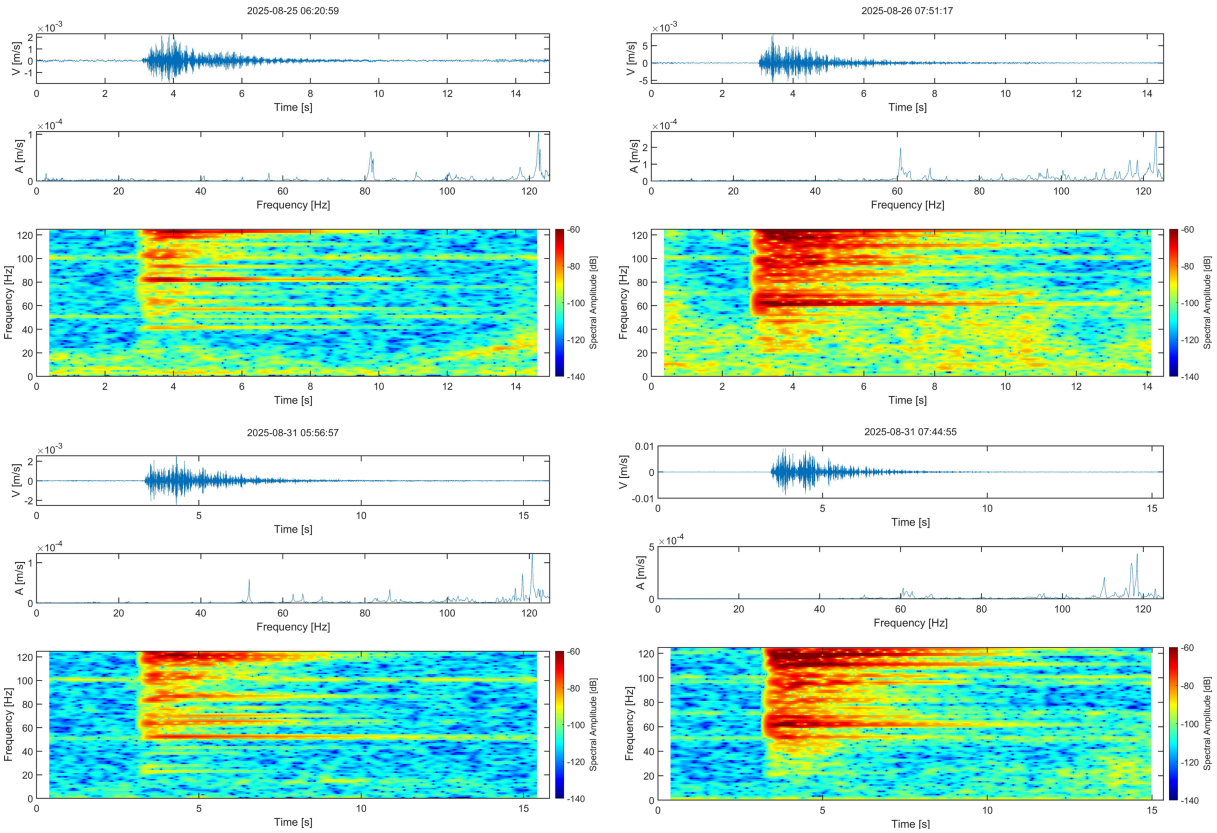

Figure 3.39: Examples of microseismic events extracted at GEA07 within period 2 that were not easy to be related to some ongoing process.

This preliminary visual analyses of spectrogram allowed to identify some characteristic feature of events but due to the too high amount of events extracted it was very time consuming to perform a classification of the events. Hence, according to the feature observed by spectrograms and by the parameters extracted for all the events, the further considerations were performed. Firstly, the analysis focused on GEA07 events. This decision was made since there were more events to be analyzed, especially coming from two different periods of the year, which would make the results obtained more robust, even if still requiring confirmation from future data collection, particularly in the months with gaps. Moreover, the peak frequency of GEA06 showed some coherent events below 20 Hz and some other events, but less clearly coherent, between 65 and 85 Hz (Figure 3.40). Indeed, especially when cold approached in mid-November, the behaviour of the peak frequencies became not fully understandable. Moreover, a prominent peak at 50 Hz is observed in the event spectrum, likely resulting from electromagnetic interference generated by on-site instrumentation such as solar panel inverters, extensometers, or geophones (An example is reported in Figure 3.41).

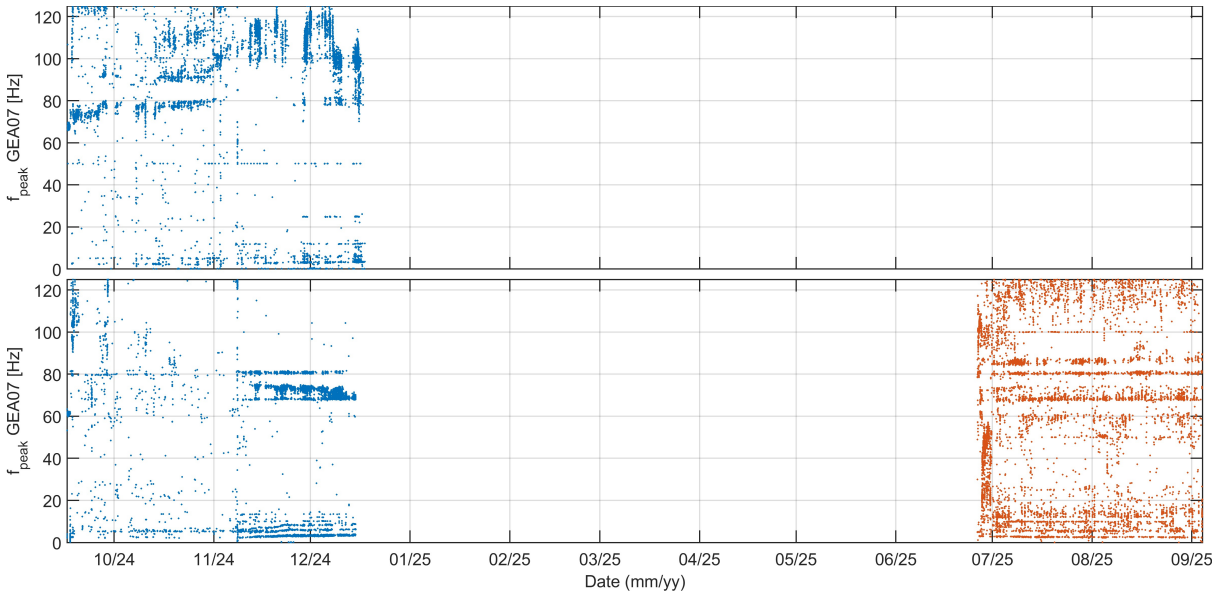

Figure 3.40: Peak frequencies of microseismic events extracted from GEA06 and GEA07. Blue markers correspond to events from period 1 (16/09/2024–18/12/2024), while orange markers correspond to events from period 2 (26/06/2025–04/09/2025).

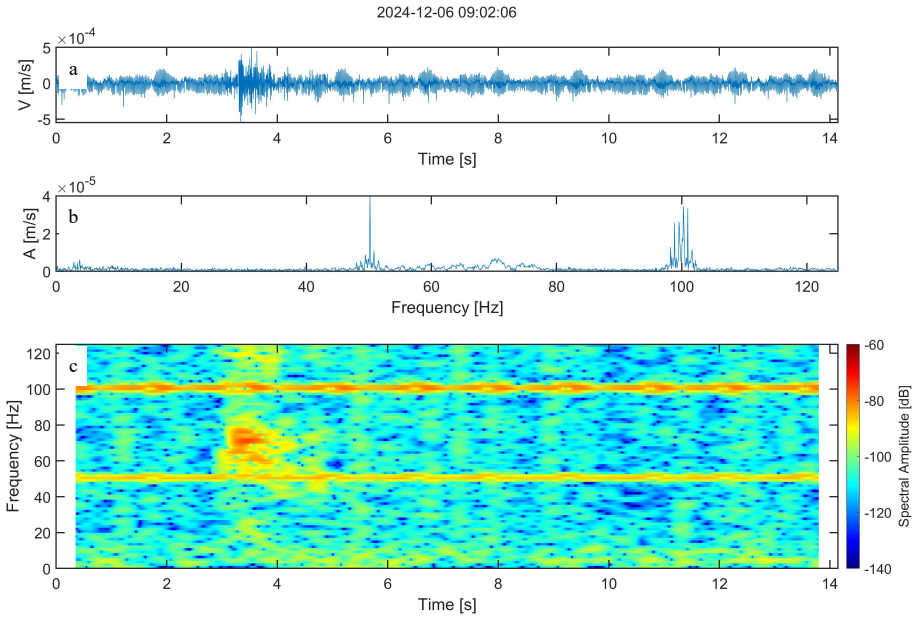

Figure 3.41: Example of electromagnetic interference recorded in the ambient seismic noise of geophones, with frequency peaks observed at 50 and 100 Hz. (a) Seismogram recorded on channel N. (b) Corresponding Fourier spectrum. (c) Corresponding spectrogram.

By observing GEA07 peak frequency, in both periods, two clusters of coherent events were identified. For this reason, the further analysis was applied to the filtered GEA07 events in the following peak frequency ranges:

- 2–11 Hz
- 65–85 Hz

A representation of the events extracted by this criterion is shown in Figure 3.42.

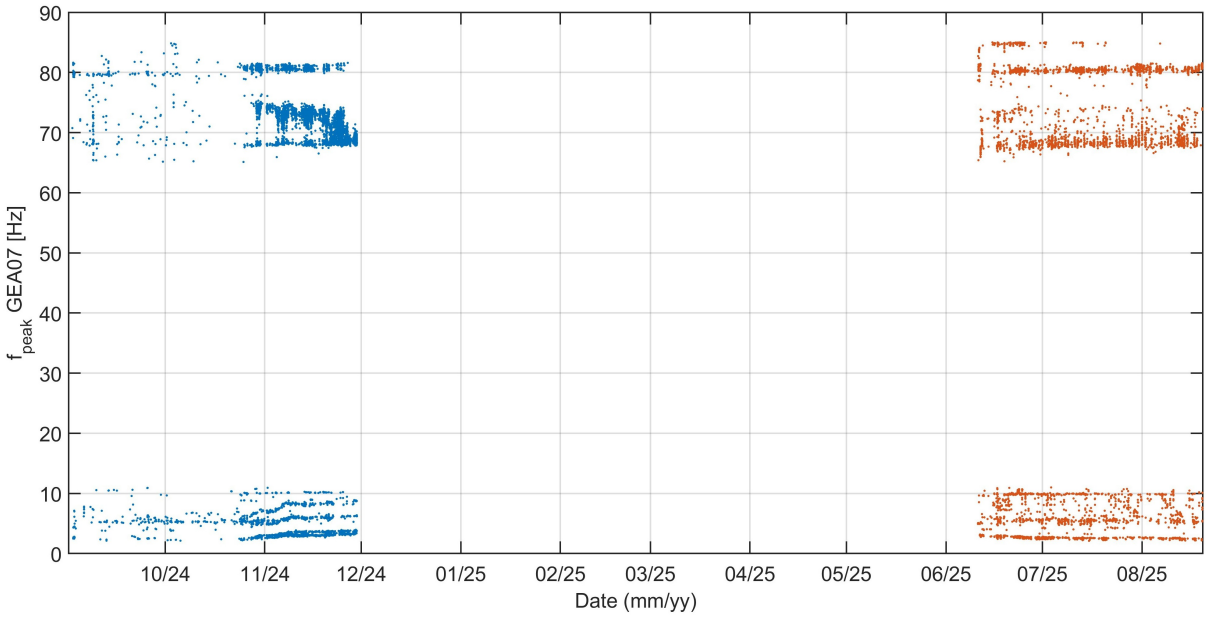

Figure 3.42: Peak frequencies of extracted and filtered GEA07 microseismic events. Filtering removed events occurring during human presence on the site, events with kurtosis > 500, total duration < 13 s, maximum amplitude > 0.02 m/s, and events with peak frequencies outside the ranges 2-11 Hz and 65-85 Hz. Blue markers correspond to events from period 1, while orange markers correspond to events from period 2.

The performed filtering operations removed 1183 events out of the total 5529 events extracted in period 1, and 5672 events out of the 10654 extracted in period 2. Especially for period 2, more than 50% of the events were filtered out, many of which had very high peak frequencies (greater than 100 Hz).

The peak frequency of the MS events proved to be a characteristic parameter of the extracted signals, as it closely matched the frequency of maximum energy (Figure 3.43). This indicates that the extracted peak frequency did not exhibit significant deviations or isolated spikes relative to the main energetic portion of the events.

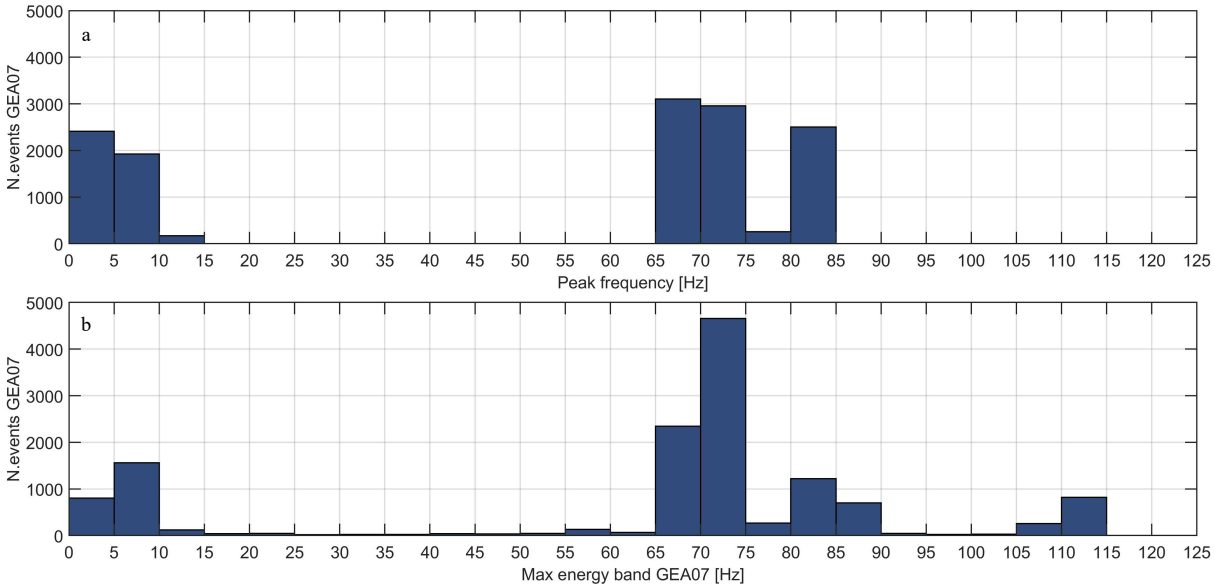

Figure 3.43: Comparison between peak frequency and maximum energy band of GEA07 in periods 1 and 2. (a) Histogram of peak frequencies of the extracted and filtered events, using 5 Hz bins. (b) 5 Hz bins associated with the maximum energy, computed as the frequency interval with the largest area under the amplitude spectrum.

The GEA07 extracted and filtered events were plotted, in cumulative form to provide an immediate visualization of their temporal trend (as previously done for GEA06). The two monitoring periods were plotted separately (Figures 3.44-3.45) and for both of them the main rapid increment in the number of events were evaluated as for GEA06.

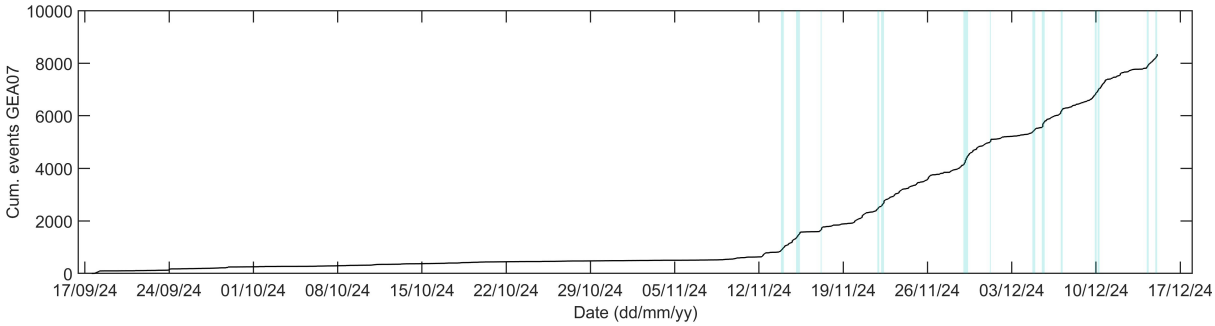

Figure 3.44: Cumulative GEA07 events during period 1. Blue vertical bars highlight the main steep steps in the curve.

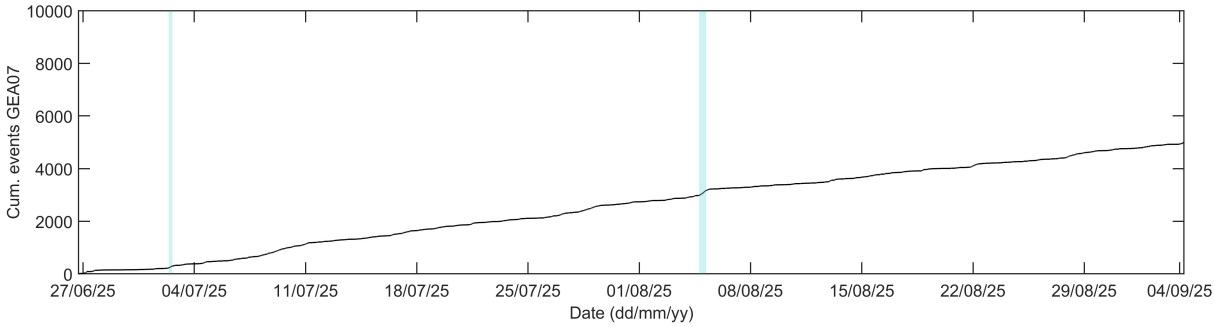

Figure 3.45: Cumulative GEA07 events during period 2. Blue vertical bars highlight the main steep steps in the curve.

Period 1 and period 2 showed very different trends. Actually, three different trends can be observed. The first one covers the first two months of recording during autumn 2024, up to the 9th of November 2024, with a mean number of events per hour of 0.4. Within this first time period, no rapid increase in the event rate was observed. The second trend was observed from the 9th of November 2024 onward, with 14 different rapid increases in the number of events. Despite this pattern, very different from that of GEA06, the total number of events extracted from the two stations within period 1 was very similar. The filtering of GEA07 did not affect its general trend in period 1.

Hence, the observed patterns suggest that the eastern rock column experiences a marked increase in microseismic activity during the cold months. This behavior can be explained by differences in the timing of freezing between the two columns. The northern column monitored by GEA06, being less exposed to sunlight, likely experiences early freezing of its shallow layers, generating microseismic events already from September, with a gradual increase in November as deeper layers freeze. In contrast, the eastern column monitored by GEA07, more exposed to sunlight, undergoes delayed freezing. Only around mid-November, when both the superficial and deeper layers of the underlying Raibl rock freeze, does the microseismicity increase sharply, resulting in the concentration of events observed between November and December 2024.

In period 2, the observed trend is quite an intermediate trend compared to the two just described, with a mean of 3 events/h and just two rapid increases.

In order to investigate the nature of the rapid increases in the event rate, and why the trend changed so much from the 9th of November, the microseismic events occurrence was compared to meteorological parameters. In particular, it was compared with air temperature measured at the site by extensometer 21, superficial rock temperature measured by the outer sensors of the multiparametric columns, wind speed and wind gust speed measured at the meteorological station of "Badia Cima Pisciadù", and precipitation data from the two valley stations "Corvara" and "Selva di Val Gardena" (Figures 3.46-3.47).

Precipitation data have been reported as the mean precipitation (in mm) measured on hours when both meteorological stations recorded rainfall. Since the two stations are located respectively to the east-north-east and west-north-west of the monitoring site, it was assumed that when it was raining at both stations, it was also raining in between them, and therefore at Sas da Lech. This is indeed a strong assumption, but the two stations are almost equally distant from the site and are the closest ones providing precipitation measurements. For this reason, precipitation was not taken into account in the analysis until now. It has only been considered here to visualise whether some of the

main highlighted steps in the event rate could be related to heavy precipitation events. It resulted that there is no linear trend in event occurrence with increasing rain intensity or frequency. This is valid for both periods, although more precise precipitation data at the site could lead to different results.

Temperature and wind have been of greater interest, and both seem to have some influence on the occurrence of microseismic events.

In particular, rock temperature appears to have had a strong influence on the microseismic events. Indeed, the number of extracted events increased substantially once rock temperature fell below 0 °C, starting from 9th November 2024. When considering only air temperature, its brief drop below 0 °C for a few days in October did not lead to an increase in the number of events. Hence, the thermal inertia of the rock played a role: a few days of sub-zero air temperature were not sufficient to freeze the rock, and therefore did not lead to an increase in microseismic activity; however, once rock temperature reached 0 °C in mid-November, the number of events increased significantly. This may indicate that most of the recorded and extracted events are related to freezing processes.

High wind intensity, and especially high wind gust speed, also seems to have contributed to an increase in the number of recorded events, although no direct relationship has been observed. Indeed, the highest wind speeds occurred during the cold months, but similarly high wind intensities were recorded in autumn without causing steep increases in the number of events. However, it is important to note that wind was measured at the top of Piz Pisciadù, at about 265 m higher elevation. At the monitoring site, the lower elevation and especially the local orography could have resulted in different wind speeds and, in particular, different gust intensity.

During period 2, both air and rock temperatures were almost always above 0 °C, and this is likely the reason why the occurrence of microseismic events remained almost constant throughout the period. Wind appears again to play a role: indeed, one of the two observed steep increases in event rate corresponds to very high wind values. However, even higher wind intensities were recorded on 17th July 2025. Once again, precipitation does not appear to have a direct relationship with the occurrence of microseismic events.

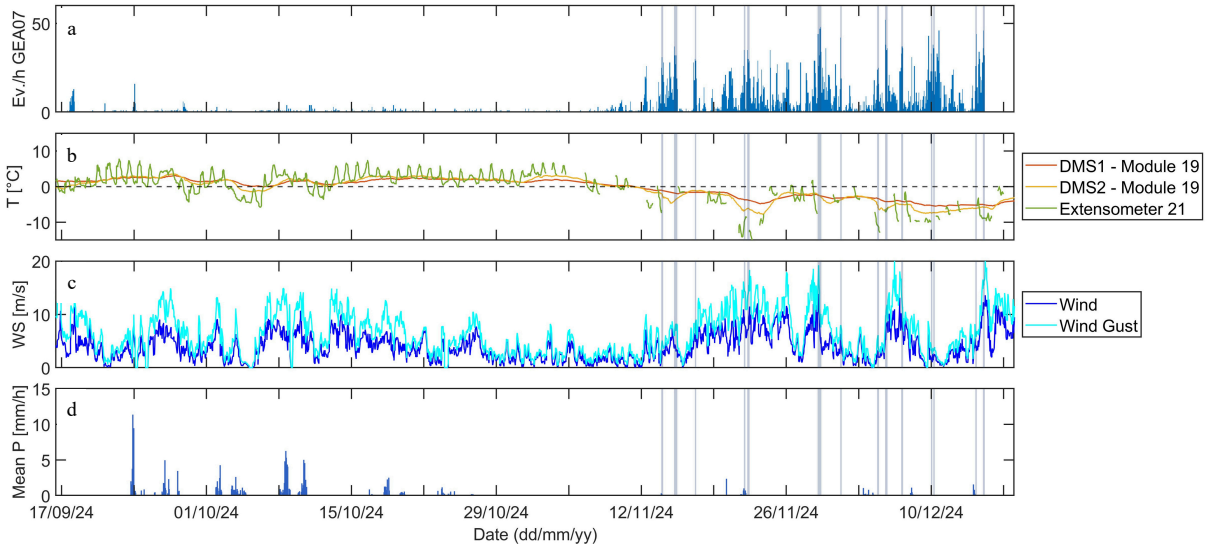

Figure 3.46: Microseismic events at GEA07 during period 1 compared with meteorological parameters. Grey vertical bars indicate the main steep increases in the event rate. (a) Event rate at GEA07, expressed as the number of microseismic events per hour. (b) Air temperature measured at extensometer 21 and rock temperature at module 19 of DMS1 and DMS2. (c) Wind speed and wind gust speed recorded at the meteorological station "Badia Cima Pisciadù". (d) Precipitation, reported as the mean value measured at the two valley stations "Corvara" and "Selva di Val Gardena" on hours when rainfall was recorded at both stations.

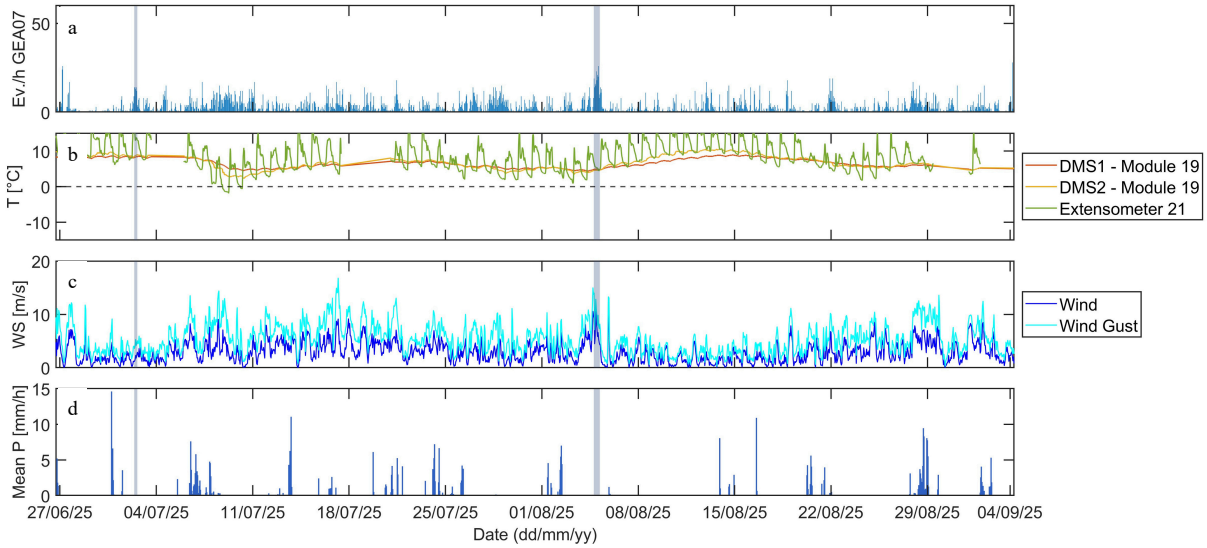

Figure 3.47: Microseismic events at GEA07 during period 2 compared with meteorological parameters. Grey vertical bars indicate the main steep increases in the event rate. (a) Event rate at GEA07, expressed as the number of microseismic events per hour. (b) Air temperature measured at extensometer 21 and rock temperature at module 19 of DMS1 and DMS2. (c) Wind speed and wind gust speed recorded at the meteorological station "Badia Cima Pisciadù". (d) Precipitation, reported as the mean value measured at the two valley stations "Corvara" and "Selva di Val Gardena" on hours when rainfall was recorded at both stations.

Since surface rock temperature and wind intensity resulted to be the most influential parameters related to MS event occurrence, they were further investigated. Rock

temperature, as before, was taken as the temperature measured at the outer modules of multiparametric columns DMS1 and DMS2. The half-hour raw temperature data were averaged over a 1-hr resolution and averaged between the two sensors to get a single rock temperature value for each hour. The two monitoring periods were considered, and for each 1 °C temperature bin, the mean number of events occurring at that temperature was computed, along with the number of hours in which that temperature bin range occurred (Figure 3.48). It resulted that, as already observed, most of the events occurred when rock temperatures were below 0 °C. However, the shortness of the recording period led to having not so many hours of recording during cold times. However, a link seems to be present between the below-0 °C superficial rock temperature and the occurrence of events.

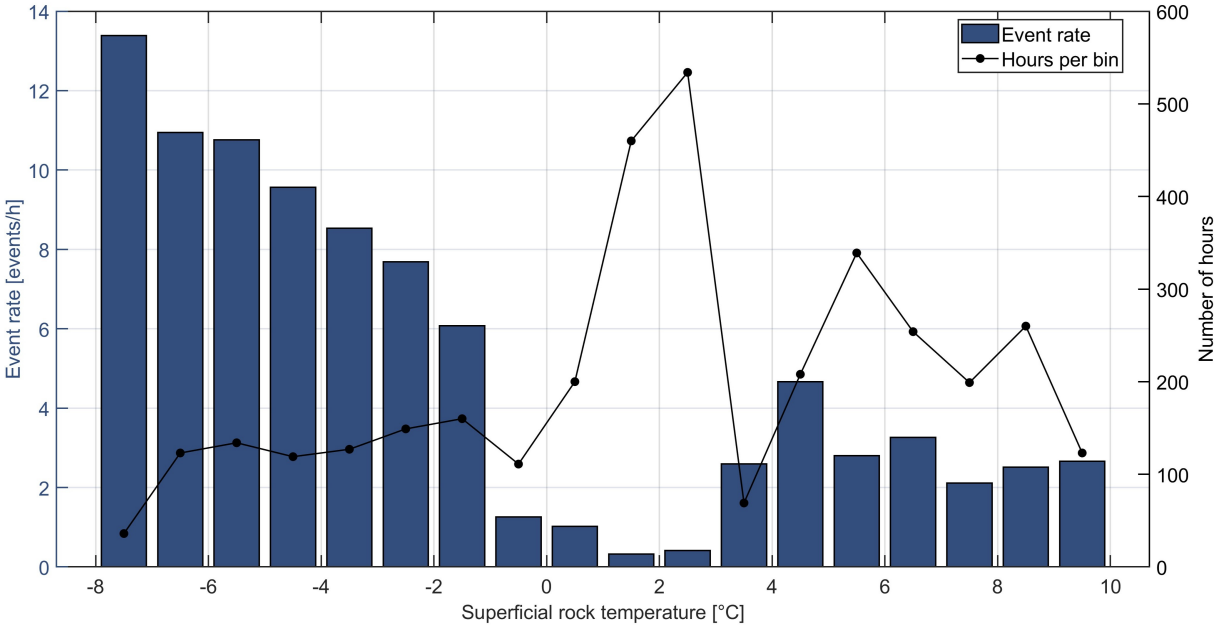

Figure 3.48: Rock temperature influence on microseismic event occurrence. For each 1 °C temperature bin, the mean number of events per hour occurring within that bin is reported, along with the total number of recorded hours falling in the same temperature range. Data from period 1 and period 2 were combined for this analysis.

Similarly was done for wind (Figure 3.49). It was investigated whether the number of events occurring per hour was somehow related to the wind speed intensity. It resulted that the number of MS events increased with wind speed intensity. However, the number of hours with high wind intensity was very few. For this reason, this relationship should be further investigated over a longer time period to obtain a more statistically robust result.

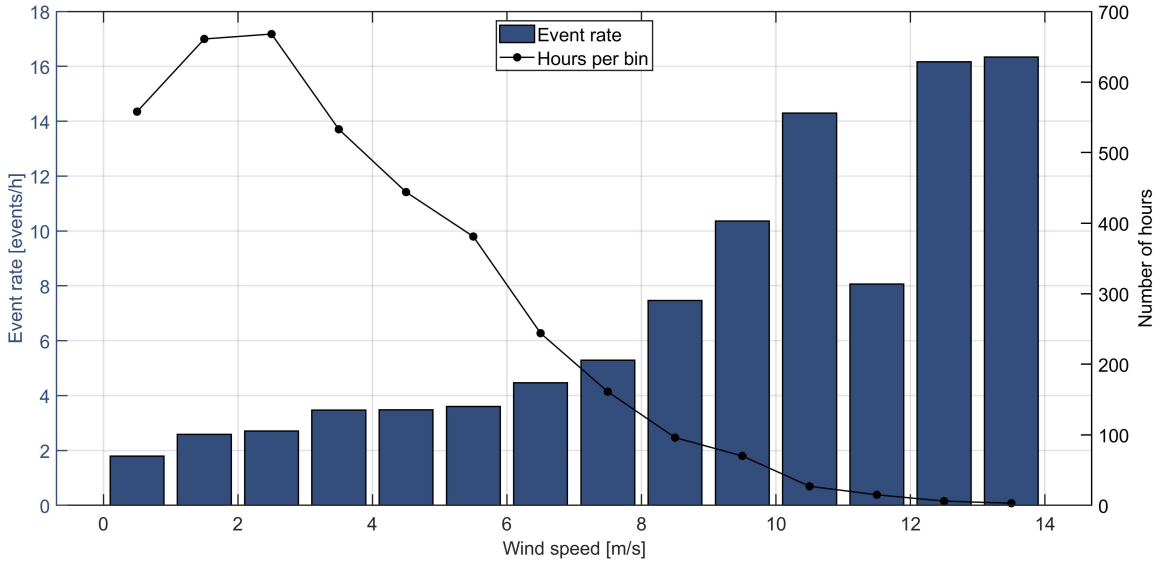

Figure 3.49: Wind speed influence on microseismic event occurrence. For each 1 m/s wind speed bin, the mean number of events per hour occurring within that bin is reported, along with the total number of recorded hours falling in the same wind speed range. Data from period 1 and period 2 were combined for this analysis.

Moreover, the occurrence of events along the day was investigated (as already done for GEA06). Considering both monitored periods together (Figure 3.50), it turned out that the events are quite distributed homogeneously throughout a day, with a slightly higher occurrence in night hours. However, if the three periods of the different observed trends are analysed separately, it emerged that during September and October 2024, there was a marked difference between the occurrence of events during day and night, while in November and December this discrepancy was less marked. In period 2, it seems quite an opposite pattern, with a lot of events occurring in the central hours of the day. However, there is no clear pattern within a day.

This observed behaviour could be related to the fact that, up to the 9$^{\text{th}}$ November 2024 (Panel a, Figure 3.51), the superficial rock temperature was still above 0 °C but very low. Lower noise during cold nights could have led to the extraction of more events. Conversely, during November and December, when rock temperature was always below 0 °C, the difference between day and night noise was less marked, leading to a more homogeneous extraction of events throughout the day. A longer monitoring period is still needed to achieve a more complete understanding of this behaviour.

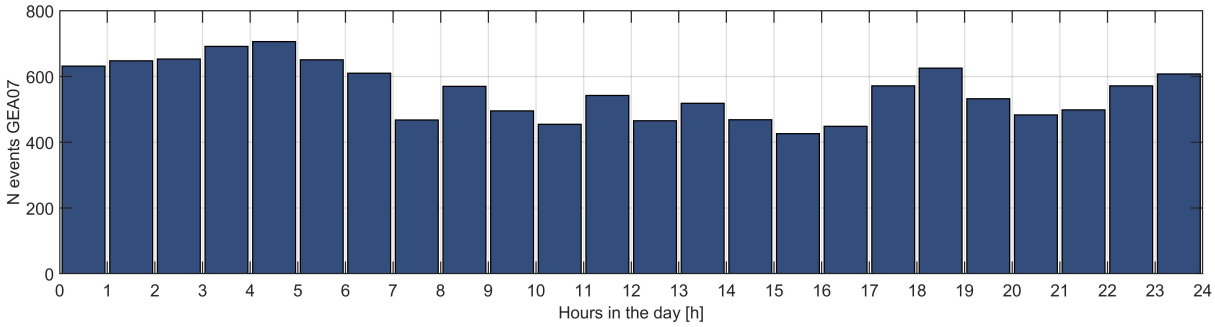

Figure 3.50: Distribution of microseismic events, extracted from GEA07 ambient seismic noise and filtered, across different hours of the day. Data from period 1 and period 2 were combined for this analysis.

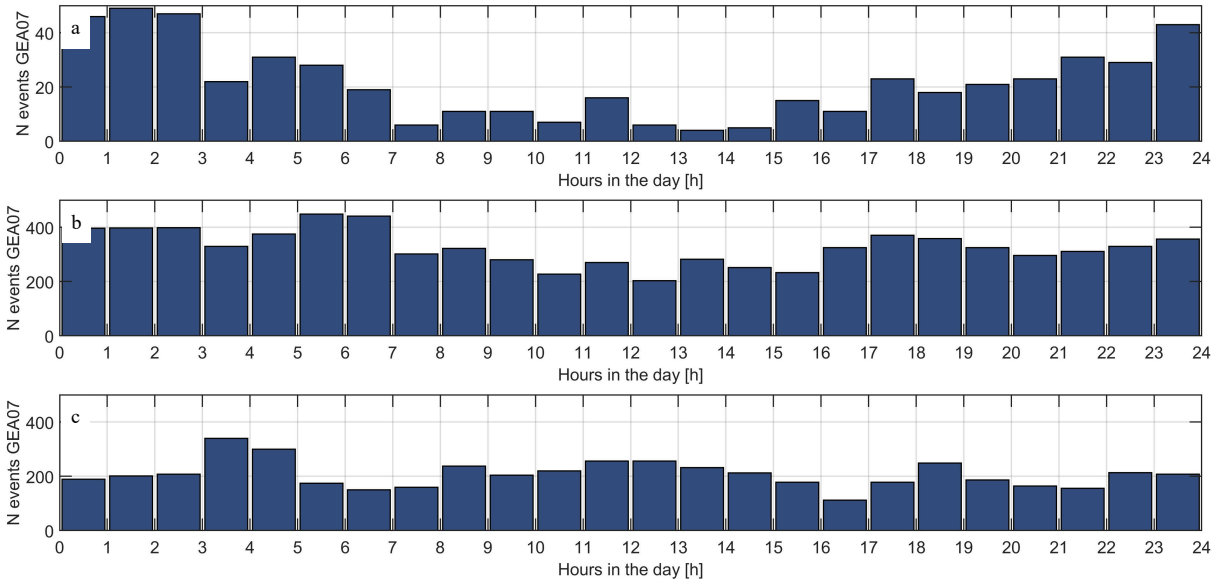

Figure 3.51: Distribution of microseismic events, extracted from GEA07 ambient seismic noise and filtered, across different hours of the day in different time periods. (a) First part of period 1, up to the 9th November 2024. (b) Second part of period 1. (c) Period 2.

3.5.6 ERT

Method

The ERT survey was performed in two different campaigns, on 26th June and 4th September 2025.

The acquisition configurations were Dipole-Dipole (with a total of 497 measurements) and Wenner-Schlumberger (with a total of 871 measurements). The acquired profile is shown in Figure 3.7.

The instrument used was a georesistivimeter Syscal Pro (Iris Instruments), with 48 electrodes for each acquisition, spaced at about 0.5 m, placed horizontally within the Dolomia Principale (Figure 3.52). Standard stainless steel electrodes were used, along with a conductive cement grout to improve the coupling between the electrodes and the rock.

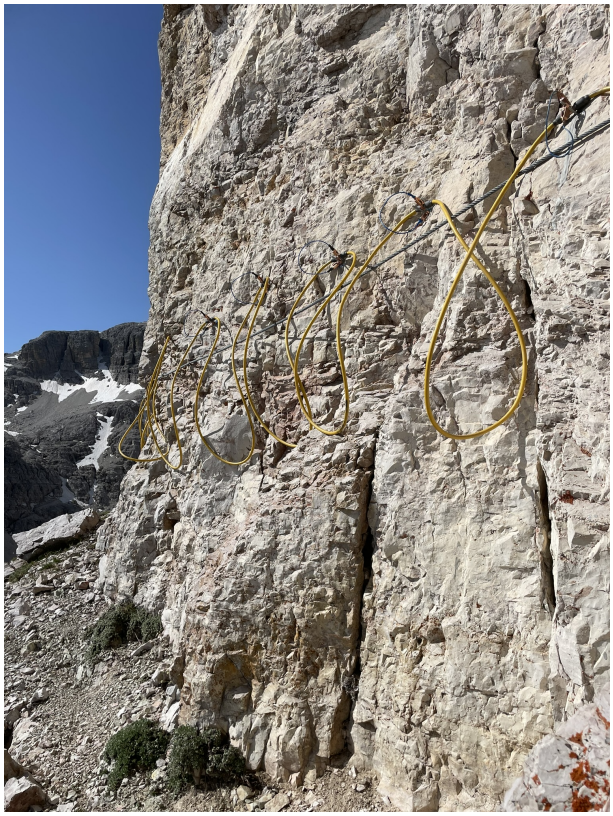

Figure 3.52: Electrode settings at the site.

The acquisition settings of the instrument were an injection time of 500 ms and a minimum of 5 up to 10 stacks. The accepted error percentage on the stacks was 2%.

As a standard practice, each ERT acquisition was preceded by a check of the contact resistance between the electrodes and the ground. This operation ("RScheck") was directly performed by the instrument.

Once collected, the ERT data were pre-processed using the software Prosys-III (Iris Instruments), performing filtering to remove data with negative resistivity values, isolated extremely high or low resistivity values (i.e. outliers), and values with standard deviation greater than 3%. The filtering results in a reduction of the number of available measurements, as reported in Table 3.5.

Table 3.5: Number of ERT measurements after the filtering performed with the software Prosys-III (IrisInstruments) on Dipole-Dipole and Wenner-Schlumberger arrays.

Array	**26th June 2025**	**04th September 2025**
Dipole-Dipole	646	696
Wenner-Schlumberger	844	620

It is worth noting that the filtering of the September Wenner-Schlumberger survey led to a significant reduction in the number of measurements, most of which were near-surface data.

The filtered ERT data were then exported as a `protocol.dat` file; an example of its format is reported below.

```
1490
1 1 45 21 25 20.1400934 0.2
2 1 37 17 21 74.44405321 0.36
3 1 29 13 17 13.10792882 0
4 1 21 9 13 52.32095945 1.32
5 1 13 5 9 308.5848765 0.61
6 1 47 23 25 9.755938667 0.07
```

In the file, the first row reports the total number of measurements (already filtered). The first column is the progressive number of measurements (from 1 to the total number), columns 2–5 are the electrodes involved in the quadrupole, column 6 is $\Delta V/I$, and column 7 is the standard deviation.

The results from the two arrays were combined prior to inversion to take advantage of both configurations. The 2D ERT inversion was performed using the open-source package ResIPy (*Blanchy et al., 2020*), a software developed to facilitate the processing, modeling, and inversion of geoelectrical data. ResIPy is written in Python and is open source (source code is available on a GitLab repository: https://gitlab.com/hkex/pyr2). It conducts inverse modeling using a weighted least-squares objective function coupled with a range of regularization options (*Binley, 2015*):

$$\Phi = \|W_d(d_{\text{obs}} - F(m))\|^2 + \lambda^2 \|W_m(m - m_{\text{ref}})\|^2 \tag{3.3}$$

where d_{obs} represents the measured apparent resistivities, $F(m)$ the calculated data from the model parameters m, W_d the data weighting matrix (typically containing the inverse of the measurement standard deviations), W_m the model roughness matrix, and λ the regularization parameter controlling the trade-off between data misfit and model smoothness.

Results

The inversion results are presented in Figures 3.53–3.54. Electrode coordinates (provided as input to the inversion software) were taken from the photogrammetric model produced by ARPA Valle d'Aosta, based on the reference system RDN2008/UTM zone 32N (EPSG:6707). Rock temperature data (shown in Figure 3.55) were measured at the two multiparametric columns DMS1 and DMS2 at the time of the ERT surveys. It can be observed that external temperature affects the rock temperature primarily within the first few meters of depth. Indeed, while the temperature at Module 19 (the shallowest, located at 0.5 m) differed significantly between the two survey dates, the deeper internal rock temperature remained almost the same on both dates, although in June a greater number of depths recorded temperatures below 0 °C.

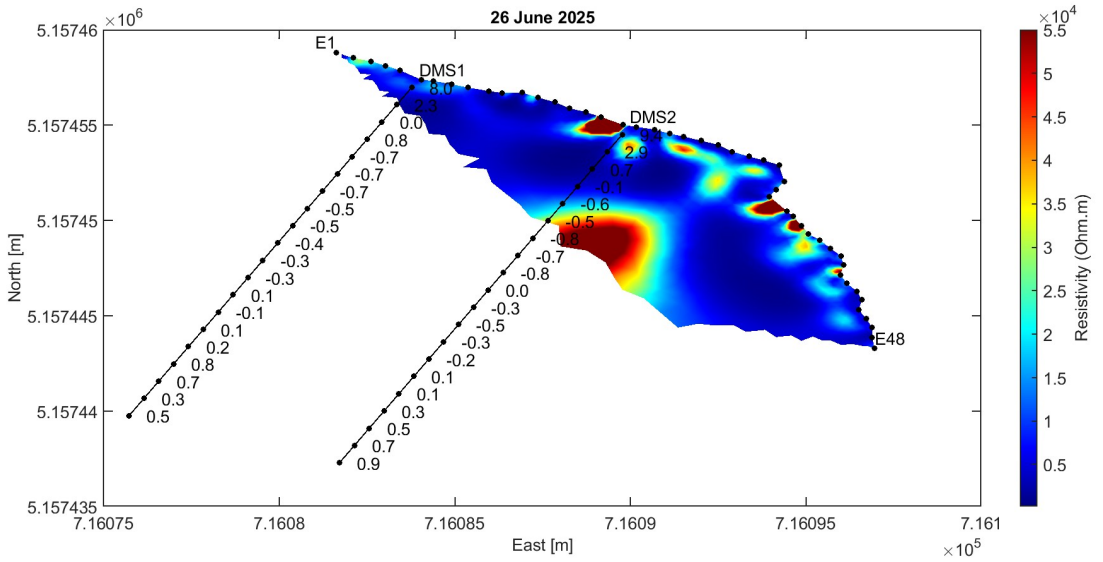

Figure 3.53: Resistivity model obtained from the inversion of the ERT performed on 26$^{\text{th}}$ June 2025. Both Dipole–Dipole and Wenner–Schlumberger data were used for the inversion. Dots along the surface indicate the electrode positions, from electrode 1 (E1) to electrode 48 (E48). The lines with dots represent the multiparametric columns, showing rock temperature in °C at each module depth (every 1 m).

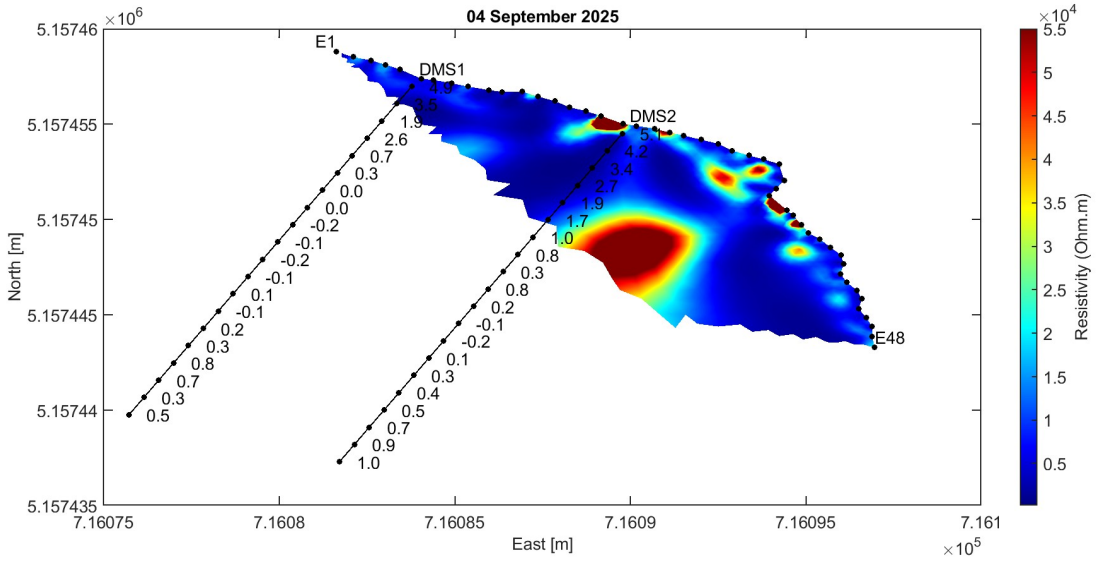

Figure 3.54: Resistivity model obtained from the inversion of the ERT performed on 4$^{\text{th}}$ September 2025. Both Dipole–Dipole and Wenner–Schlumberger data were used for the inversion. Dots along the surface indicate the electrode positions, from electrode 1 (E1) to electrode 48 (E48). The lines with dots represent the multiparametric columns, showing rock temperature in °C at each module depth (every 1 m).

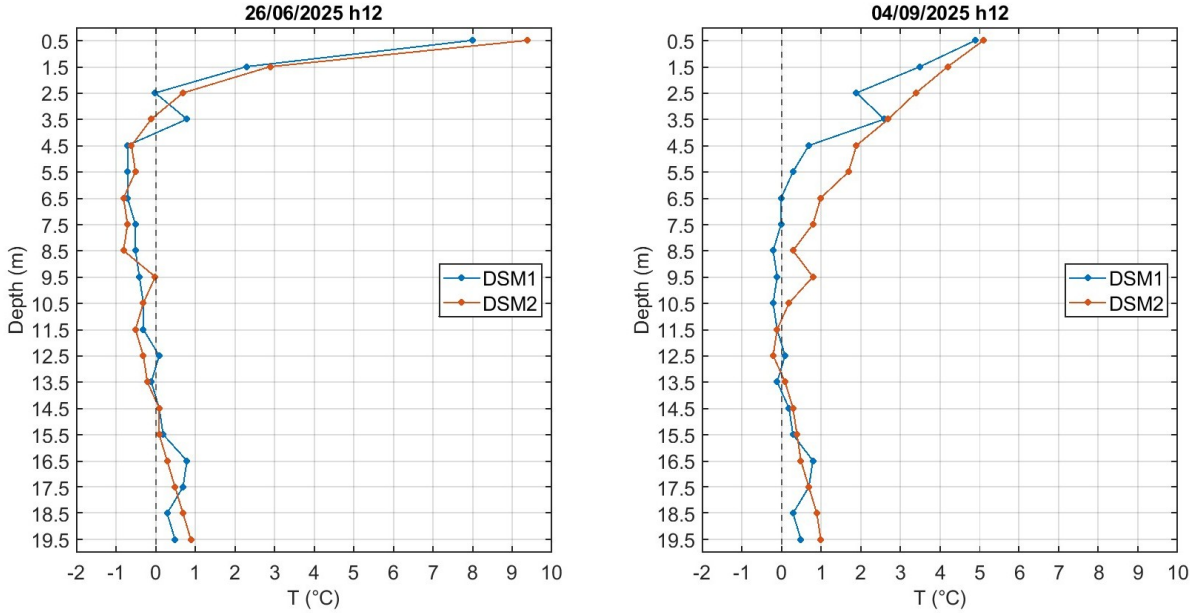

Figure 3.55: Rock temperature with depth at the multiparametric columns DMS1 and DMS2 measured during the ERT surveys.

An investigation depth of about 6 m was reached in the middle of the arrays; hence, especially at the corners, only a limited rock depth was investigated.

Overall, similar resistivity values were observed in both surveys, ranging from 237 to 1×10^6 Ohm·m in June and from 261 to 2.2×10^6 Ohm·m in September. The Dolomia Principale mostly shows values in the range of 500–1500 Ohm·m, while the deeper anomaly exhibits values from 60000 to 80000 Ohm·m.

Resistivity models were first interpreted using photos from the photogrammetric survey to understand the nature of the high superficial resistivity features. All of them turned out to be visible fractures, likely filled with air. Both in June and in September, there are near-surface higher resistivity bodies (with respect to the bulk resistivity of the Dolomia) which are very close to the rock surface and could still be filled with air due to the highly fractured nature of the rock itself. Between June and September, some of the superficial features changed but were not investigated since, as mentioned before, during filtering many superficial data were removed from the dataset due to their low quality; hence, the resistivity model very close to the surface was not considered feasible.

The main focus of the analysis is the high resistivity feature present at greater depth, which appears to change in location and shape between June and September. Looking at the inversion result of the ERT survey performed in June (Figure 3.53), it can be observed that it is very close to DMS2, at 4–6 m depth, where registered rock temperatures are below 0 °C. This could suggest it is an ice lens or a permafrost isolated patch (see permafrost classification in Section 4.1). According to this hypothesis, we expected a retreat in the ERT survey of September; however, this high resistivity feature appears closer to the surface and less extensive, farther from the DMS2 column, which cannot be used anymore to provide a clue on the rock temperature at the high resistivity body itself. Hence, with just these two surveys, it seems that there is a deeper anomaly subject to seasonal fluctuations both in size and in position, but with only these two inversions it is difficult to understand exactly what it is.

4. Climate change and future projections

4.1 Permafrost

According to its definition, permafrost is any ground that remains completely frozen (at 0°C or below) for at least two years straight (*NASA, 2025*).

Frozen grounds are typically found in cold regions such as Earth's high latitudes or in high altitude mountains as in this case study. All over the world, large regions are covered by permafrost and about 15% of the Northern Emisphere has it, covering about 22.8 million km^2(*National Geographic, 2023*).

Permafrost is the result of the combined effect of frost and negative temperatures and it results from a negative energy balance at the ground surface. The latter mainly depends on the direct incoming solar radiation and on the sensible heat flux. For this reason, permafrost is encountered in the Alps mainly at high elevations, where air temperature (controlling the sensible heat flux) is low. At lower altitudes can still be found especially on north facing slopes, because of a reduced incoming solar radiation due to slope angle and shadowing effects.

It consists of soil, gravel, and sand, held together by ice. Permafrost thickness can range from one meter to more than 1,000 meters; usually, near the surface, it contains large amount of organic carbon while lower permafrost layers contain mostly minerals. The upper layer, that thaws during summer and freeze again in autumn/winter, is called active layer; it can span from few tens of centimeters thickness to more than 1500 meters.

Permafrost is usually classified according to its extent (percentage of area) into continuous permafrost (90-100%), discontinuous permafrost (50-90%), sporadic permafrost (10-50%) and isolated patches (0-10%). "Mountain permafrost" is somewhat off these categories since its defintion is exclusively based on its location at high altitudes (*Global Terrestrial Network for Permafrost, 2025*).

In order to understand the permafrost occurrence in the Alpine region, the University of Zurich and the University of Waterloo (Canada) developed the Alpine Permafrost Index Map (APIM) (*University of Zurich, University of Waterloo, 2025*). The APIM was modelled and designed within the scope of the Alpine Space Interreg Project Permafrost longterm monitoring network (PermaNET) and it shows an index of the estimated likelihood of permafrost occurrence for the entire Alps region (Figure 4.1).

The map results from an inventory of evidence indicating the presence or absence of permafrost, made thanks to the effort of several countries and institutions. Contributors shared information from their respective research areas, consisting of existing data and knowledge. These data were further complemented by targeted investigations carried out

in collaboration with regional and local geological services, ski resort operators, engineering companies, and alpine guide associations. The final map is the result of a model calibrated based on that inventory dataset.

Within the study area, one of the monitoring sites of the PermaNET project is located at Lech del Dragon. This monitoring site is located approximately 800 m south-west of the Sas da Lech monitoring site. There, ground surface temperature (GST) measurements are collected; even if GST is not a direct measure of permafrost presence, being the temperature at the top of the active layer, it represents a key parameter for understanding the thermal evolution of both the active layer and the underlying permafrost, as well as frozen ground in general.

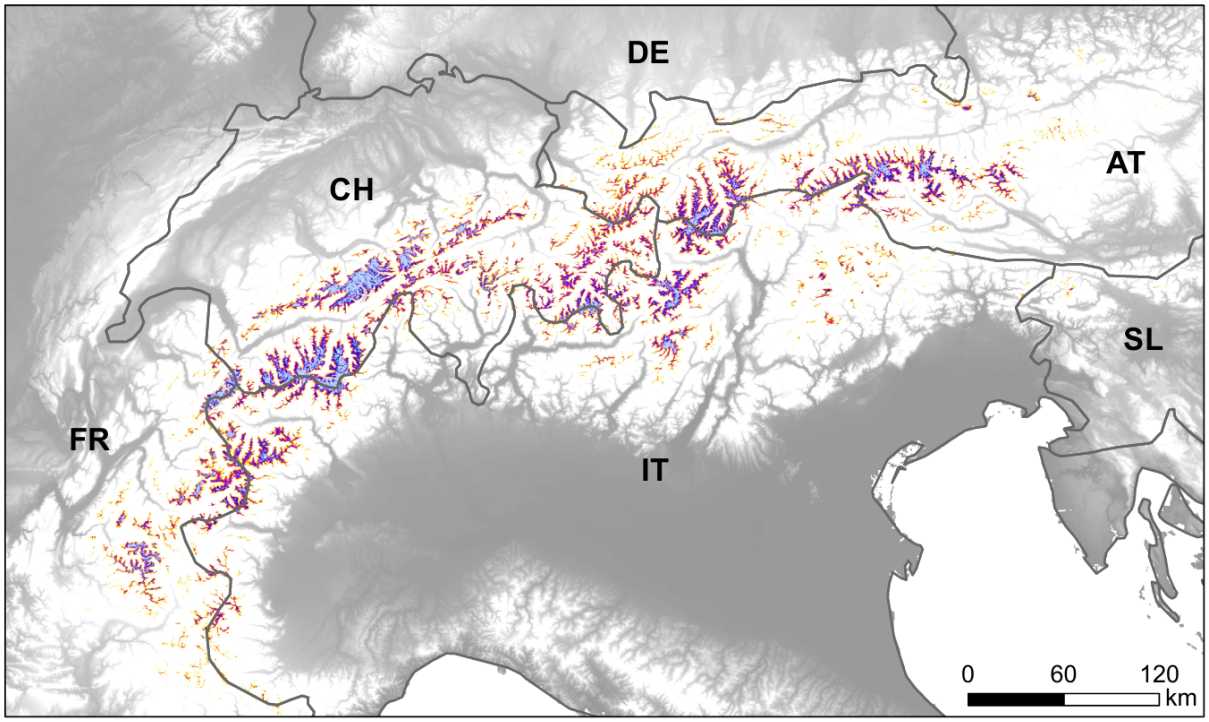

Figure 4.1: Alpine Permafrost Index Map (APIM) shown for the European Alps (AT: Austria, CH: Switzerland, DE: Germany, FR: France, IT: Italy, SL: Slovenia).

Being the Alpine Permafrost Index Map (Figure 4.1) available as a GIS layer with a spatial resolution of approximately 30 m, it was used in order to zoom over the study area, resulting in figure 4.2.

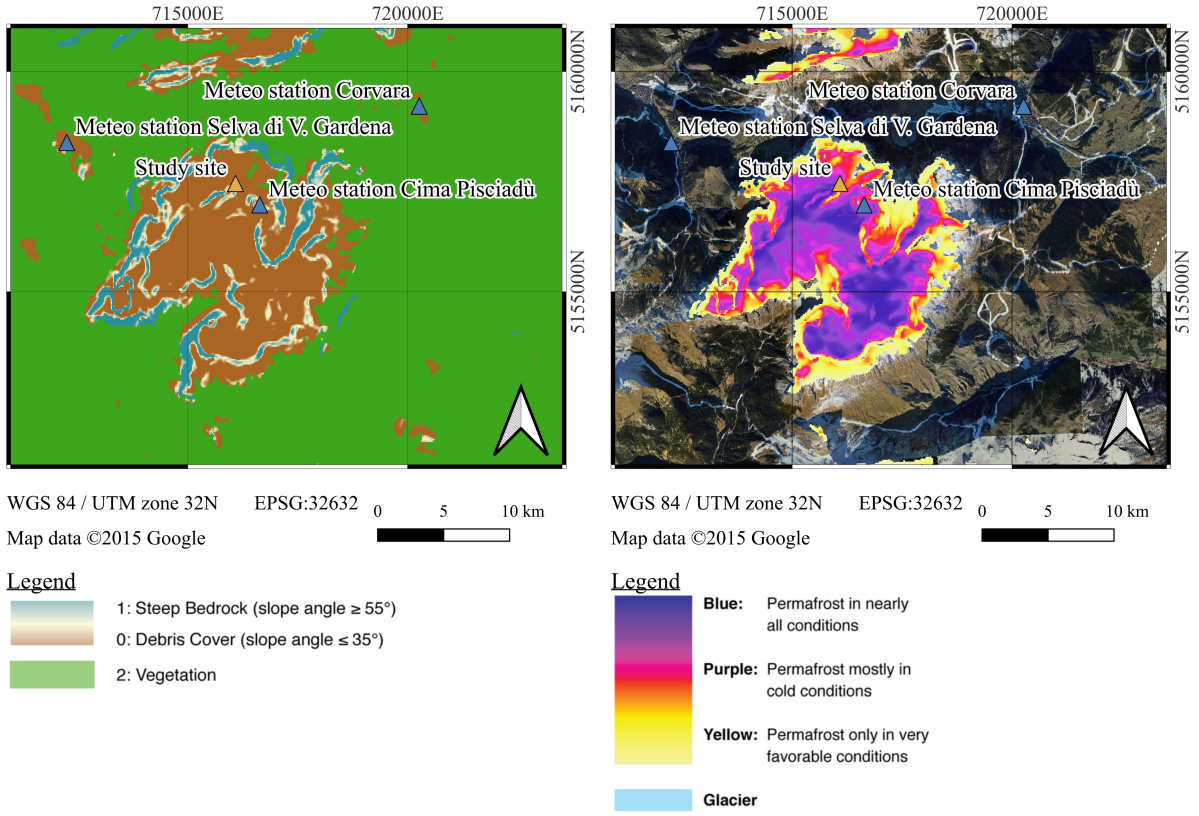

Figure 4.2: Left map: surface type map zoomed over the study area. Right map: APIM zoomed over the study area. Realised using QGIS (*QGIS Development Team, 2023*).

The surface type map is provided to understand which models were applied in the different regions according to the slope (debris and rock models). Focusing on the Sas da Lech case study, the steep bedrock surface condition is found. It has to be noted that, in general, over steep rock slopes there are several degrees of heterogeneity caused by micro-topography and fracturing. Differences are also due to the fracture setting and the sun exposure, which is almost absent at the monitoring site, being located on the north face of the Sas da Lech.

Moreover, it has to be highlighted that the APIM shows estimated conditions; hence, the models applied have estimated the permafrost presence within the analysed rock formation. However, a higher level of certainty can be achieved locally through geophysical investigations, as performed in this project.

From figure 4.2 can be observed that at the Sas da Lech, there is permafrost in nearly all conditions, and the same condition can be found in almost all the Sella Massif. This result will be used in support of the data collected at extensometer 21 (see Section 3.5.2).

Permafrost, along with inland waters and mountain glaciers, is highly sensitive to Climate Change, as permanently frozen ground is directly temperature dependent. Therefore, the importance of monitoring this target becomes evident. Indeed, ice acts as a binding agent that holds soil and rock together, preventing their movement. When it melts, however, the overall mass becomes less stable and may accelerate its movements, sometimes resulting in collapse, mudslides, or debris flows.

Permafrost reactions to climate change can be categorized as (*Kellerer-Pirklbauer et al., 2011*):

- thermal reactions
  - permafrost warming due to increased temperature
  - thawing of permafrost that leads to reduction in its spatial extent, active layer thickening and changing ground water circulation
  - changes in the number of freeze thaw cycles and magnitude of freezing and thawing periods
- geomorphic reactions
  - changes in the rate of rock glacier displacement
  - changes in the displacement mode of rock glaciers
  - changes in solifluction rates
  - changes in cryogenic weathering
  - changes in the volume and extent of unstable materials
  - changes in frequency and magnitude of mass movement events
  - surface instabilities caused by thermokarst processes/melting of permafrost ice.

A recent study done by the Swiss Federal Institute for Forest, Snow and Landscape Research (WSL) (*Jacquemart et al., 2024*) confirms that climate change is increasing the risk of natural disasters in the Alps, with rock falls and rock wall collapses that may occure more frequently as permafrost melts in the Alps. Indeed, they highlithed that one of the clearest climate-controlled trend is the increase in the rockfall frequency in high-alpine areas due to higher temperature.

In this work, the focus was primarily on investigating geomorphic responses—particularly those related to instabilities and movement variations. Special attention was given to the permafrost within the Raibl Formation, which appears to influence the displacement of the overlying rock columns. Furthermore, electrical methods (see Section 3.5.6) were employed to explore the possible presence of permafrost lenses within the rock columns themselves.

4.2 Temperature Variability: Historical Data and Future Projections

4.2.1 Climate Change in the Alps: Review of the Literature

Climate in the Alpine region is expected to be considerably affected by 21st-century global warming, not only due to rising temperatures, but also to changes in the seasonal cycle of precipitation, global radiation, and humidity, as well as changes in temperature and precipitation extremes, and closely related impacts such as alterations in snow cover and natural hazards.

When analysing climate change in such a complex region as the Alps, it is important to remember that this complexity translates into uncertainties in climate projections. Indeed, climate models must deal with challenges related to the complex orography and to several small-scale atmospheric phenomena. Other sources of uncertainty include internal

climate variability, assumptions related to the scenario and thus to future atmospheric greenhouse gas (GHG) emissions and aerosol concentrations, as well as assumptions and errors in both global and regional climate models and the downscaling methods used.

For precipitation patterns, projections are even more complicated; indeed, the Alpine region is located in the transition zone between the increasing precipitation trend of northern Europe and the decreasing one of the southern regions. Since at the monitoring site there are no precipitation data, this topic is not addressed in terms of future climate projections.

Mean wind speed, instead, is expected not to change considerably.

While, as far as temperature is concerned, higher rates of warming are often found at high elevations, mainly due to the snow–albedo feedback, but this is not always the case and depends on the region and the period under consideration.

Looking at the recent past, Nigrelli and Chiarle (2023) found that during the period 1991–2020 the Alps experienced a warming rate of 0.5°C per decade. This rate actually represents an acceleration that began in the 1980s, corresponding to roughly a 100 m increase of the zero-degree isoline every ten years. Overall, since 1880, temperatures have increased by 1.8°C in the Alpine region. This region is currently experiencing a greater warming than the global average, similarly to polar regions.

After reviewing recent trends, it becomes important to look ahead and see at climate projections.

Looking into the future, according to Gobiet et al. (2014), under the A1B emission scenario (energy system balance across all sources), in European Alps a warming of about 0.25°C per decade is expected until the mid-21st century, accelerating to 0.36°C per decade in the second half of the century. It must be noted that the expected rates of change in the 21st century are clearly below the observed rates in the past few decades, which were about 0.5°C per decade.

In the Alpine environment, where frost occurs at all altitudes but with varying intensity and duration, temperature changes affect many frost-related phenomena, but at different time scales (*Kellerer-Pirklbauer et al., 2011*):

- The diurnal freeze–thaw cycle, which is driven by air temperature, therefore follows the changing daily temperature range. Warmer temperatures are expected to reduce the frequency and intensity of this cycle at mid-altitudes, while increasing the frequency at high altitudes (where this small-timescale cycle is not the dominant frost phenomenon) and causing a seasonal shift toward earlier or later periods.

- The seasonal frost, which is subjected to complete thawing during warm months, is expected to replace permafrost in some regions, to decrease in depth and frequency at mid-altitudes, and to decrease in depth and duration at higher altitudes.

- At the largest scale, permafrost. Its lower limit is expected to migrate toward higher altitudes; sporadic permafrost will likely disappear at mid-altitudes, while continuous permafrost could be replaced by discontinuous permafrost. Permafrost exists in many steep rock slopes in high-mountain environments (as shown in Figure 4.1), and its degradation due to global warming can affect slope stability. However, the mechanisms of permafrost degradation and related slope stability are complex and often poorly understood.

Hence, in the future, we expect to observe some of these changes in the Alpine region, including at the monitoring site, which will be especially affected in terms of slope stability.

In the following section, an attempt to quantify these temperature changes is presented, with a focus on the studied area.

It must be made clear that this is not just a matter of climate change. In recent years, several collapses and instability events have occurred in the Alps. While climate change plays a role, geological and geomorphological factors are equally important. Rock wall destabilisation is the result of long-term processes that can span thousands of years, although weathering and climatic conditions can influence the timing of failure. Nevertheless, it is important to recognise the relevance of monitoring mountain sites in order to intervene and prevent disasters. This aligns with the project within which my thesis work is framed.

4.2.2 Historical Temperature Observations

Temperature data from the monitoring site are available only from the installation of the extensimeters with thermal sensors. Therefore, the first available data are from 22$^{\text{nd}}$ July 2024. Data are recorded every 30 minutes, and those analyzed cover the period up to the last data download, which occurred on 25$^{\text{th}}$ September 2025. Having just fourteen months of temperature data makes it impossible to use them to evaluate past temperature trends.

Unfortunately, the data from the nearest meteorological station, "Badia Cima Pisciadù", also do not cover a sufficient period, as they start from 14$^{\text{th}}$ June 2023, making a climate analysis unfeasible.

Hence, the nearest meteorological station above 2000 m was selected, which is Pian Fedaia (Diga) (*Provincia Autonoma di Trento, 2025*). There, temperature data are available from 24$^{\text{th}}$ September 1991 at daily resolution. The station is located at an altitude of 2063 m, with longitude and latitude of 11°51'46.3" E and 46°27'32.5" N, respectively. It is situated approximately 9 km south-south-east of the Sas da Lech.

At first, the data were plotted (Figure 4.3) to visualize missing values. Within the 34 years of records, only five small data gaps were detected. Missing values were replaced by the average temperature measured on the same day of the year across the entire dataset. For this purpose, a reference vector containing the daily averages was built ($\overline{T_{\text{daily}}}(t)$). In addition, to maintain a balanced dataset with the same number of measurements for each day of the year, data were truncated to complete years; the vector obtained after these operation will be called in the following $T_{\text{filled,cut}}(t)$.

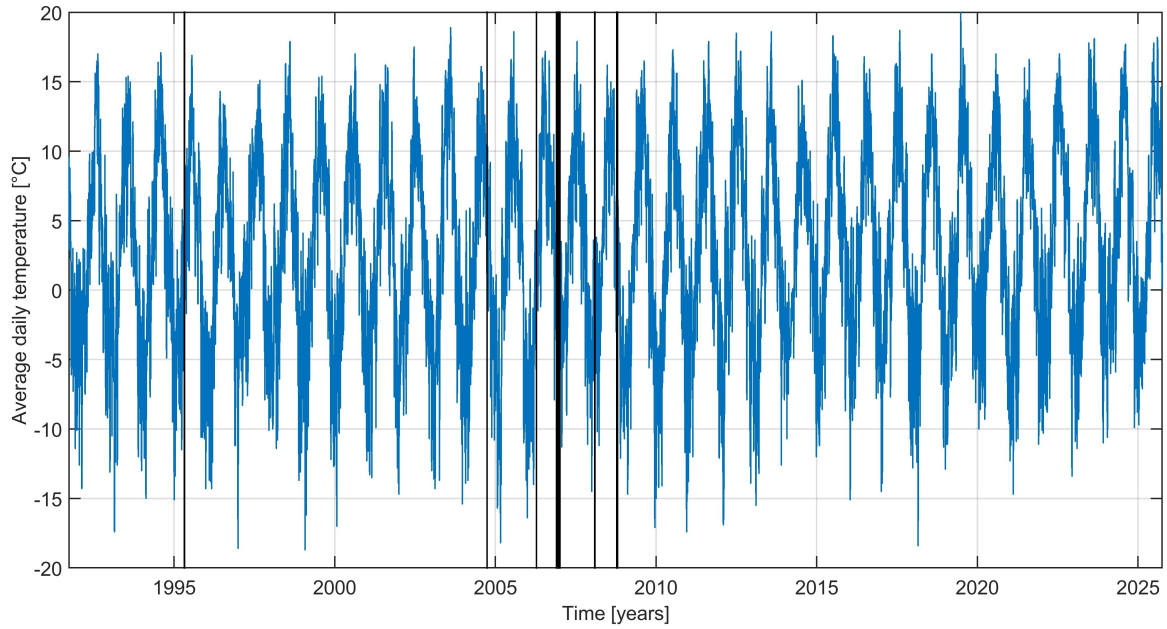

Figure 4.3: Daily temperature time series from the Pian Fedaia meteorological station; vertical black bars indicate missing data.

Those data were compared with air temperature data measured by extensometer 21 in the monitoring site to evaluate whether they can be used as a proxy for the site's thermal conditions. Extensometer data were first averaged on a daily scale to match the temporal resolution of the meteorological station and plotted (Figure 4.4).

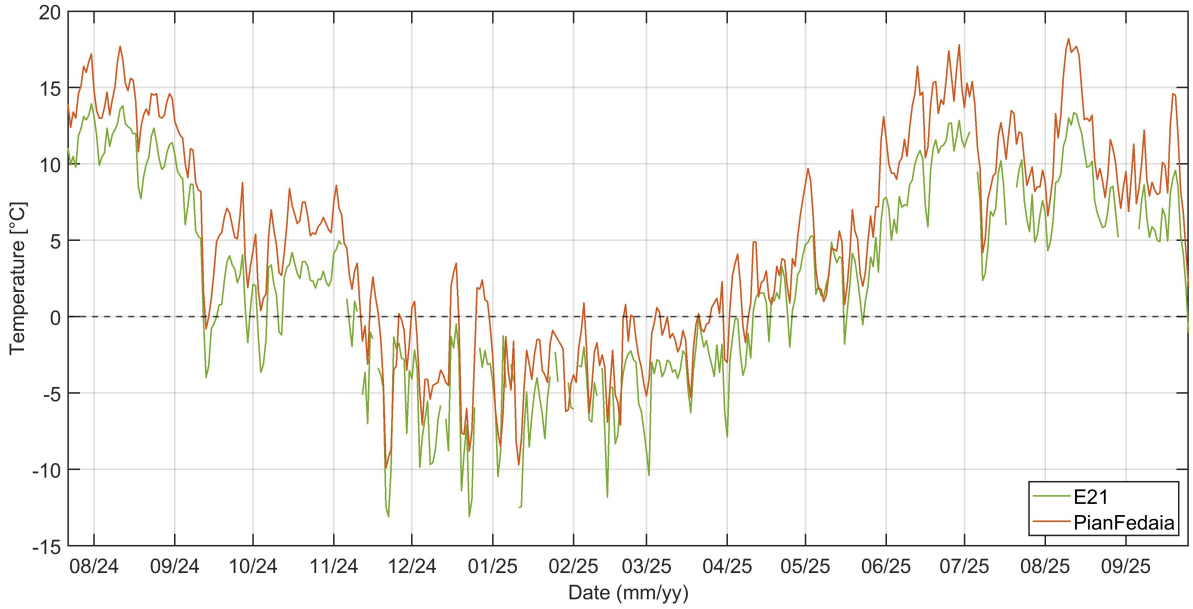

Figure 4.4: Comparison between daily air temperatures measured Pian Fedaia meteorological station and at the monitoring site (Extensometer 21)

For both datasets, not only the mean daily temperature but also the daily minimum

and maximum values were available, allowing for the computation of the daily thermal range. By computing the difference in daily mean temperature between Pian Fedaia and Extensometer 21 (always calculated as Pian Fedaia minus Extensometer 21) over the entire period, an average offset of 2.81 ± 1.35 °C was found, likely due to the slightly higher altitude of the monitoring site (approximately 700 m difference).

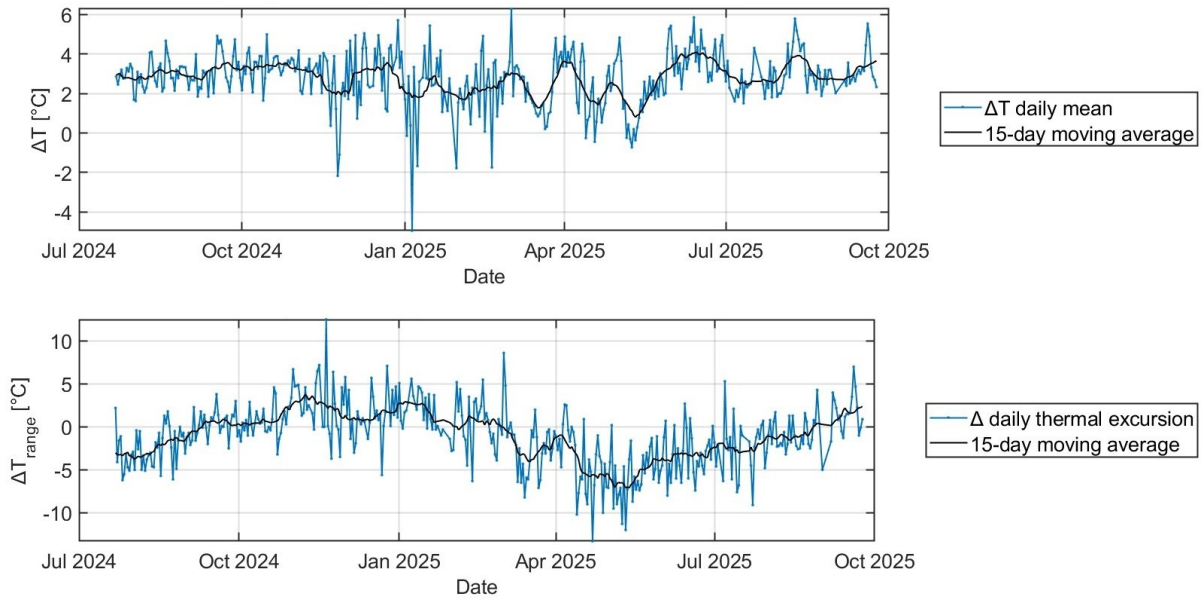

Figure 4.5: Difference in the daily mean temperature between extensometer21 and Pian Fedaia, with a 15-day moving average to better highlight the temporal trend throughout the all period (top plot). Difference in the daily thermal range between extensometer21 and Pian Fedaia, with 15-day moving average to visualize better the trend (bottom plot).

It can be observed that the Pian Fedaia meteorological station recorded temperatures almost always higher than those measured at Sas da Lech, with an approximately constant difference between the two locations throughout the year. Conversely, when examining the difference in daily thermal range, it can be highlighted that during the cold months (September–March) the two locations show nearly the same range, whereas during the warm months (April–August) the difference becomes negative, indicating that the thermal range at the monitoring site is higher.

Since this comparison was performed using only the available data, a more robust assessment would require a longer observation period. For this reason, the Pian Fedaia values were not corrected for the bias with respect to Extensometer 21, in order to avoid introducing an incorrect adjustment.

Nevertheless, despite their differences, the nearly constant offset in daily mean temperature throughout the year suggests that both sites exhibit a similar trend (assuming that this year of data is representative for both locations). The difference in thermal range makes Pian Fedaia less representative on the annual scale; however, the aim of this analysis is to investigate the long-term temperature trend, where mean values are of primary interest rather than daily extremes. Therefore, the Pian Fedaia data were used to evaluate the presence of a temperature trend over the period 1991–2025.

To estimate the temperature trend, two different strategies were applied. Since temper-

ature data exhibit a strong cyclical behavior due to astronomical and seasonal variations in solar radiation, to enhance the long-term trend, the first strategy consists of removing the periodic component. Indeed, whatever signal can be decomposed in a sum of cosine functions (Equation 4.1) with specific amplitude, frequency and phase and once defined can be removed from data.

$$\Psi(t) = \sum_{k=1}^{n} A_k \cos(2\pi f_k t + \phi_k) \tag{4.1}$$

where t is time in days, A_k is the amplitude in °C, f_k is the frequency in 1/day, and ϕ_k is the phase of the k-th harmonic component. The parameters A_k, f_k, and ϕ_k were derived from spectral analysis of the dataset using the following procedure:

```
dt = date_cut(2) - date_cut(1);                    % sampling
    interval [days]
N_sample = size(T_filled_cut,1);                % number of samples
T = dt*(N_sample-1);                               % total duration [
    days]
i = (0:N_sample-1);                                % sampling index
tr = dt*i;                                         % relative time
    vector
df = 1/T;                                          % spectral
    resolution
f = (0:N_sample/2)/T;                              % frequency vector
     up to Nyquist
Asp = abs(fft(T_filled_cut))/N_sample;          % normalized amplitude
    spectrum (FFT) of the gap-filled temperature time series
Asp(2:end) = 2*Asp(2:end);                         % true amplitude
PHsp = angle(fft(T_filled_cut));                % phase spectrum
```

where T_filled_cut is the daily temperature series, gap-filled and truncated to complete years while $date\_cut$ is the time vector corresponding to T_filled_cut.

From the amplitude spectrum (Figure 4.6) can be observed a strong frequency in the data, at 0.00273774 1/day. The latter corresponds to a period of about 365 days, representing the yearly periodicity; as expected, there is a temperature variation that repeats every year.

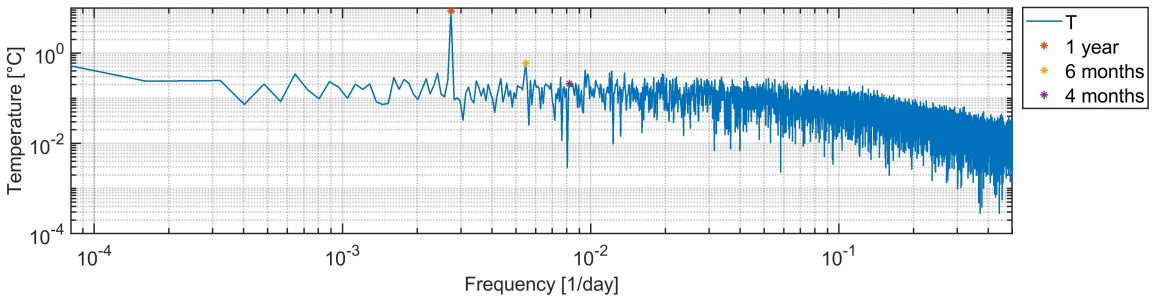

Figure 4.6: Pian Fedaia meteoreological station amplitude spectrum, with highlighted the main frequency corresponding to 1 years, 6 months and 4 months.

Amplitudes, frequencies, and corresponding phases of the three main periodic components (1 year, 6 months, 4 months) were extracted as:

```
[val, idx] = min(abs(f(:) - k*(1/365.25))); % k=1 (yearly), k=2
    (6 months), k=3 (4 months)
fk = f(idx);  % frequency of k-th harmonic
ak = Asp(idx); % amplitude of k-th harmonic
phk = PHsp(idx); % phase of k-th harmonic
```

The resulting periodic component was reconstructed as (Equation 4.2):

$$PC(t) = a_1 \cos(2\pi f_1 t + \phi_1) + a_2 \cos(2\pi f_2 t + \phi_2) + a_3 \cos(2\pi f_3 t + \phi_3) \tag{4.2}$$

The periodic component was then compared with the daily averages and the gap-filled, complete-year temperature data (Figure 4.7):

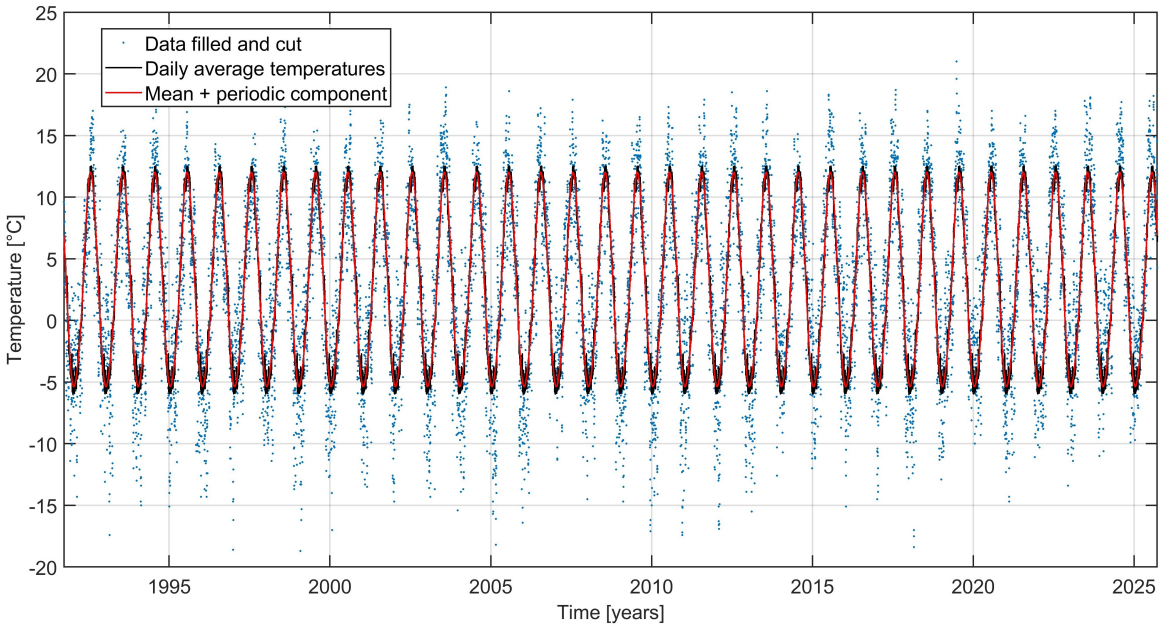

Figure 4.7: Pian Fedaia periodic component (red line), daily average temperature (black line), and gap-filled complete-year dataset (blue dots).

Residuals were obtained by subtracting the periodic component from the original data (Equation 4.3).

$$T_{\text{res}}(t) = T_{\text{filled,cut}}(t) - \left(\overline{T_{\text{filled,cut}}} + PC(t)\right) \tag{4.3}$$

Following strategy 2, instead, residuals were computed by subtracting the average temperature for each day of the year from the corresponding measurements (Equation 4.4).

$$T_{\text{res}}(t) = T_{\text{filled,cut}}(t) - \overline{T_{\text{daily}}}(t) \tag{4.4}$$

For both strategies, the residuals were fitted with linear regression in order to highlight possible increases or decreases of the temperature in the long-term (Equation 4.5).

$$T_{\text{res}}(t) = \alpha + \beta t + \epsilon \tag{4.5}$$

where $T_{res}(t)$ are the residuals (after removing the periodic component or the daily average), α is the intercept, β is the slope representing the trend in °C/day, and ϵ are the residual errors. The slope is finally multiplied by 365.25 to obtain the annual trend in °C/year, including its uncertainty.

The MATLAB (*The MathWorks Inc., 2023*) implementation is shown below:

```
Lfit = fitlm(tr, Tres, 'linear', 'RobustOpts', 'ols'); %fit
    linear model
Lpar = Lfit.Coefficients{:,'Estimate'};                % extract
    intercept and slope
SE = Lfit.Coefficients{:,'SE'};                        % standard
     error
Annual_trend = [num2str(Lpar(2)*365.25) ' \textpm ' num2str(SE(2)
    *365.25) ' [^\circ C/year]'];
```

where *tr* is the time vector expressed as number of days since the first one, the slope of the linear regression in °C/day is given by $Lpar(2)$ and $SE(2)$ is the standard error.

Results of the fitting are shown in Figure 4.8.

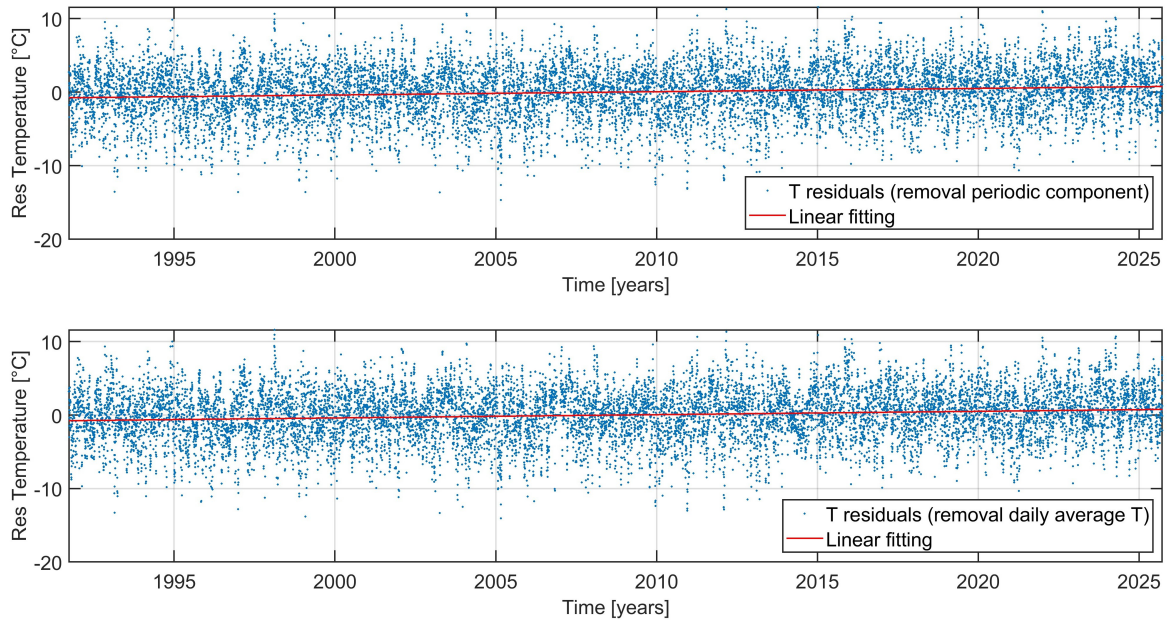

Figure 4.8: Pian Fedaia trend evaluated from residuals obtained by removing the periodic component (top) and the daily average temperature (bottom).

From both strategies, an annual trend of 0.045±0.003 (°C/year) was found for the period 1991-2025. This value aligns with the one found in literature for the Alpine region since the end of the last century (see 4.2.1), highlighting a strong warming in the site in the last thirty-four years.

The temperature data registered at Pian Fedaia (Diga) station were compared to the ones from the CORDEX regional climate model (*"CORDEX regional climate model data on single levels", 2019*), obtained from Copernicus Climate Data Store, in order to obtain correction parameters to then apply to the future projections and be able to perform a bias correction.

In table 4.1 are summarized the datasets used for the temperature analysis, along with the relative time windows considered. All the available-to-download Representative Concentration Pathways (RCPs) were used. In particular, the 4.5 scenario is a stabilization scenario for which radiative forcing level stabilizes at 4.5 W/m^2 before 2100 (approximately 650 ppm CO_2 equivalent)(*Thomson et al., 2011*) that represents an intermediate option scenario between the low-emission scenario with active mitigation (RCP 2.6) and the high-emission scenario (RCP 8.5).

Table 4.1: Dataset Information.

Type	**Source**	**Time Frame**
Historical	CORDEX	1991-2005
Observation	Meteo station Pian Fedaia	1991-2005
RCP 2.6 Scenario	CORDEX	2031-2100
RCP 4.5 Scenario	CORDEX	2031-2100
RCP 8.5 Scenario	CORDEX	2031-2100

Both historical and scenario datasets were downloaded as mean monthly air temperature data at 2m above the ground. After the download, the CORDEX data were filtered to extract the values corresponding to the nearest model grid cell centroid to the Pian Fedaia meteorological station.

The following table (Table 4.2) summarizes the characteristics of the datasets obtained from the Copernicus Climate Data Store (valid for both Historical and RCP selected scenario).

Table 4.2: Configuration of the CORDEX dataset downloaded from the Copernicus Climate Data Store for the climate analysis at Pian Fedaia meteorological station.

Database	CORDEX Regional Climate Model Data on Single Levels
Domain	Europe
Experiment	Historical, RCP2.6, RCP4.5 and RCP8.5
Horizontal resolution	0.11×0.11 degrees
Temporal resolution	Monthly mean
Variables	2m air temperature
Global Climate Model	CNRM-CERFACS-CM5 (France)
Regional Climate Model	CNRM-ALADIN63 (France)
Ensemble member	r1i1p1
Period historical	1991-2005
Period RCPs	2031-2100

To ensure consistency between datasets, the Pian Fedaia data were averaged to obtain monthly means, matching the temporal resolution of the historical dataset (Figure 4.9). The comparison was carried out over the period from September 1991 (first available Pian Fedaia record) to December 2005 (last available data from the scenario).

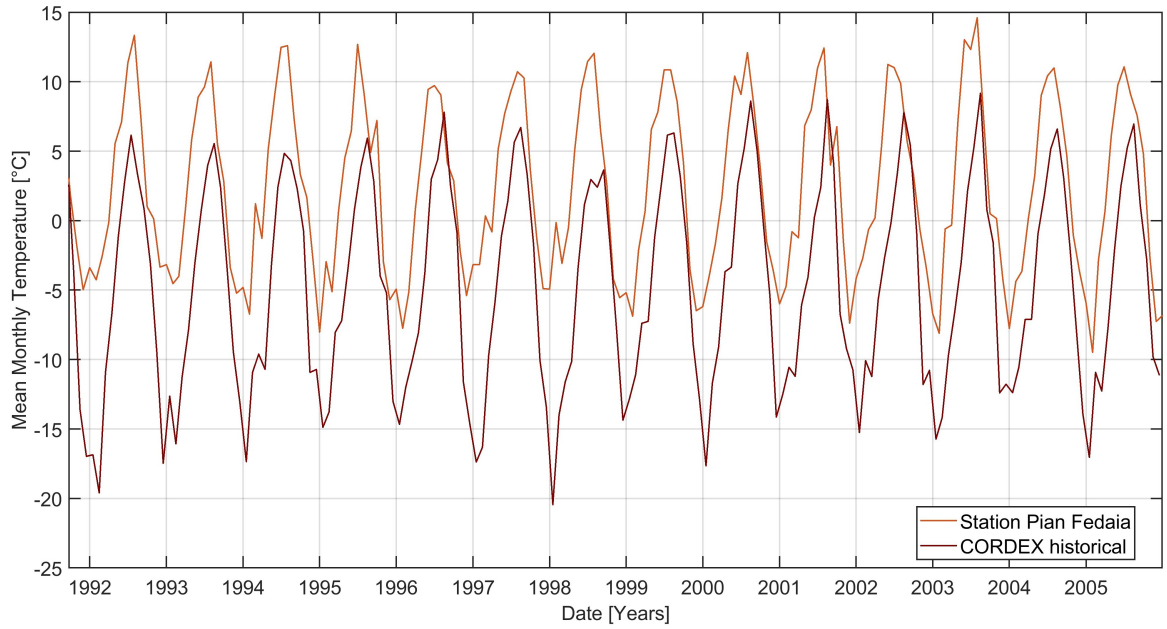

Figure 4.9: Monthly mean air temperature at Pian Fedaia meteorological station and of the historical scenario.

4.2.3 Projected Future Temperatures

The bias correction was performed according to a monthly delta method. Specifically, a 14-year mean (1991–2005) was calculated for each month, resulting in a monthly average value. The bias was determined by calculating the month-by-month difference between the observed value at the Pian Fedaia station and the historical value. This bias was then applied to the RCP scenarios data, as follows:

$$X_{\text{scenario,corr}} = X_{\text{scenario}} + \left(\overline{X}_{\text{historical,month}} - \overline{X}_{\text{observed,month}}\right) \tag{4.6}$$

where $\overline{X}_{\text{historical,month}}$ and $\overline{X}_{\text{observed,month}}$ are the monthly average values for the historical and observed data, respectively.

The results obtained from the bias correction are shown in Figures 4.10-4.12, where the raw data from Pian Fedaia, the historical data, the raw RCP scenarios data, and the bias-corrected RCP scenarios data are plotted.

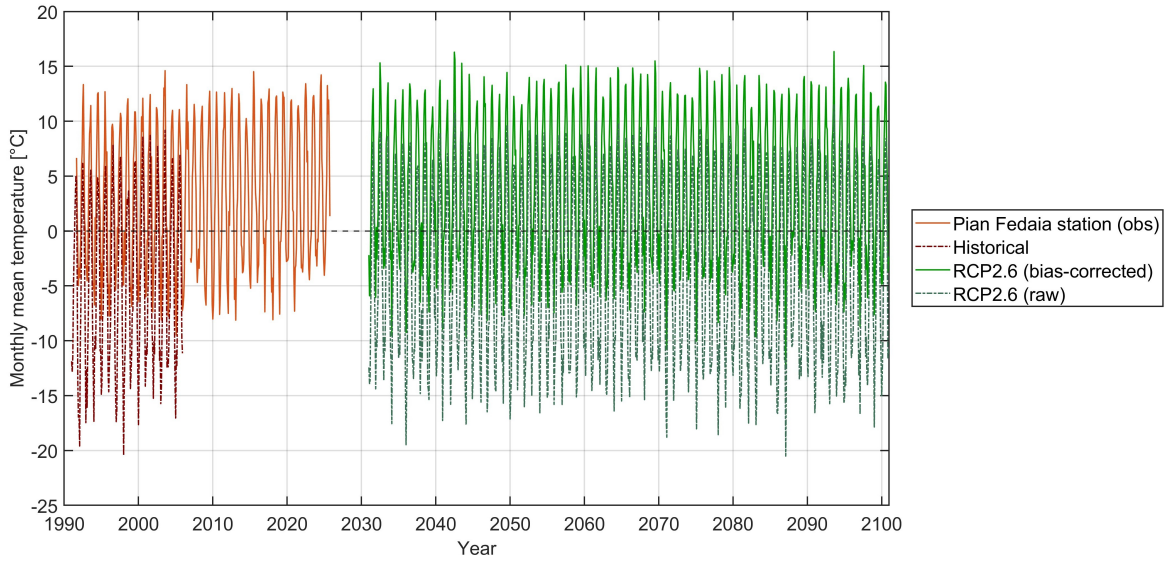

Figure 4.10: Comparison of monthly mean air temperature time series including raw Pian Fedaia data, historical data, RCP2.6 scenario data before and after bias correction.

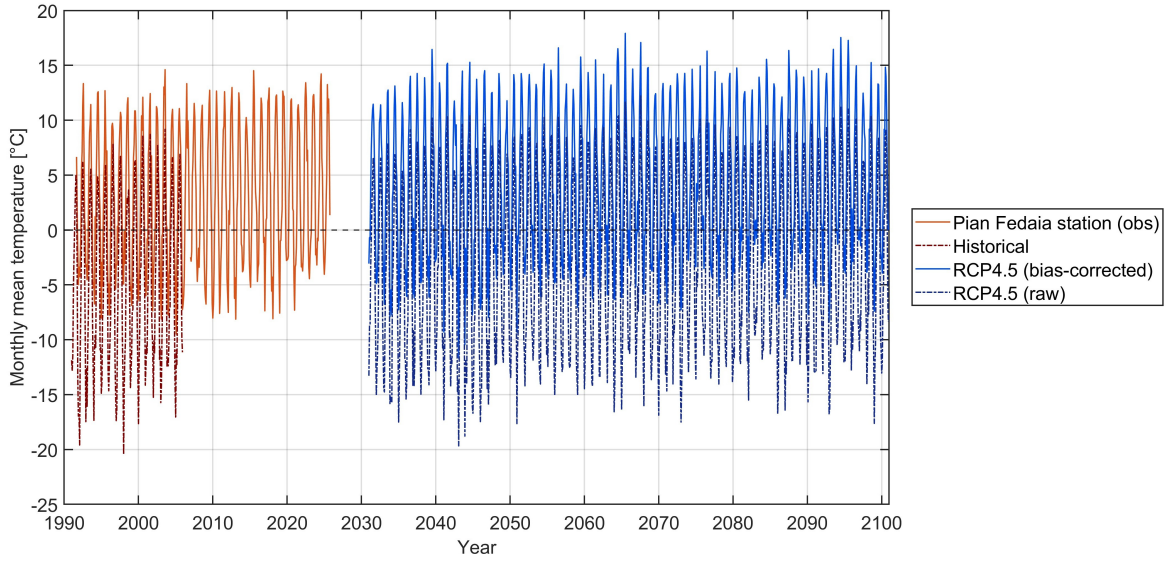

Figure 4.11: Comparison of monthly mean air temperature time series including raw Pian Fedaia data, historical data, RCP4.5 scenario data before and after bias correction.

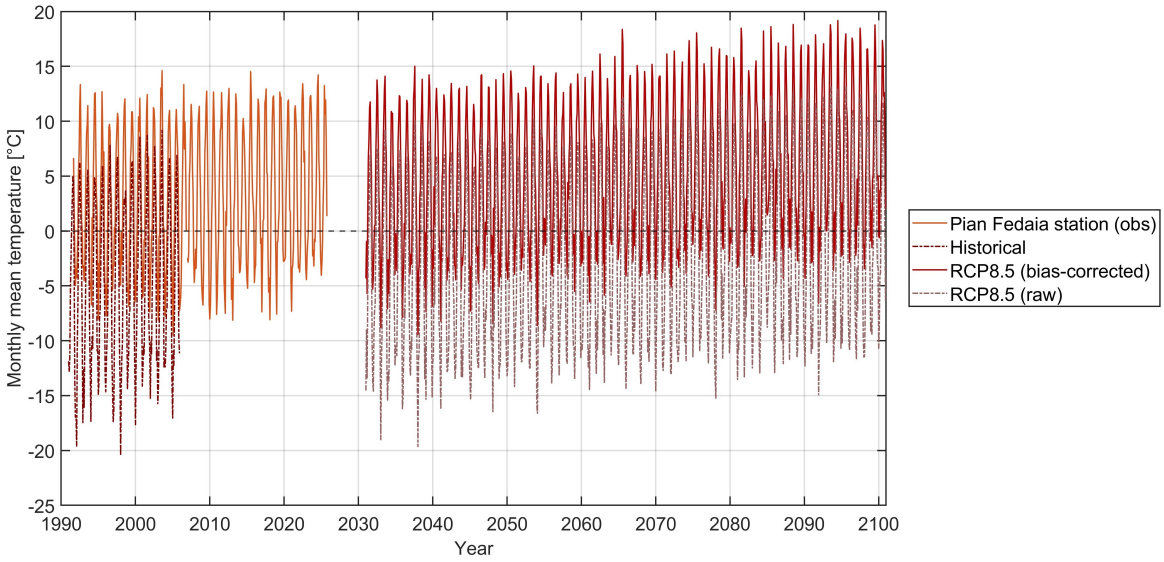

Figure 4.12: Comparison of monthly mean air temperature time series including raw Pian Fedaia data, historical data, RCP8.5 scenario data before and after bias correction.

The bias corrected mean monthly air temperatures of the RCP scenarios were aggregated and plotted at the annual scale, using a 5-year Gaussian smoothing filter to visualize the long-term trends of the different scenarios (Figure 4.13).

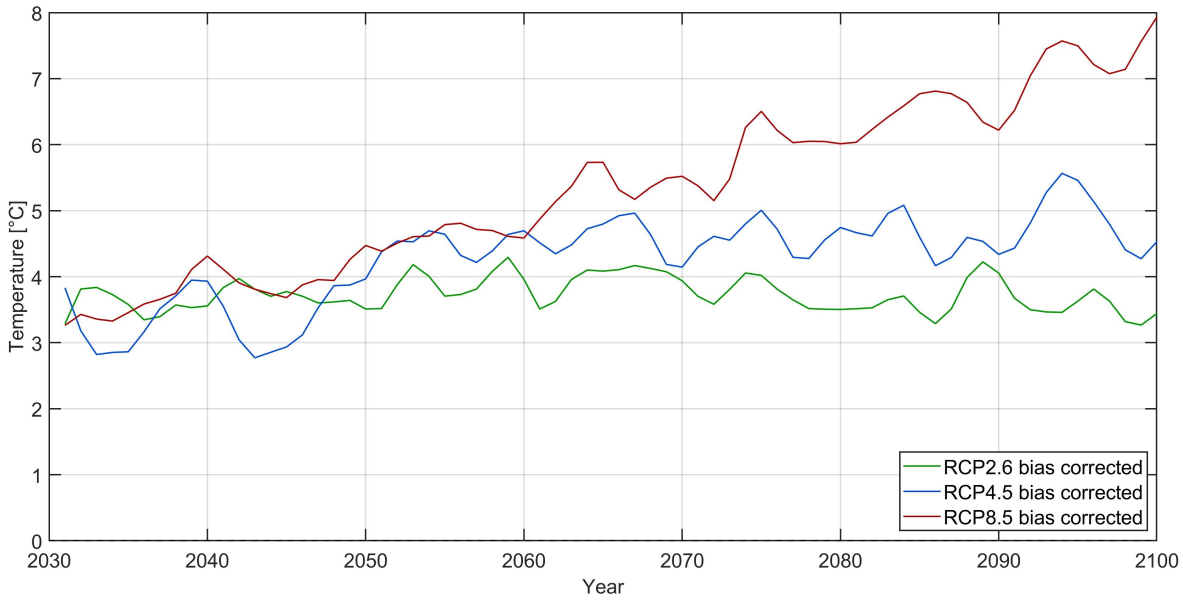

Figure 4.13: Annual mean temperature time series for CORDEX RCP2.6, RCP4.5 and RCP8.5 scenarios. The curves are smoothed using a 5-year Gaussian filter to highlight long-term trends. Data shown are bias-corrected.

On the bias-corrected data, the long-term trend was finally evaluated using the same procedure applied previously for the calculation of the yearly trend in the raw Pian Fedaia temperature data. The annual trends obtained are:

- 0.000 ± 0.003 [°C/year] for RCP2.6, showing steady thermal conditions until the end of the century.
- 0.025 ± 0.003 [°C/year] for RCP4.5, showing a decreasing trend from 2031 to 2100 with respect to that observed in the past 34 years, but still an increasing trend of the temperatures. This result aligns quite well with predictions found in the literature for A1B emission scenario, showing a slight decrease in the trend compared to the recent past.
- 0.062 ± 0.003 [°C/year] for RCP8.5, showing an even more rapid increase of the temperature with respect to the recent past.

The results obtained for the different scenarios show very different projections for the future, hence the importance of the pathway that will be taken in the future. Anyway, it is important to note that the bias correction was performed using the Pian Fedaia data and not directly with the monitoring site data, which shows an additional bias that could not be estimated in terms of long-term trend due to the limited availability of data at Sas da Lech.

5. Method assessment and future work

5.1 Advantages and limitations

Geophysical methods applied at the Sas da Lech are valuable monitoring methods; however, the performed analysis presented some limitations that affected the results and their overall quality:

- The climatic variables are not directly measured at the monitoring site, except for air temperature. The main issue is that during winter, when solar panels are covered by snow, data collection becomes intermittent. Wind data were considered representative of the site, although a bias is likely due to the different altitude and complex orography. Moreover, precipitation data are not available at the Cima Pisciadù meteorological station, making it difficult to determine when precipitation events actually occur at the monitoring site.
- CORDEX data are provided at a spatial resolution of 0.11×0.11 degrees, corresponding to approximately 100 km^2. Therefore, they cover a much wider area, including the Marmolada Massif, just the southern part of the Sella Massif and the valley between the two (Figure 5.1). In addition, historical data were not compared with the actual measurements at the monitoring site (due to the short available time series), but with those from the nearest meteorological station, which introduces some biases. This discrepancy could be related to orographic and climatic factors, such as altitude differences. Furthermore, the comparison covers less than 30 years of data because of the limited availability of recorded temperature data at the Pian Fedaia station.

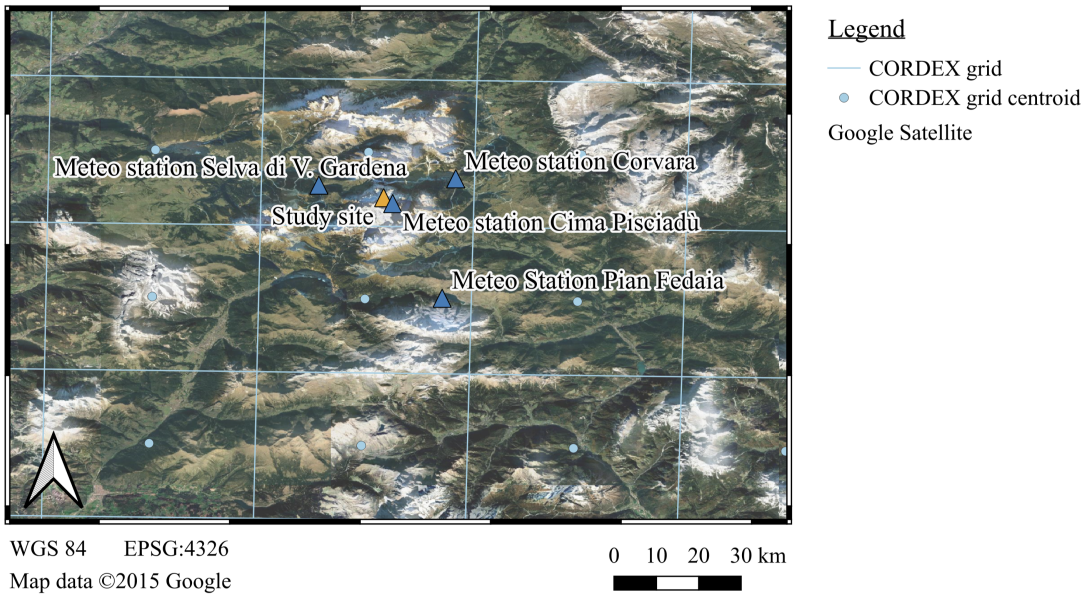

Figure 5.1: CORDEX grid over the study area. The study site is shown as an orange marker, while the available meteo stations are displayed in blue. Realised using QGIS (*QGIS Development Team, 2023*).

- For the climatic analysis, the bias correction was evaluated using only 14 years of past data, which were assumed to be representative of the long term.
- The site's difficult accessibility, together with the limited memory capacity of the geophones, made data collection challenging. As a result, it was not possible to record seismic data for an entire year, but only for the two analyzed periods. Moreover, GPS connection issues—mainly caused by the orography and the shadowing effect of Sas da Lech itself—further affected data acquisition. The accessibility did not allow to put geophones at the top of the rock columns, making all the performed analysis more complicated.
- ERT analyses were performed during only two measurement campaigns. Indeed, ERT survey is discrete in time, requiring the presence of an operator on site. Moreover, with electrodes that are almost horizontally aligned (as in the Sas da Lech monitoring site), only a horizontal cross-section at the electrode elevation can be obtained, along with the fact that it was not possible to reach great investigation depths. Furthermore, the array geometry used in this study is unconventional compared to a standard linear array, which poses challenges due to the lack of codes capable of handling such a configuration.

Conversely to ERT, long-term ambient-noise acquisition is a continuous recording method. The continuous recording is one of the main advantages of passive seismic applications. It allows to have a long-term recording, covering different time scale, without requiring on-site operators. Ambient seismic noise recording in such a natural environment, where anthropogenic sources are minimal, provides data for understanding of the overall behaviour of the monitored rock mass. The continuous nature of these recordings allows the detection of temporal variations, such as seasonal or weather-related changes. These characteristics make ambient seismic noise and microseismicity analyses valuable

monitoring tools, useful for understanding the triggering mechanisms behind mechanical instabilities and for subsequently tracking the evolution toward failure from an early-warning perspective. Moreover, passive seismics offers larger spatial coverage than ERT and is minimally invasive, making it particularly suitable for long-term monitoring in remote mountain areas.

Despite many disadvantages, the ERT survey was performed since it provides a resistivity image that offers a more detailed understanding of the internal structure of the rock mass at different depths. This obtained results allow to indirectly reconstruct the internal structure of the rock columns, while with passive seismic just a more general behaviour can be obtained. Especially thanks to the time-lapse, this electrical method can be very valuable in the understanding of the cross section of the rock columns at the monitoring site.

5.2 Future work

Other applied geophysical analyses could be investigated, such as cross-correlation, clustering, and the extraction of single resonance frequencies to perform cross-correlation with air temperature and understand the delay in the rock response. However, before that, a longer dataset would be useful in order to have enough data from both the stable and unstable compartments, capture all possible types of events throughout the year, and gain a more complete understanding of how resonance frequencies dominate and change over time. Hence, a longer dataset is required to achieve a more comprehensive understanding of the site's behaviour and to proceed with more robust analyses.

This would allow the investigation of phenomena on annual and seasonal scales and the observation of data from the currently missing months. Data covering multiple years would also be useful for identifying possible patterns or trends and would allow for a more complete understanding of the rock formation's response to external conditions.

Moreover, a photogrammetric model, together with a 3D model of the Sas da Lech itself, would be useful for studying the site and its responses through modeling, gaining a better understanding of the fracture setting, and potentially locating microseismic events to identify the most active parts of the rock formation. However, developing the 3D model would require a better understanding of the mechanical properties of both the Dolomia Principale and the underlying Raibl Formation, which will be achieved through collaboration with geologists from the University of Milano-Bicocca.

Additional ERT acquisitions are required to better interpret the observed data, both throughout the year and at greater depths. This may require a longer array, which should, however, be evaluated according to the geometry of the site.

6. Conclusions

Within the monitoring project conducted at the Sas da Lech site, the integrated analysis of ambient seismic noise, microseismicity, ERT, deformation and meteorological parameters has provided new insights into the behaviour of both the unstable eastern and northern rock columns. Being the site located at 2720 m, within a high-alpine periglacial environment, a lot of limitations were encountered related to data coverage, accessibility, and environmental conditions. Despite these limitations, the combined use of different geophysical methods (covering period 1, from 16/09/2024 to 18/12/2024, and period 2 from 26/06/2025 to 04/09/2025), deformation information and short- and long-term meteorological data has enabled a deeper understanding of the mechanical response of the rock mass and its relation to freezing–thawing dynamics.

Ambient seismic noise and HVSR analysis revealed the presence of three main resonance frequencies. They showed seasonal fluctuations in both unstable compartments. However, resonance frequencies are clearer and continuous for GEA07, indicating that the eastern rock column vibrates more than the northern one. This observed behaviour might be related to the more stable conditions below GEA06 throughout the monitored periods, less affected by thawing and freezing cycles due to lower solar radiation exposure. For both stations, two dominant frequencies were observed at approximately 5–5.5 Hz and 7 Hz, and a weaker one at 2.5–3 Hz. Overall, both GEA06 and GEA07 showed similar patterns in terms of resonance frequencies, with an increase around mid-November, temporally aligned with the decrease in temperature (suggesting a temporary stiffening of the rock mass linked to ice formation within or below the rock columns) and a weakening. Moreover, the two highest ones seem to somehow unify at the end of period 1, or one of the two disappears, without being that clear. The 5.5 Hz peak seems to have disappeared in period 2. This observed behaviour at the end of period 1 and within period 2 could be related to a question of constraints of the rock column, and a 3D modelling could be useful in the understanding of the reason behind that observation.

Since the obtained Power Spectral Densities and spectral ratios turned out to be very noisy, wind intensity was investigated, resulting to be not the only cause of noise, nor always a triggering factor. Besides the noise, a daily cyclicity was observed in both PSD amplitude and spectral ratios, driven by external air temperature, confirming the influence of thermal forcing on the ambient seismic response.

Microseismicity analysis provided complementary evidence of frost-related processes. Both columns showed a marked increase in microseismic events from around mid-November 2024, once rock temperatures dropped below 0 °C. However, this change in trend was much less marked for GEA06, as if it experiences early freezing of its shallow layers, generating microseismic events already from September. The observed increases support the interpretation that most of the extracted events were likely associated with freezing processes affecting shallow and deeper rock layers at different times for the two columns. While

correlations with below 0 °C temperature appeared within the analysed periods, wind intensity also seemed to play a role, but a longer recording would have made the result more robust.

ERT results offered a complementary view of the subsurface conditions, despite the constraints of site geometry and limited measurement campaigns. The time-lapse resistivity models revealed a high-resistivity feature at depth that changed in position and extent between June and September 2025, suggesting the presence of an isolated permafrost patch or of an ice lens affected by seasonal thermal variations. Although the shallowest layers could not be reliably interpreted due to electrode configuration and data-quality filtering, the deeper anomaly highlights the potential of ERT to capture internal structural features that cannot be detected from seismic data alone.

Given the strong thermal control over the seismic response of the site, a larger-scale climatic analysis was performed. The Sas da Lech lies in an area where permafrost is estimated to be present in nearly all conditions according to APIM, and the observed site behaviour is consistent with freezing processes especially within the underlying Raibl Formation. Temperature analyses confirmed a significant warming trend experienced in the last 34 years (0.45 °C/decade), and this trend is projected to halve during 2031-2100 according to the intermediate scenario RCP 4.5. However, the extreme scenarios show different trajectories: RCP2.6 exhibits no increase in mean temperature (0.0 °C/year), whereas RCP8.5 projects a an even stronger warming trend (0.062 °C/year). These results highlight the strong dependence of future temperature evolution on the emission pathway. Whatever will it be, In the context of ongoing climate change, the influence of the emission scenario is critical, but the role of geological and geomorphological factors must also be considered. Indeed, the response to external conditions is site-specific, according to rock lithology, orography, weathering, climate conditions, and ongoing geomorphological processes. These combined factors influence rock stability and highlight the importance of site-specific monitoring supported by an interdisciplinary approach that integrates geophysical, geological, and climatic knowledge.

Overall, while data limitations constrained the robustness of conclusions, the multimethod approach enabled the identification of seasonal patterns, freezing-related processes, and structural constraint controls on the behaviour of the rock columns. Future monitoring, with longer seismic time series, additional ERT campaigns, and mechanical modelling, will be crucial for refining the interpretation of the observed patterns, having a more complete understanding of variables controlling the columns' thermo-mechanical behaviour and hence being able to use the monitoring as an early-warning system.

Bibliography

Antonellini, M., & Mollema, P. (2000). A natural analog for a fractured and faulted reservoir in dolomite: Triassic sella group, northern italy. *AAPG Bulletin*, *84*, 314–344.

Bendat, J. S., & Piersol, A. G. (1971). *Random data: Analysis and measurement procedures*. Wiley.

Binley, A. (2015). Tools and techniques: Dc electrical methods. In G. Schubert (Ed.), *Treatise on geophysics* (2nd, pp. 233–259, Vol. 11). Elsevier. https://doi.org/10.1016/B978-0-444-53802-4.00192-8

Blanchy, G., Saneiyan, S., Boyd, J., & McLachlan, P. (2020). Resipy, an intuitive open source software for complex geoelectrical inversion/modeling. *Computers & Geosciences*, *143*, 104423. https://doi.org/10.1016/j.cageo.2020.104423

Bonometti, F. N. (2025). *Dolomites - digital-twin of landslides over mountains under climate changes to empower sustainability* [Tesi di dottorato]. Università degli Studi di Milano-Bicocca. https://hdl.handle.net/10281/547781

Colombero, C., Comina, C., Vinciguerra, S., & Benson, P. M. (2018). Microseismicity of an unstable rock mass: From field monitoring to laboratory testing [First published: 06 February 2018]. *Journal of Geophysical Research: Solid Earth*, *123*(2), 1673–1693. https://doi.org/10.1002/2017JB014612

Colombero, C., Jongmans, D., Fiolleau, S., Valentin, J., Baillet, L., & Bièvre, G. (2021). Seismic noise parameters as indicators of reversible modifications in slope stability: A review. *Surveys in Geophysics*, *42*, 339–375. https://doi.org/10.1007/s10712-021-09632-w

Cordex regional climate model data on single levels. (2019). https://doi.org/10.24381/cds.bc91edc3

De Pascale, S. (2023). Cambiamento climatico e frane, sul sas da lech "un'installazione" per studiare i movimenti causati dallo scioglimento del permafrost. *il Dolomiti*. https://www.ildolomiti.it/montagna/2023/cambiamento-climatico-e-frane-sul-sas-da-lech-uninstallazione-per-studiare-i-movimenti-causati-dallo-scioglimento-del-permafrost

EMSC-CSEM. (n.d.). Earthquake information [Accessed 2025]. https://www.emsc-csem.org/Earthquake_information

Global Terrestrial Network for Permafrost. (2025). Permafrost zones [Accessed: 2025-10-17]. https://gtnp.arcticportal.org/help/20-data/ontology/23-permafrost

Gobiet, A., Kotlarski, S., Beniston, M., Heinrich, G., Rajczak, J., & Stoffel, M. (2014). 21st century climate change in the european alps—a review. *Science of The Total Environment*, *493*, 1138–1151. https://doi.org/10.1016/j.scitotenv.2013.07.050

Google. (2025). Google Earth Pro [Fonte: Google Earth Pro, © Google 2025. Dati da SIO, NOAA, U.S. Navy, NGA, GEBCO. Immagini © 2015–2025 Airbus, Landsat / Copernicus.].

Istituto Superiore per la Protezione e la Ricerca Ambientale (ISPRA). (2022). Geosciences ir: Research infrastructure for the italian network of geological services [Start date: 1 October 2022; duration: 30 months; 16 partners (13 Universities + 3 Research Institutions)].

Jacquemart, M., Weber, S., Chiarle, M., Chmiel, M., Cicoira, A., Corona, C., Eckert, N., Gaume, J., Giacona, F., Hirschberg, J., Kaitna, R., Magnin, F., Mayer, S., Moos, C., van Herwijnen, A., & Stoffel, M. (2024). Detecting the impact of climate change on alpine mass movements in observational records from the european alps. *Earth-Science Reviews*, *258*, 104886. https://doi.org/10.1016/j.earscirev.2024.104886

Keim, L., & Brandner, R. (2001). Facies interfingering and synsedimentary tectonics on late ladinian–early carnian carbonate platforms (dolomites, italy). *International Journal of Earth Sciences*, *90*, 813–830. https://doi.org/10.1007/s005310000192

Kellerer-Pirklbauer, A., Lieb, G. K., Schoeneich, P., Deline, P., & Pogliotti, P. (Eds.). (2011). *Thermal and geomorphic permafrost response to present and future climate change in the european alps* [Final report of Action 5.3. Online publication. ISBN 978-2-903095-58-1, 177 pp.]. PermaNET Project.

Kirchner, M., Faus-Kessler, T., Jakobi, G., Leuchner, M., Ries, L., Scheel, H.-E., & Suppan, P. (2013). Altitudinal temperature lapse rates in an alpine valley: Trends and the influence of season and weather patterns [Published online 19 March 2012]. *International Journal of Climatology*, *33*, 539–555. https://doi.org/10.1002/joc.3444

Konno, K., & Ohmachi, T. (1998). Ground-motion characteristics estimated from spectral ratio between horizontal and vertical components of microtremor. *Bulletin of the Seismological Society of America*, *88*, 228–241.

Krainer, K., Mussner, L., Behm, M., & Hausmann, H. (2012). Multi-disciplinary investigation of an active rock glacier in the sella group (dolomites; northern italy). *Austrian Journal of Earth Sciences*, *105*, 48–62.

Ltd., G. S. (2019). *Dm16-r8 / dm16-r16 digitizer: Man-d16-0001 – chapter 4: Sta/lta triggering* [Available online: https://www.guralp.com/documents/html/MAN-D16-0001/s4.html (accessed DATE)]. Güralp Systems Ltd. UK.

McNamara, D. E., & Buland, R. P. (2004). Ambient noise levels in the continental united states. *Bulletin of the Seismological Society of America*, *94*(4), 1517–1527. https://doi.org/10.1785/012003001

Mussner, L. (2009, November). *Die geologie der sella-nordseite (dolomiten – südtirol) unter besonderer berücksichtigung der blockgletscher* [Diplomarbeit]. Leopold-Franzens-Universität Innsbruck, Institut für Geologie & Paläontologie [Betreuer: Ao. Univ. Prof. Dr. Karl Krainer].

Nakamura, Y. (1989). A method for dynamic characteristics estimation of subsurface using microtremor on the ground surface. *Quarterly Report of RTRI*, *30*(1), 25–33. https://doi.org/10.2219/rtriqr.30.25

Nakamura, Y. (1996). Clear identification of fundamental idea of nakamura's technique and its applications. *Proceedings of the 2nd International Symposium on the Effects of Surface Geology on Seismic Motion*, *2*, 3–10.

Nakamura, Y. (2000). On the h/v spectral ratio for microtremor and its application to the estimation of site effects. *Proceedings of the 12th World Conference on Earthquake Engineering*, *2*, 1–6.

NASA. (2025). What is permafrost?

National Geographic. (2023). Permafrost [Last updated October 19, 2023].

Nigrelli, G., & Chiarle, M. (2023). 1991–2020 climate normal in the european alps: Focus on high-elevation environments. *Journal of Mountain Science*, *20*, 2149–2163. https://doi.org/10.1007/s11629-023-7951-7

Nogoshi, M., & Igarashi, T. (1971). On the amplitude characteristics of microtremor (part 2). *Journal of the Seismological Society of Japan. 2nd Series*, *24*(1), 26–40. https://doi.org/10.4294/zisin1948.24.1_26

Pace, F., Vergnano, A., Godio, A., Romano, G., Capozzoli, L., Baneschi, I., Doveri, M., & Santilano, A. (2024). A new repository of electrical resistivity tomography and ground-penetrating radar data from summer 2022 near ny-ålesund, svalbard. *Earth System Science Data*, *16*, 3171–3192. https://doi.org/10.5194/essd-16-3171-2024

Peterson, J. (1993). *Observations and modeling of seismic background noise* (tech. rep. No. Open-File Report 93-322). U.S. Geological Survey. Albuquerque, New Mexico.

Politecnico di Torino. (2025). *Progetti prin 2022 e prin 2022 pnrr* (Technical Report). Politecnico di Torino. https://www.polito.it/sites/default/files/2025-09/Politecnico%20di%20Torino_PRIN%202022%20e%202022%20PNRR.pdf

Provincia Autonoma di Bolzano. (2018). Report pericoli naturali 2018.

Provincia autonoma di Bolzano — Meteo Alto Adige. (2025). Stazione meteo badia cima pisciadù [Accessed: 2025-10-17]. https://meteo.provincia.bz.it/stazioni-meteo-montagna.asp?stat_stid=121

Provincia Autonoma di Trento. (2025). Meteotrentino: Dati storici delle stazioni meteorologiche [Accessed: 2025-10-16]. https://storico.meteotrentino.it/

QGIS Development Team. (2023). QGIS Desktop version 3.34.4 [Software GIS open source. Disponibile da https://www.qgis.org/].

Stefani, M., Brack, P., Gianolla, P., Keim, L., Mastandrea, A., Maurer, F., Neri, C., Preto, N., Ragazzi, E., Riva, A., Roghi, G., & Russo, F. (2004). Triassic carbonate platforms of the dolomites: Carbonate production, relative sea-level fluctuations and the shaping of the depositional architecture. In *Volume on triassic carbonate systems* (pp. 44–64).

The MathWorks Inc. (2023). *Matlab version 9.15 (R2023b)*. The MathWorks Inc. Natick, Massachusetts.

Thomson, A. M., Calvin, K. V., Smith, S. J., Kyle, G. P., Volke, A., Patel, P., Delgado-Arias, S., Bond-Lamberty, B., Wise, M. A., Clarke, L. E., & Edmonds, J. A. (2011). RCP4.5: A pathway for stabilization of radiative forcing by 2100. *Climatic Change*, *109*, 77–94. https://doi.org/10.1007/s10584-011-0151-4

University of Zurich, University of Waterloo. (2025). Cryodata: Publicly available data.